Non-homogeneous thermal boundary conditions in low to medium Prandtl number turbulent pipe flows

Zur Erlangung des akademischen Grades eines

DOKTORS DER INGENIEURWISSENSCHAFTEN (Dr.-Ing.)

von der KIT-Fakultät für Maschinenbau des
Karlsruher Instituts für Technologie (KIT)

angenommene

DISSERTATION

von

M. Sc. Steffen Straub

Tag der mündlichen Prüfung: 27.04.2020

Hauptreferentin: Prof. Dr.-Ing. Bettina Frohnapfel
Korreferenten: Prof. Dr.-Ing. Manuel García-Villalba
Prof. Dr.-Ing. Luca Marocco

Abstract

The application of liquid metals as the heat transfer fluid in central receiver systems can increase their efficiency and make them economically more competitive. Therefore, a better understanding of the underlying heat transfer mechanism under non-homogeneous thermal boundary conditions is necessary for a safe and optimum design of the power plant. To this end, high-fidelity direct numerical simulations and large-eddy simulations are performed in this study to analyze the heat transfer in the receiver geometry.

As a first step, three different types of homogeneous thermal boundary conditions are compared and assessed to find the most appropriate one for the current application as well as highlighting their influences on thermal statistics in general. These are isothermal, isoflux and a mixed-type boundary condition. The simulations span a range of Reynolds numbers from $Re_b = 5300$ to $Re_b = 37700$ and two Prandtl numbers, $Pr = 0.71$ corresponding to air and $Pr = 0.025$ representing a class of liquid metals such as lead-bismuth eutectic. For low-Prandtl-number fluids the Nusselt number is $\approx 20\%$ lower when imposing isothermal boundary conditions compared to the other two. Decomposing the Nusselt number into laminar and turbulent contributions reveals the dominant turbulent terms as the radial turbulent heat flux contribution for $Pr = 0.71$ and the contribution due to the turbulent velocity field for $Pr = 0.025$. First- and second-order thermal statistics exhibit dependencies on the type of thermal boundary condition, not only limited to the near-wall region but also extending towards the core of the flow. As a result of this comparison, the isoflux boundary condition is selected for modeling non-homogeneous thermal boundary conditions on the receiver because the solar radiation imposes a wall heat flux distribution and the isoflux boundary condition is able to capture fluctuations of the wall temperature.

An azimuthally non-homogeneous wall heat flux distribution is prescribed to analyze how the inhomogeneity affects the thermal statistics. One half of the receiver is adiabatic and either a constant or sinusoidal distribution is set on

the other half. While azimuthally averaged Nusselt numbers are not affected, agreeing with the results of the homogeneous setup, the local Nusselt numbers are significantly different and need to be taken into account when designing the receiver because of the inhomogeneous wall temperature. Furthermore, the anisotropy of the turbulent thermal diffusivity as well as the turbulent Prandtl number is assessed. For high enough Reynolds numbers, the turbulent Prandtl number attains a value of approximately unity and becomes isotropic in the core of the flow, while close to the wall it remains anisotropic. A proper orthogonal decomposition unveils higher energy portions in the first modes for $Pr = 0.025$ compared to $Pr = 0.71$ due to the larger thermal structures at low Prandtl numbers, thereby aggregating the energy in fewer modes.

The complex azimuthally and axially non-homogeneous distribution of wall heat flux portray additionally the dependency of thermal statistics in streamwise direction. Nusselt numbers averaged in circumferential direction and evaluated at the location of maximum wall heat flux yield similar results for $Pr = 0.71$ whereas for low Prandtl numbers the Nusselt number evaluated at the location of maximum wall heat flux is smaller than the circumferentially averaged one. This is due to the less intense peak of the wall temperature caused by the high thermal diffusivity of low-Prandtl-number fluids. First- and second-order statistics for selected axial and azimuthal locations show similar features as in the setup of azimuthally non-homogeneous thermal boundary conditions superimposed with an axial development.

All of the generated results form a database for testing and tuning computationally less intensive Reynolds-averaged Navier–Stokes models and are available in the open access repository KITopen [SSD1–SSD3].

Zusammenfassung

Die Anwendung von Flüssigmetallen als Wärmetragermedium im Bereich der konzentrierenden Solarthermie kann deren Effizienz steigern und diese ökonomisch wettbewerbsfähiger machen. Deshalb ist ein besseres Verständnis der zugrunde liegenden Wärmeübergangsmechanismen unter nicht-homogenen thermischen Randbedingungen notwendig für ein sicheres und optimales Design des Kraftwerks. Zu diesem Zweck werden hochauflösende direkte numerische Simulationen und Grobstruktursimulationen in dieser Studie durchgeführt um den Wärmeübergang innerhalb der Receivergeometrie zu analysieren.

Als ein erster Schritt werden drei verschieden Typen von thermischen Randbedingungen verglichen und bewertet um diejenige zu finden, welche für die vorliegende Anwendung am besten geeignet ist und deren Einfluss auf thermische Statistiken im Allgemeinen herauszustellen. Diese sind isotherm, isoflux (konstanter Wandwärmestrom) und eine Mischungstyp Randbedingung. Die Simulationen umfassen einen Reynolds Zahl Bereich von $Re_b = 5300$ zu $Re_b = 37700$ und zwei Prandtl Zahlen, $Pr = 0.71$, korrespondierend zu Luft und $Pr = 0.025$, welche eine Klasse von Flüssigmetallen wie Blei-Bismuth Eutektikum repräsentiert. Für Fluide kleiner Prandtl Zahlen ist die Nusselt Zahl $\approx 20\%$ kleiner falls isotherme Randbedingungen aufgeprägt werden verglichen mit den anderen beiden. Das Aufspalten der Nusselt Zahl in laminare und turbulente Anteile enthüllt die dominanten turbulenten Terme als den radialen turbulenten Wärmestrom für $Pr = 0.71$ und den Beitrag aufgrund des turbulenten Geschwindigkeitsfelds für $Pr = 0.025$. Thermische Statistiken erster und zweiter Ordnung zeigen Abhängigkeiten vom Typ der thermischen Randbedingung, nicht nur begrenzt auf den Bereich nahe der Wand, sondern sich erstreckend in Richtung der Mitte der Strömung. Als ein Ergebnis dieses Vergleichs wird die isoflux Randbedingung ausgewählt zur Modellierung der nicht-homogenen thermischen Randbedingungen auf dem Receiver, weil die

Sonneneinstrahlung eine Verteilung des Wandwärmestroms vorschreibt und die isoflux Randbedingung Fluktuationen der Wandtemperatur abbilden kann.

Eine in Umfangsrichtung nicht-homogene Verteilung des Wandwärmestroms wird vorgeschrieben um zu analysieren wie die Inhomogenität die thermischen Statistiken beeinflusst. Eine Hälfte des Receivers ist adiabat und entweder eine konstante oder eine sinusoidale Verteilung wird auf der anderen Hälfte festgelegt. Während die in Umfangsrichtung gemittelten Nusselt Zahlen unbeeinflusst sind und mit den Ergebnissen aus dem homogenen Aufbau übereinstimmen, sind die lokalen Nusselt Zahlen signifikant verändert und müssen aufgrund der inhomogenen Wandtemperatur für die Auslegung des Receivers beachtet werden. Des Weiteren wird die Anisotropie der turbulenten thermischen Diffusivität und der turbulenten Prandtl Zahl bewertet. Für Reynolds Zahlen, welche groß genug sind, erreicht die turbulente Prandtl Zahl einen Wert von ungefähr Eins und wird in der Mitte der Strömung isotrop, während sie in der Nähe der Wand anisotrop bleibt. Eine Singulärwertzerlegung enthüllt höhere Anteile der Energie in den ersten Moden für $Pr = 0.025$ verglichen mit $Pr = 0.71$ aufgrund der größeren thermischen Strukturen bei kleinen Prandtl Zahlen, sodass sich die Energie in weniger Moden ansammelt.

Die komplexe nicht-homogene Verteilung in Umfangsrichtung und axialer Richtung zeigt zusätzlich die Abhängigkeit der thermischen Statistiken in Strömungsrichtung. Nusselt Zahlen, welche in Umfangsrichtung gemittelt werden, und, welche an der Stelle des größten Wandwärmestroms ausgewertet werden, zeigen ähnliche Ergebnisse für $Pr = 0.71$, wohingegen die Nusselt Zahl ausgewertet an der Stelle des größten Wandwärmestroms für kleine Prandtl Zahlen kleiner ist als die in Umfangsrichtung gemittelte Nusselt Zahl. Dies liegt an dem weniger intensiven Maximum der Wandtemperatur aufgrund der hohen thermischen Diffusivität von Fluiden mit kleinen Prandtl Zahlen. Statistiken erster und zweiter Ordnung für ausgewählte Axial- und Umfangspositionen zeigen ähnliche Eigenschaften wie in dem Aufbau der in Umfangsrichtung nicht-homogenen thermischen Randbedingungen überlagert mit einer axialen Entwicklung.

Alle generierten Ergebnisse formen eine Datenbank für das Testen und Einstellen von weniger rechenintensiven Reynolds gemittelten Navier–Stokes Modellen und sind verfügbar in dem frei zugänglichen Repositorium KITopen [SSD1–SSD3].

Acknowledgements

I would like to use this opportunity to express my gratitude to the people without whose support this project would not have been the same. First of all, I want to thank Bettina Frohnapfel for the opportunity to study and work in her group and write this thesis under her guidance as well as Thomas Wetzel.

The initial ambition to pursue a PhD goes back to the positive experience I had when working on my master thesis at KTH together with Philipp Schlatter and Ricardo Vinuesa in Stockholm and Davide Gatti who introduced me to the world of numerical simulations at KIT. I believe it is important to feel appreciated and welcome in your working environment to be the best version of yourself. Thus, I want to thank all of my colleagues at the ISTM who created such a relaxed and inspiring atmosphere at the institute. I really enjoyed my time not only in the office but also during our countless trips, conferences and celebrations together. So thanks to Andrea, Andreas, Alex, Anna, Daniel, Davide, Erik, Franco, Frieder, Georg, Giacomo, Jochen, Karin, Kay, Lars, Marc, Pourya, Robin, Sibela, Tobias and Verena.

Thank you, Luca, for hosting me during my research semester at Politecnico di Milano.

Last but not least, I thank my parents Rosemarie and Albrecht for their support and my brother Alexander as well as my sisters Kerstin, Sabine and Katrin who are always there for me.

The simulations were performed on the national supercomputer Cray XC40 at the High Performance Computing Center Stuttgart (HLRS) under the grant number ctbctpf/44106. This work was performed with the help of the Large Scale Data Facility at the Karlsruhe Institute of Technology funded by the Ministry of Science, Research and the Arts Baden-Württemberg and by the Federal Ministry of Education and Research. Support from Karlsruhe House of Young Scientists (KHYS) in form of a research travel grant is appreciated.

Table of contents

Nomenclature

Latin Symbols

SYMBOL	DESCRIPTION
$\tilde{a}$	Exponential decay rate for isothermal (IT) boundary condition
A	Cross section of the pipe
$A(t)$	Time-dependent material surface
$A^*(t)$	Arbitrarily moving time-dependent control surface
A_{ij}	Stiffness matrix
$\boldsymbol{b}$	Local velocity of the control surface
B_{ij}	Mass matrix
Bo	Buoyancy parameter
c_v	Specific heat capacity at constant pressure
D	Pipe diameter
D_{ij}	Differentiation matrix
$\mathrm{d}A$	Differential area
$\mathrm{d}V$	Differential volume
e	Internal energy (per unit mass)
E	Power spectral density
$\mathbf{F}$	Forcing term to drive the flow
f	Volume force
Gr	Grashof number
$\mathcal{H}$	High-pass spectral filter for relaxation-term
h	Heat transfer coefficient
$\mathbf{I}$	Identity tensor

k_z	Streamwise wave number
L_z	Pipe length
L_h	Hydrodynamic entrance length
L_{th}	Thermal entrance length
$\boldsymbol{n}$	Outward unit normal vector
Nu	Nusselt number
$Nu_{HF,r}$	Nusselt number contribution due to the radial turbulent heat flux
$Nu_{HF,z}$	Nusselt number contribution due to the streamwise turbulent heat flux
Nu_L	Laminar Nusselt number contribution
Nu_{RSS}	Nusselt number contribution due to the turbulent velocity field
p	(Mean) pressure
Pe	Péclet number
Pr	Prandtl number
$\boldsymbol{q}$	Heat flux
Q	Continuity restriction matrix
R	Boundary condition restriction matrix
R	Pipe radius
r	Radial coordinate
$\boldsymbol{S}$	Strain rate tensor
S_Θ	Source term in non-dimensional temperature equation
t	Time
T	Temperature
T_b	Bulk temperature
$\boldsymbol{U}$	Unitary matrix containing the left singular vectors
$\mathbf{U}$	(Instananeous) velocity
U_b	Bulk velocity
$\boldsymbol{V}$	Unitary matrix containing the right singular vectors
$V(t)$	Time-dependent material volume

$V^*(t)$	Arbitrarily moving time-dependent control volume
w_k	Quadrature weights
$\boldsymbol{X}$	Data matrix
$\mathbf{x}$	Vector of spatial coordinates
z	Streamwise coordinate

Greek Symbols

SYMBOL	DESCRIPTION
α	Thermal diffusivity
β	Thermal expansion coefficient
χ	Model parameter for relaxation-term
δ_{ij}	Kronecker delta
λ	Eigenvalue
λ	Thermal conductivity
λ_z	Streamwise wavelength
μ	Dynamic visosity
μ_v	Coefficient of bulk velocity
∇	Nabla operator
ν	Kinematic viscosity
Φ	Fractional flow rate
Φ_T	Fractional flow rate of the turbulent velocity field
φ	Azimuthal coordinate
Φ	Quantity of interest (dummy variable)
ρ	Density
$\mathbf{\Sigma}$	Diagonal matrix containing the singular values
σ_i	Singular values
$\boldsymbol{\sigma}$	Deviatoric stress tensor
Θ	Non-dimensional temperature
ϑ	Fluctuating part of non-dimensional temperature
$\boldsymbol{\tau}$	Stress tensor

Superscipts

SYMBOL	DESCRIPTION
$*$	Complex conjugate
e	Element
$+$	Scaling in viscous units
t	Time (average)
T	Transpose

Subscripts

SYMBOL	DESCRIPTION
0	Inlet
a	Averaging (time)
r	Radial component
w	Wall (temperature, heat flux)
z	Streamwise component

Abbreviations

SYMBOL	DESCRIPTION
ADM	Approximate deconvolution model
AMG	Algebraic multigrid
BDF	Backward difference formula
CRS	Central receiver system
CSP	Concentrated solar power
DNS	Direct numerical simulation
EXT	Extrapolation
FEM	Finite element method
FIK	Fukagata–Iwamoto–Kasagi (identity)
GLL	Gauss–Lobatto–Legendre
HTF	Heat transfer fluid
IF	Isoflux

IT	Isothermal
LES	Large-eddy simulation
MBC	Mixed-type boundary condition
NSE	Navier–Stokes equation
PDE	Partial differential equation
POD	Proper orthogonal decomposition
PSD	Power spectral density
RANS	Reynolds-averaged Navier–Stokes (equations)
RSS	Reynolds shear stress
SEM	Spectral element method
TBC	Thermal boundary condition

1 Introduction

Within this chapter the motivation behind this thesis is explained and an overview of the previous works in the literature is given to put this project into perspective. Derived from the motivation and the literature review, the research questions are formulated and the procedure is outlined.

1.1 Motivation

Providing renewable and sustainable energy is one of the major challenges of the current generation [29]. One promising technique for harvesting solar power are concentrated solar power (CSP) plants, in particular central receiver systems (CRS). Such a CRS consists of many heliostats, which track the sun during the day and reflect the solar radiation onto a central receiver, potentially a thermal energy storage system as well as a heat exchanger to couple the CRS with a conventional or advanced power cycle. Fig. 1.1 on the left shows the solar power tower of the Plataforma Solar de Almería in Spain. The focus of this study is on the receiver, subject to a circumferentially and axially non-homogeneous thermal boundary condition (TBC) resulting from the reflected and focused solar radiation. A simple schematic depicting the receiver geometry as a straight pipe and a non-homogeneous TBC is given in Fig. 1.1 on the right.

In order to make the CRS economically more competitive, the heat transfer in the receiver, which is an essential part of the power plant and its proper design is crucial, is to be optimized. Therefore, liquid metals are proposed as an advanced heat transfer fluid (HTF) due to their advantageous thermo-physical properties to increase the efficiency of CRSs [58].

Liquid metals differ from conventional HTFs such as Nitrate salt, air, water/steam [59] by their large thermal conductivity, resulting in a low molecular

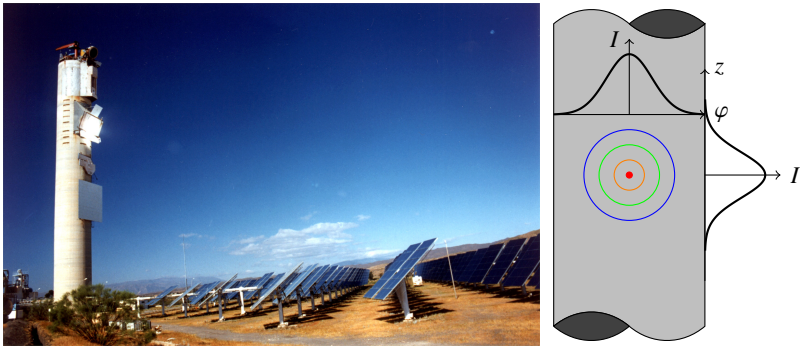

Figure 1.1: Solar power tower in Almería, Spain (left, source: DLR CC-BY 3.0) and a sketch of a receiver under a circumferentially and axially non-homogeneous thermal boundary condition (right).

Prandtl number. Thus, the heat transfer mechanism of liquid metals is substantially different from conventional HTFs [27]. As consistent and accurate measurements in liquid metal experiments are challenging to perform, numerical simulations can provide further insights into the underlying heat transfer mechanism. Such numerical simulations provide accurate predictions of the inner wall temperature, which are required for designing the receiver appropriately to withstand the thermal loading, e.g. by a structural simulation of the solid.

1.2 Literature review

Early studies on the effect of non-homogeneous thermal boundary conditions have been mostly analytical or experimental. In 1963 Reynolds [67] investigated analytically the influence of a circumferentially varying heat flux on the heat transfer in a pipe for fully developed laminar and turbulent flow. Diffusivities in radial and circumferential directions were modeled and assumed to be identical in this approach. The wall temperature was shown to be considerably different than by employing a Nusselt number for homogeneous wall heat flux. In a similar analytical approach, Sparrow and Lin [74] also assumed the radial

and tangential diffusivities for heat to be identical and additionally equal to the momentum diffusivities.

Experiments on non-homogeneous thermal boundary conditions were performed by Black and Sparrow [9] for air. A tube of variable thickness in circumferential direction was heated electrically. They found that the variation of the locally evaluated heat transfer coefficient was smaller than the variation of the imposed heat flux and that the predictions of the aforementioned analytical approaches overestimated the variation of the heat transfer coefficient.

Rapier [65] proposed a simple model to predict the wall temperature for circumferentially varying heat flux based on separating the flow into two regions: the boundary layer with the molecular conductivity and the turbulent core with an effective mean conductivity. Results were found to be in good agreement with Ref. [9, 67].

The era of studying wall-bounded turbulence and turbulent heat transfer by means of direct numerical simulations (DNS) started in the 1980s with the pioneering work of Kim, Moin, and Moser [40] as well as the study for passive scalars by Kim and Moin [41]. In the early '90s, Kasagi, Tomita, and Kuroda [36] introduced a particularly simple numerical type of thermal boundary condition where the wall temperature is assumed to be constant in time and it increases linearly in streamwise direction, similar to a constant wall heat heat flux boundary condition. This type of boundary condition will be denoted as mixed-type boundary condition in the following chapters. Kawamura et al. [39] performed direct numerical simulations on a range of Prandtl numbers from $Pr = \nu/\alpha = 0.025$ to $Pr = 5$ employing the mixed-type boundary condition. They reported the near-wall behavior of turbulent quantities, thermal statistics and budgets of the temperature variance and turbulent heat flux. In a following paper [38], they extended their database from the previous friction Reynolds number of $Re_\tau = 180$ to $Re_\tau = 395$ and showed near-wall values of turbulent Prandtl numbers to be independent of Reynolds and molecular Prandtl number for $Pr < 0.2$. For low-Prandtl-number fluids the turbulent Prandtl number is found to be higher than for $Pr \approx 1$ as the turbulent thermal diffusivity is lower. However, the dependency on the Reynolds number indicates that these high values are a result of the low Reynolds number as convection becomes more dominant than conduction with increasing Reynolds number. A further increase in Reynolds number up to $Re_\tau = 1020$ in a turbulent channel flow by Abe, Kawamura, and Matsuo [1] revealed a considerable

Reynolds number dependency of the temperature fluctuations (scaled in inner units), especially for the Prandtl number of $Pr = 0.025$ due to the increase of convective heat transfer with higher Reynolds number. For $Pr = 0.71$ the temperature fluctuations presented the same weak dependence on the Reynolds number as the fluctuations of the streamwise velocity.

The effect of different types of thermal boundary conditions for a constant wall temperature (isothermal: IT) and a constant wall heat flux (isoflux: IF) in a thermal boundary layer were studied by Kong, Choi, and Lee [42]. The effect of the type of thermal boundary condition on thermal statistics has been further explored by Tiselj et al. [76]. They employed DNSs to compare isoflux and mixed-type boundary conditions in a channel flow with a conjugate heat transfer calculation, where also the heat transfer in the solid was considered. In another paper of the same group [78], they referred to a non-fluctuating wall temperature boundary condition, i.e. the mixed-type boundary condition, and a fluctuating wall temperature boundary condition, i.e. the isoflux boundary condition, highlighting their different behavior of the temperature fluctuations at the wall. These two types are the limiting cases of the conjugate heat transfer problem. They found only a weak influence of up to 1 % depending on the type of thermal boundary condition on the Nusselt number. Piller [62] compared three different types of thermal boundary conditions in a turbulent pipe flow, namely the isoflux, isothermal and mixed-type boundary conditions. He concluded that the thermal boundary condition can cause differences in the thermal statistics not only in the near-wall region but also in the core region due to a different axial heat flux of the isothermal boundary condition. However, his comparison was limited to a low Reynolds number of $Re_b = U_b D/\nu = 5300$ and only one Prandtl number of $Pr = 0.71$. Therefore, a wider range of parameters, i.e. higher Reynolds numbers and different Prandtl numbers, needs to be taken into account for a more general statement on the influences of the type of thermal boundary condition. Another study by Flageul et al. [19], comparing the mixed-type boundary condition with the isoflux and a Robin boundary condition, i.e. a linear combination of isothermal and isoflux, as well as conjugate heat transfer, highlighted the importance of accurate predictions of the wall temperature, being dependent on the type of thermal boundary condition. Higher Reynolds numbers have been considered only more recently, due to the improving computational resources, for instance by Pirozzoli, Bernardini, and Orlandi [63] at a friction Reynolds number of $Re_\tau = 4088$ and $Pr = \{0.2, 0.71, 1.0\}$ in a channel flow. Comparing a thermal

boundary condition imposed by different temperatures of the upper and the lower wall with a boundary condition where a constant source term is added in the temperature equation, they observed an influence of the type of the thermal boundary condition mostly limited to the core region of the flow. Even lower Prandtl numbers, corresponding to liquid metals, were studied by Alcántara-Ávila, Hoyas, and Pérez-Quiles [2] of $Pr = 0.007$ to $Pr = 0.71$ for turbulent channel flow. They compared their results employing the mixed-type boundary condition to the constant source term condition of Pirozzoli, Bernardini, and Orlandi [63] and found only small deviations in the thermal statistics. In another study on thermal boundary layers by Li et al. [45], they compared isothermal and isoflux boundary conditions at Prandtl numbers of $Pr = \{0.2, 0.71, 2\}$ and $Re_\Theta = 830$, based on the momentum thickness and free-stream velocity. They found no effects on the mean temperature but on the temperature variance and observed deviations between the thermal boundary conditions in the one-dimensional premultiplied energy spectra.

Progress in the field of non-homogeneous thermal boundary conditions was not only limited to numerical works. Barletta, Lazzari, and Zanchini [7] extended earlier analytical works by considering laminar mixed convection under non-homogeneous thermal boundary conditions in circumferential direction. They showed that depending on the parameters, the local Nusselt number can become singular. In a following paper [6], they pointed out that the average Nusselt number resulting from a non-homogeneous wall heat flux, i.e. one half of the pipe is heated while the other one is adiabatic, is the same as the Nusselt number under homogeneous wall heat flux for forced convection.

Recently, liquid metals, i.e. low-Prandtl-number fluids, have been proposed as the heat transfer fluid in CRSs [58, 59]. For an efficient design of such power plants employing liquid metals, accurate engineering correlations are required. Pacio, Marocco, and Wetzel [57] reviewed existing data and correlations for the heat transfer in liquid metals covering the isothermal and isoflux boundary condition. Circumferentially and axially non-homogeneous thermal boundary conditions, as occurring in the receiver of a central receiver system, were studied numerically by Marocco et al. [50]. They considered liquid metals as the operating fluid and employed a four-equation turbulence model simulating the conjugate heat transfer problem in the context of Reynolds-averaged Navier–Stokes (RANS) equations. The averaged Nusselt number agreed with the one evaluated for uniform thermal boundary conditions while correlations devel-

oped for uniform thermal boundary conditions were not applicable for the local Nusselt numbers and wall temperatures. Circumferentially non-homogeneous thermal boundary conditions in a turbulent pipe flow were studied by means of direct numerical simulations by Antoranz et al. [4] for friction Reynolds numbers of $Re_\tau = 180, 360$ and Prandtl numbers of $Pr = 0.7, 4$. They used a proper orthogonal decomposition on their dataset to study coherent structures [5]. Further numerical studies employed RANS modeling to study non-homogeneous thermal boundary conditions in the context of concentrated solar power systems [22, 56]. Okafor, Dirker, and Meyer [56] took into account heat conduction within the solid as well as convective and irradiative losses and found that the average internal heat transfer coefficient remained largely unaffected by the non-homogeneous heat flux distribution. Fritsch et al. [22] additionally included transient effects due to a sudden change in the prescribed wall heat flux and proposed a simplified model based on the finite element method. The simplified model required the spatial distribution of the Nusselt number to be known as significant discrepancies between the simplified model and a more detailed RANS simulation where found, when assuming a constant Nusselt number.

Even though there are analytical, experimental and numerical studies dealing with non-homogeneous thermal boundary conditions, there is still a lack of high-fidelity data, particularly when it comes to low-Prandtl-number fluids such as liquid metals. Such data are essential for a deeper understanding of the underlying physical mechanisms, governing such complex heat transfer problems.

1.3 Objectives and procedure

The objective of the present thesis is to fill the aforementioned gap of high-fidelity data by generating a database with numerical simulations on the heat transfer of low-Prandtl-number fluids in turbulent pipe flow. Medium-Prandtl-number fluids of $Pr = 0.71$ are included additionally in this project to allow for a direct comparison between the heat transfer of low- and medium-Prandtl-number fluids. These data are used to answer the following research questions of engineering as well as of fundamental nature.

1. *What is the appropriate type of thermal boundary condition for a central receiver system with liquid metals as heat transfer fluid?*
   In a first step, homogeneous TBCs are studied in detail to asses their influence on the heat transfer in general and in order to select the TBC which is the most suited one to represent the actual boundary condition of a CRS.

2. *How does the non-homogeneity of the thermal boundary condition affect the heat transfer?*
   High-fidelity databases of non-homogeneous TBCs are generated and evaluated by comparing the data to the homogeneous TBC cases.

3. *What are the physical mechanisms underlying the heat transfer of liquid metals under non-homogeneous thermal boundary conditions?*
   A more thorough physical understanding is sought by scrutinizing the high-fidelity databases and interpreting the results.

These questions will be tackled by numerically modeling the receiver of a CRS as a straight pipe, which is irradiated non-homogeneously and depicted in Fig. 1.1 on the right. The convective heat transfer is mathematically represented by a set of partial differential equations (PDEs), namely the Navier–Stokes equation (NSE), the continuity equation and an advection-diffusion equation for the temperature, together with appropriate boundary conditions. The flow is considered to be incompressible and Newtonian, thermophysical properties are considered to be constant and temperature is treated as a passive scalar with negligible heating due to viscous dissipation. This set of PDEs is solved numerically by means of direct numerical and large-eddy simulations of increasing complexity, starting with the homogeneously distributed TBC over the azimuthally non-homogeneous TBC to a locally concentrated TBC. The spectral element method (SEM) implemented in the massively parallelized high-order open source solver Nek5000 [54] is employed for solving the set of PDEs. As a result of the numerical simulations global and local thermal statistics are evaluated, i.e. the (local) Nusselt number, mean temperature, temperature variance and turbulent heat fluxes as well as budgets of the temperature variance and turbulent heat fluxes. These results are collected in databases and made publicly available in the open-access repository KITopen.

1.4 Structure of the thesis

The necessary fundamentals for the numerical studies are given in Chapter 2, containing a description of the mathematical model and a general overview of the employed numerical methods together with a brief description of a certain reduced order modeling technique, the proper orthogonal decomposition. For answering the first research question regarding the appropriate type of thermal boundary condition, a detailed investigation is presented in Chapter 3. Circumferentially non-homogeneous thermal boundary conditions are introduced in Chapter 4 and their effects on thermal statistics is presented and discussed. Chapter 5 deals with the influence of a complex distribution of axially and azimuthally non-homogeneous thermal boundary condition on thermal statistics. The thesis closes with the gathered conclusions of Chapters 3 - 5 and a brief outlook on what could be studied in the future.

2 Fundamentals

The theoretical basis of the numerical simulations is explained in this chapter, starting with the underlying mathematical model and its assumptions and followed by a general description of its numerical treatment. The last section gives a brief introduction to the proper orthogonal decomposition.

2.1 Mathematical model

The physical processes which are to be described by the mathematical model are the fluid flow through the receiver and the heat transfer within the receiver. In the field of continuum mechanics, these processes can be described by the conservation of mass, momentum and energy. These conservation principles form a particular set of partial differential equations, namely the continuity equation, the Navier–Stokes equation and an advection-diffusion equation for the temperature, where certain assumptions are introduced in the following when needed. This brief derivation closely follows Kundu, Cohen, and Dowling [44].

A useful and purely kinematic relation is the *Reynolds transport theorem* [44]

$$\frac{\mathrm{d}}{\mathrm{d}t}\int_{V^*(t)} \Phi \mathrm{d}V = \int_{V^*(t)} \frac{\partial \Phi}{\partial t}\mathrm{d}V + \int_{A^*(t)} \Phi \boldsymbol{b}\cdot\boldsymbol{n}\mathrm{d}A \tag{2.1}$$

which relates the total time derivative of the volume integral of the quantity of interest Φ over an arbitrarily moving time-dependent control volume $V^*(t)$ to the local change in time of Φ and the flux through the arbitrarily moving time-dependent control surface $A^*(t)$. The local velocity of the control surface is denoted by $\boldsymbol{b}$ and $\boldsymbol{n}$ is the outward normal unit vector.

The conservation of mass given in integral form for a time-dependent material volume $V(t)$ is [44]

$$\frac{\mathrm{d}}{\mathrm{d}t}\int_{V(t)}\rho \mathrm{d}V = \int_{V(t)}\frac{\partial \rho}{\partial t}\mathrm{d}V + \int_{A(t)}\rho \mathbf{U}\cdot\boldsymbol{n}\mathrm{d}A = 0 \tag{2.2}$$

where the Reynolds transport theorem, Eq. (2.1), has been applied on the density ρ for a material volume where the local velocity of the material surface $A(t)$ is identical with the local velocity $\mathbf{U}$. Using Gauss' divergence theorem to recast the surface integral to a volume integral and requiring the equation to hold for any choice of material volume yields the differential form of the mass conservation equation [44] also known as the *continuity equation*:

$$\frac{\partial \rho}{\partial t} + \nabla\cdot(\rho\mathbf{U}) = 0 \tag{2.3}$$

In order to simplify the mass conservation equation, incompressibility is assumed. A flow is considered to be incompressible if the material derivative of the density vanishes [44], i.e.

$$\frac{\mathrm{D}\rho}{\mathrm{D}t} \equiv \frac{\partial \rho}{\partial t} + \mathbf{U}\cdot\nabla\rho = 0 \tag{2.4}$$

so that the *continuity equation for incompressible flows* reduces to [44]

$$\nabla\cdot\mathbf{U} = 0 \tag{2.5}$$

In other words, the velocity field needs to be solenoidal. According to the detailed handbook by Fazio et al. [18], liquid metals are in good approximation incompressible below their boiling point.

The conservation of momentum in integral form relates the change of momentum in a control volume with surface forces, i.e. stresses, $\boldsymbol{\tau}$ and volume forces f acting on the control surface and volume, respectively [44]

$$\frac{\mathrm{d}}{\mathrm{d}t}\int_{V(t)}\rho\mathbf{U}\mathrm{d}V = \int_{A(t)}\boldsymbol{n}\cdot\boldsymbol{\tau}\mathrm{d}A + \int_{V(t)}\rho\boldsymbol{f}\mathrm{d}V \tag{2.6}$$

The differential form of the momentum conservation equation can be derived from Eq. (2.6) by using the Reynolds transport theorem to rewrite the left-hand side, Gauss' divergence theorem to recast the surface integrals to volume

integrals, requiring the equation to hold for any choice of material volume and recognizing the differential mass conservation equation, Eq. (2.3), to simplify the left-hand side, resulting in *Cauchy's equation of motion* [44]:

$$\rho \frac{\mathrm{D}\mathbf{U}}{\mathrm{D}t} = \rho \left(\frac{\partial \mathbf{U}}{\partial t} + (\mathbf{U} \cdot \nabla)\, \mathbf{U} \right) = \nabla \cdot \boldsymbol{\tau} + \rho \boldsymbol{f} \tag{2.7}$$

A constitutive equation for the Cauchy stress tensor $\boldsymbol{\tau}$, a symmetric second order tensor, is necessary to form a closed set of equations. The stress tensor can be decomposed into fluid-static p and fluid-dynamic $\boldsymbol{\sigma}$ contributions [44], so that

$$\boldsymbol{\tau} = -p\mathbf{I} + \boldsymbol{\sigma} = -p\mathbf{I} + 2\mu \left(\boldsymbol{S} - \frac{1}{3}(\nabla \cdot \mathbf{U})\mathbf{I} \right) + \mu_v (\nabla \cdot \mathbf{U})\mathbf{I} \tag{2.8}$$

where the fluid-static contribution is identified as the (mean) pressure and a linear relationship between the fluid-dynamic contribution $\boldsymbol{\sigma}$, or deviatoric stress tensor, and the strain rate tensor $\boldsymbol{S}$, the symmetric part of the velocity gradient tensor, is assumed. The identity tensor is denoted by $\mathbf{I}$, the dynamic viscosity is μ and the coefficient of bulk velocity is μ_v [44]. Fluids which satisfy Eq. (2.8) are called *Newtonian fluids* [44] and liquid metals are in good approximation Newtonian fluids [18]. Due to the solenoidality of the velocity field for incompressible flows, Eq. (2.5), the constitutive equation for Newtonian fluids reduces to [44]

$$\boldsymbol{\tau} = -p\mathbf{I} + 2\mu \boldsymbol{S} \tag{2.9}$$

Substituting the constitutive equation, Eq. (2.9), for the stress tensor in Cauchy's equation of motion, Eq. (2.7), and using the continuity equation for incompressible flows, Eq. (2.5), results in the Navier–Stokes equation for incompressible flows:

$$\rho \frac{\mathrm{D}\mathbf{U}}{\mathrm{D}t} = \rho \left(\frac{\partial \mathbf{U}}{\partial t} + (\mathbf{U} \cdot \nabla)\, \mathbf{U} \right) = -\nabla p + \nabla \cdot (\mu \nabla \mathbf{U}) + \rho \boldsymbol{f} \tag{2.10}$$

The Navier–Stokes equation for incompressible flows and constant thermophysical properties is therefore given by [44]

$$\frac{\partial \mathbf{U}}{\partial t} + (\mathbf{U} \cdot \nabla)\,\mathbf{U} = -\frac{1}{\rho}\nabla p + \nu \nabla^2 \mathbf{U} + \boldsymbol{f} \tag{2.11}$$

where ∇^2 denotes the Laplace operator and $\nu = \mu/\rho$ is the kinematic viscosity.

The assumption of constant thermophysical properties is justified for small enough temperature variations and it is a common assumption to study turbulent convective heat transfer problems in basic research (e.g. [1, 4, 62, 66, 75]). An estimation of the temperature variations in the present simulations is given in App. A.1

The third conservation principle required to describe the convective heat transfer process within the receiver is the conservation of energy. The change of the total energy, as the sum of internal energy e and kinetic energy, of a material volume is related to work performed on the fluid by body forces and surface forces as well as due to heat transfer in/out of the control volume. In integral form the conservation of total energy states [44]

$$\frac{\mathrm{d}}{\mathrm{d}t}\int_{V(t)} \rho \left(e + \frac{1}{2}\mathbf{U}^2\right) \mathrm{d}V = \int_{V(t)} \rho \boldsymbol{f} \cdot \mathbf{U} \mathrm{d}V + \int_{A(t)} (\boldsymbol{\tau} \cdot \mathbf{U} - \boldsymbol{q}) \cdot \boldsymbol{n} \mathrm{d}A \tag{2.12}$$

where $\boldsymbol{q}$ is the heat flux. The differential form of the total energy conservation equation is derived by rewriting the left-hand side with the Reynolds transport theorem, using Gauss' divergence theorem to recast surface integrals to volume integrals, requiring the equation to hold for any choice of material volume and recognizing the differential mass conservation equation, Eq. (2.3), to simplify the left-hand side:

$$\rho \frac{\mathrm{D}}{\mathrm{D}t}\left(e + \frac{1}{2}\mathbf{U}^2\right) = \rho \boldsymbol{f} \cdot \mathbf{U} + \nabla \cdot (\boldsymbol{\tau} \cdot \mathbf{U}) - \nabla \cdot \boldsymbol{q} \tag{2.13}$$

A separate equation for the mechanical energy is deduced from Cauchy's equation of motion, Eq. (2.7), multiplied by $\mathbf{U}$ [44]:

$$\frac{\rho}{2}\frac{\mathrm{D}\mathbf{U}^2}{\mathrm{D}t} = (\nabla \cdot \boldsymbol{\tau}) \cdot \mathbf{U} + \rho \boldsymbol{f} \cdot \mathbf{U} \tag{2.14}$$

Subtracting the conservation equation for mechanical energy, Eq. (2.14), from the conservation equation for the total energy, Eq. (2.13), gives the conservation equation for internal energy

$$\rho \frac{\mathrm{D}e}{\mathrm{D}t} = -p\nabla \cdot \mathbf{U} + \boldsymbol{\sigma} : \boldsymbol{S} - \nabla \cdot \boldsymbol{q} \tag{2.15}$$

The heating due to viscous dissipation of energy $\boldsymbol{\sigma} : \boldsymbol{S} = 2\mu \boldsymbol{S} : \boldsymbol{S}$ (for incompressible flows) is typically much smaller than the convective terms in the energy equation and therefore its contribution is negligible [8, 32, 44]. Evaluating the numerically determined dissipation of turbulent kinetic energy a posteriori and comparing its influence to the advective heat flux, shown in App. A.1, confirms that the heating due to viscous dissipation is indeed negligible.

For incompressible flows, with $\mathrm{d}e = c_v \mathrm{d}T$ and $c_v = c_p$ [32], and ideal gases, the conservation equation for internal energy, Eq. (2.15), can be simplified to find the *conservation equation for temperature* such that [32, 44]

$$\frac{\mathrm{D}T}{\mathrm{D}t} = \alpha \nabla^2 T \tag{2.16}$$

where $\alpha = \lambda/(\rho c_p)$ denotes the thermal diffusivity, viscous dissipation is neglected, constant thermophysical properties are assumed and Fourier's law of heat conduction is introduced.

The set of partial differential equations (2.5), (2.11) and (2.16) constitute the mathematical model to describe the convective heat transfer within the receiver under the assumptions of an incompressible flow and Newtonian fluid, constant thermophysical properties and negligible heating due to viscous dissipation. Two additional assumptions are made to simplify the mathematical model. First, the flow is assumed to be hydrodynamically and thermally fully developed, except for axially non-homogeneous thermal boundary conditions. The hydrodynamic entrance length for a turbulent pipe flow is estimated to be $L_h = 25\,D$ for $Re_b = 37700$ [30]. A thermally fully developed flow is reached, when the Nusselt number is independent of the axial location [8]. The thermal entrance length for the current setup is estimated to be $L_{th} = 16\,D$ for $Re_b = 5300$ and $Pr = 0.025$ [T4] and up to $L_{th} = 35\,D$ [18] for higher Reynolds numbers. Second, the temperature is treated as a passive scalar, i.e. buoyancy forces are neglected and only forced convection is considered. For

high enough Reynolds numbers this is a good approximation, as estimated for $Re_b = 37700$ in App. A.1.

This set of partial differential equations is accompanied by appropriate boundary conditions and depending on the type of boundary condition and its treatment, additional source terms are possibly introduced. This is explained in the following chapters, when describing the setup of the homogeneous and non-homogeneous thermal boundary conditions.

2.2 Numerical methods: the spectral element method

The analytical partial differential equations governing the turbulent convective heat transfer, and derived in the previous section, need to be solved numerically as there are only few analytical solutions to the Navier–Stokes equation (2.11). The numerical approach adopted in the present project to solve the system of partial differential equations is the spectral element method. This method can be seen as a particular extension of "classical" single-domain spectral methods to multi-domain methods enabling the treatment of more complex geometries, coordinate singularities, discontinuous coefficients or solutions, and taking into account solution and efficiency considerations [43]. A detailed description of this method is given in Deville, Fischer, and Mund [15] and more generally on multi-domain methods in Canuto et al. [11]. A brief description, following Deville, Fischer, and Mund [15] and Couzy [14], is given in this section.

The spectral element method was first introduced by Patera [61], combining the flexibility of finite elements with the accuracy of spectral methods. The spatial discretization is based on a weak (Galerkin) formulation of the problem, which will be presented briefly in the following subsection on a model problem. Discretization in time is presented afterwards and some remarks on the scaling and parallelization of the employed code conclude this section.

2.2.1 Galerkin formulation

The model problem for the spatial discretization is the 1D Poisson equation

$$-\frac{\mathrm{d}^2 u(x)}{\mathrm{d}x^2} = f(x), \tag{2.17}$$

with homogeneous Dirichlet boundary conditions.

We use an approximate solution (trial solution) to the differential equation, constructed as a linear combination of basis coefficients $\hat{u}_j$ and basis functions $\phi_j(x)$

$$u_N(x) = \sum_{j=1}^{N} \hat{u}_j \phi_j(x) \tag{2.18}$$

where the basis functions span a finite-dimensional trial space X_0^N, which fulfills the homogeneous boundary conditions

$$X_0^N = \{\phi_1(x), \phi_2(x), ..., \phi_N(x)\}, \qquad \phi_j(0) = \phi_j(1) = 0 \tag{2.19}$$

The trial solution does not, in general, fulfill the model problem, so that a residual

$$r(x) = f(x) + \frac{\mathrm{d}^2 u_N(x)}{\mathrm{d}x^2} \tag{2.20}$$

remains. We do not require for the residual to vanish, but for it to be orthogonal to a set of functions from a test space X_0^N.

$$\int_0^1 v r \mathrm{d}x = 0, \qquad \forall v \in X_0^N \tag{2.21}$$

Note that in the Galerkin formulation test space and trial spaces are chosen to be the same. As Eq. (2.21) needs to hold for every test function, this method is also called weighted residual technique. We expand the residual and use

integration by parts to reduce the second order derivative of the trial function to a first order derivative

$$-\int_0^1 v\frac{\mathrm{d}^2 u_N}{\mathrm{d}x^2}\mathrm{d}x = \int_0^1 vf\mathrm{d}x, \qquad \forall v \in X_0^N \tag{2.22}$$

$$-\left[v\frac{\mathrm{d}u_n}{\mathrm{d}x}\right]_0^1 + \int_0^1 \frac{\mathrm{d}v}{\mathrm{d}x}\frac{\mathrm{d}u_N}{\mathrm{d}x}\mathrm{d}x = \int_0^1 vf\mathrm{d}x, \qquad \forall v \in X_0^N \tag{2.23}$$

thereby reducing the continuity requirements on u_N. Since the test functions fulfill the homogeneous boundary conditions as well, the term evaluated on the boundary vanishes and the *weak formulation* of the problem is obtained.

$$\int_0^1 \frac{\mathrm{d}v}{\mathrm{d}x}\frac{\mathrm{d}u_N}{\mathrm{d}x}\mathrm{d}x = \int_0^1 vf\mathrm{d}x, \qquad \forall v \in X_0^N \tag{2.24}$$

The requirements on the trial space are that the functions as well as their first derivatives are Lebesque-square integrable $\mathcal{L}^2$

$$\mathcal{L}^2 = \left\{v : \int_0^1 v^2\mathrm{d}x < \infty\right\} \tag{2.25}$$

and satisfy the homogeneous boundary conditions, i.e they are a subset of the Sobolov space [15]: $X_0^N \in \mathcal{H}_0^1$, with

$$\mathcal{H}_0^1 = \left\{v : v \in \mathcal{L}^2, \frac{\mathrm{d}v}{\mathrm{d}x} \in \mathcal{L}^2; v(a) = v(b) = 0\right\} \tag{2.26}$$

We discretize the weak formulation (2.24) by expanding the trial and test functions

$$\int_0^1 \frac{\mathrm{d}}{\mathrm{d}x}\left(\sum_{i=1}^{N} v_i\phi_i\right)\frac{\mathrm{d}}{\mathrm{d}x}\left(\sum_{j=1}^{N} u_j\phi_j\right)\mathrm{d}x = \int_0^1 \sum_{i=1}^{N}(v_i\phi_i)\sum_{j=1}^{N}(f_j\phi_j)\mathrm{d}x \tag{2.27}$$

$$\sum_{i=1}^{N}\sum_{j=1}^{N} v_i \int_0^1 \frac{\mathrm{d}\phi_i}{\mathrm{d}x}\frac{\mathrm{d}\phi_j}{\mathrm{d}x}\mathrm{d}x\, u_j = \sum_{i=1}^{N}\sum_{j=1}^{N} v_i \int_0^1 \phi_i\phi_j\mathrm{d}x\, f_j \tag{2.28}$$

$$\sum_{i=1}^{N}\sum_{j=1}^{N} v_i A_{ij} u_j = \sum_{i=1}^{N}\sum_{j=1}^{N} v_i B_{ij} f_i \tag{2.29}$$

and identify the stiffness matrix $A_{ij} = \int_0^1 \phi_i'\phi_j'\mathrm{d}x$ and the mass matrix $B_{ij} = \int_0^1 \phi_i\phi_j\mathrm{d}x$. Using matrix vector notation with the vector of unknown basis coefficients $\underline{u} = (u_1, u_2, \ldots u_N)^T$ to condense the expression, a linear system of equations remains:

$$\underline{v}^T A\underline{u} = \underline{v}^T B\underline{f}, \qquad \forall v \in \mathbb{R}^N \tag{2.30}$$

$$A\underline{u} = B\underline{f} \tag{2.31}$$

The spectral element method differs from finite element methods (FEM) in the choice of the trial space, i.e. the basis functions. For spectral element methods, orthogonality is related to non-overlapping local functions, as for FEM, and additionally due to the analytical nature of their basis functions [15]. Spectral accuracy can be attained for the approximation of smooth functions by selecting eigensolutions to the singular Sturm–Liouville problem [15]. Jacobi polynomials, and in particular Legendre polynomials, are polynomial eigensolutions to the singular Sturm–Liouville problem [15]. The nodal bases for the spectral element method are Lagrange interpolation polynomials on Gauss–Lobatto–Legendre (GLL) quadrature nodes.

On a reference element in the domain $\hat{\Omega} = [-1, 1]$, the GLL nodes are defined as the roots of

$$\left(1 - \xi^2\right) L_N'(\xi) = 0, \qquad \xi \in \hat{\Omega} \tag{2.32}$$

where L'_N is the derivative of the Legendre polynomial of degree N. We construct the Lagrange interpolation polynomials by satisfying the bi-orthonormality relation [15]

$$\pi_i(\xi_j) = \delta_{ij} = \begin{cases} 1, & i = j \\ 0, & i \neq j \end{cases}, \qquad 0 \leq i, j \leq N \tag{2.33}$$

with the Kronecker delta δ_{ij}, so that the individual basis functions, based on the GLL nodes, can be written as

$$\pi_j(\xi) = \frac{-1}{N(N+1)} \frac{\left(1-\xi^2\right) L'_N(\xi)}{(\xi - \xi_j) L_N(\xi)}, \qquad 0 \leq j \leq N, \qquad \xi \in \hat{\Omega} \tag{2.34}$$

They are shown in Fig. 2.1 for a polynomial of degree $N = 7$, portraying the

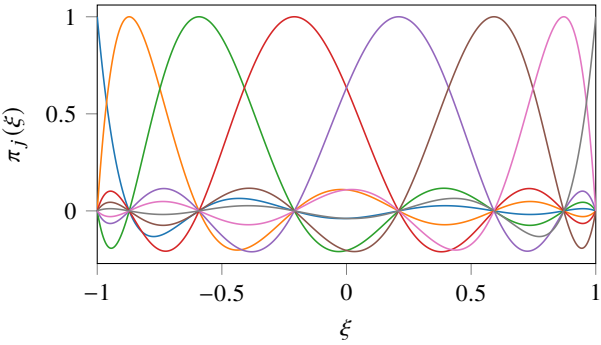

Figure 2.1: Lagrangian interpolation polynomials of degree $N = 7$ based on GLL nodes on the reference element.

bi-orthonormality relation of the basis functions and the location of the GLL nodes for the reference element.

2.2.2 Spatial discretization

An important advantage of multi-domain methods, such as the SEM, is a more flexible domain decomposition compared to single-domain methods. The spatial discretization of a straight pipe section is shown in Fig. 2.2. The

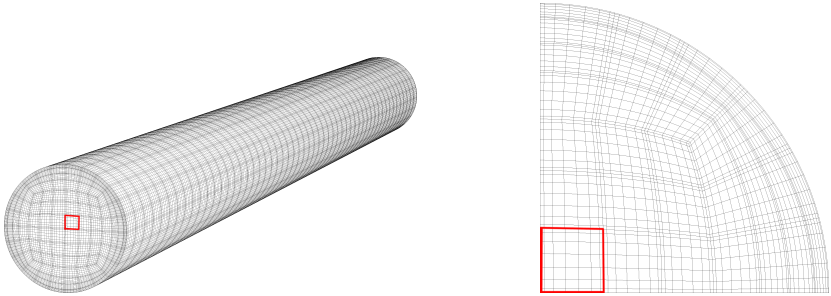

Figure 2.2: Spectral element mesh of a straight pipe section: 3 dimensional view (left) and a quarter of the cross-sectional view (right). The red square marks an individual element.

domain is decomposed into a number of hexahedral elements, as marked by the red square in Fig. 2.2. Within each element, the Lagrange interpolation polynomial uses the GLL nodes to represent the unknowns. The distribution of the GLL nodes is shown by the grid inside each element.

We consider the complete domain by summing over all individual elements where

$$u^e|_{\hat{\Omega}} = u(\xi) = \sum_{j=0}^{N} \pi_j(\xi) u_j^e \tag{2.35}$$

with $u_j^e = u(\xi_j)$ being the nodal values at the GLL nodes. Therefore, the weak formulation of the model problem, Eq. (2.24), becomes

$$\sum_{e=1}^{E}\sum_{i=1}^{N}\sum_{j=1}^{N} v_i^e \int_{\Omega^e} \frac{\mathrm{d}\pi_i}{\mathrm{d}x}\frac{\mathrm{d}\pi_j}{\mathrm{d}x}\mathrm{d}x\; u_j^e = \sum_{e=1}^{E}\sum_{i=1}^{N}\sum_{j=1}^{N} v_i^e \int_{\Omega^e} \pi_i\pi_j \mathrm{d}x\; f_j^e \tag{2.36}$$

$$\sum_{e=1}^{E}\sum_{i=1}^{N}\sum_{j=1}^{N} v_i^e \frac{2}{L^e}\int_{\hat{\Omega}} \frac{\mathrm{d}\pi_i}{\mathrm{d}\xi}\frac{\mathrm{d}\pi_j}{\mathrm{d}\xi}\mathrm{d}\xi\; u_j^e = \sum_{e=1}^{E}\sum_{i=1}^{N}\sum_{j=1}^{N} v_i^e \frac{L^e}{2}\int_{\hat{\Omega}} \pi_i\pi_j \mathrm{d}\xi\; f_j^e \tag{2.37}$$

$$\sum_{e=1}^{E}\sum_{i=1}^{N}\sum_{j=1}^{N} v_i^e A_{ij}^e\; u_j^e = \sum_{e=1}^{E}\sum_{i=1}^{N}\sum_{j=1}^{N} v_i^e B_{ij}^e\; f_j^e \tag{2.38}$$

$$\underline{v}_L^T A_L \underline{u}_L = \underline{v}_L^T B_L \underline{f}_L \tag{2.39}$$

where L^e denotes the length of the element and stems from the transformation between the reference domain $\xi \in \hat{\Omega}$ and the actual element $x \in \Omega^e$, and A^e_{ij} and B^e_{ij} are the element stiffness and mass matrices, respectively. The vector $\underline{u}_L = (\underline{u}^1, \underline{u}^2, ..., \underline{u}^E)^T$ contains the unknowns of all elements ($\underline{v}_L$ similarly). We use Gaussian quadrature on the GLL nodes to evaluate the element mass and stiffness matrices to be

$$B^e_{ij} = \frac{L^e}{2} \int_{\hat{\Omega}} \pi_i \pi_j \mathrm{d}\xi \approx \frac{L^e}{2} \sum_{k=0}^{N} w_k \pi_i(\xi_k) \pi_j(\xi_k) = \frac{L^e}{2} w_i \delta_i \tag{2.40}$$

$$A^e_{ij} = \frac{2}{L^e} \int_{\hat{\Omega}} \frac{\mathrm{d}\pi_i}{\mathrm{d}\xi} \frac{\mathrm{d}\pi_j}{\mathrm{d}\xi} \mathrm{d}\xi = \frac{2}{L^e} \sum_{k=0}^{N} w_k \left.\frac{\mathrm{d}\pi_i}{\mathrm{d}\xi}\right|_{\xi_k} \left.\frac{\mathrm{d}\pi_j}{\mathrm{d}\xi}\right|_{\xi_k} = \frac{2}{L^e} \hat{D}^T \hat{B} \hat{D} \tag{2.41}$$

with the quadrature weights w_k and the differentiation matrix $\hat{D}$ on the reference domain [15]

$$\hat{D}_{ij} = \left.\frac{\mathrm{d}\pi_j}{\mathrm{d}\xi}\right|_{\xi=\xi_i} = \begin{cases} \dfrac{L_N(\xi_i)}{L_N(\xi_j)} \dfrac{1}{\xi_i - \xi_j}, & i \neq j \\ -\dfrac{(N+1)N}{4}, & i = j = 0 \\ \dfrac{(N+1)N}{4}, & i = j = N \\ 0, & \text{otherwise} \end{cases} \tag{2.42}$$

Note that the element mass matrix is diagonal and the numerical quadrature for the element stiffness matrix is exact as the polynomial order of the integrand is $2N - 2 < 2N - 1$.

Continuity requirements, i.e. C^0 continuity at the element interfaces, as well as the Dirichlet boundary conditions are incorporated into the discrete formulation by the Boolean matrices Q and R, respectively, so that the final (global) system of equations can be reformulated with $\underline{u}_L = QR^T \underline{u}$ as

$$RQ^T A_L Q R^T \underline{u} = RQ^T B_L \underline{f}_L \tag{2.43}$$

$$A\underline{u} = B\underline{f}_L \tag{2.44}$$

where it is sufficient to require that $\underline{f} \in \mathcal{L}^2$ as it does not need to fulfill neither C^0 continuity (Q) nor the boundary conditions (R).

2.2.3 Temporal discretization

The model problem for the temporal discretization is the 1D unsteady Burgers equation

$$\frac{\partial u}{\partial t} + u\frac{\partial u}{\partial x} = \nu\frac{\partial^2 u}{\partial x \partial x} \tag{2.45}$$

with initial condition $u(x,0) = u_0(x)$ and homogeneous Dirichlet boundary conditions. We approximate the solution by

$$u_N(x,t) = \sum_{j=1}^{N} \hat{u}_j(t)\pi_j(x) \tag{2.46}$$

Note that we use the Lagrangian interpolation polynomials as basis functions $\pi_j(x)$ and that we consider only a single element. By multiplying the model problem with the test function, integrating over the domain and approximating the solution by $u_N(x,t)$, the weak formulation is recovered

$$\int_\Omega \frac{\partial u_N}{\partial t} v \mathrm{d}x + \int_\Omega u_N \frac{\partial u_N}{\partial x} v \mathrm{d}x = -\int_\Omega \nu \frac{\mathrm{d}v}{\mathrm{d}x}\frac{\mathrm{d}u_N}{\mathrm{d}x}\mathrm{d}x, \qquad \forall v(x) \in X_0^N \tag{2.47}$$

With the mass matrix B and stiffness matrix A, introduced in the previous section, and the convective term (for a single element in the reference domain) written as

$$\sum_{k=0}^{N} w_k \left(\sum_{l=0}^{N}\sum_{m=0}^{N} u_l \pi_l(\xi_k) u_m \left.\frac{\mathrm{d}\pi_m}{\mathrm{d}x}\right|_{\xi_k} \right) \pi_i(\xi_k) = \sum_{m=0}^{N} \underbrace{w_i u_i \hat{D}_{im}}_{\hat{C}_{im}} u_m \tag{2.48}$$

the semi-discrete formulation of the model problem becomes

$$B\frac{\mathrm{d}\underline{u}}{\mathrm{d}t} + C\underline{u} = -\nu A\underline{u} \tag{2.49}$$

An explicit scheme is used for the nonlinear term, avoiding Newton linearization, and an implicit scheme for the viscous term, to avoid its severe stability criterion [15]. A combination of backward difference formula (BDFk) for the implicit treatment of the viscous term and extrapolation (EXTk) for the explicit treatment of the convective term is implemented in Nek5000, where k denotes the order of the scheme. BDF3 and EXT3 are given e.g. by Couzy [14]

$$B\frac{\mathrm{d}\underline{u}}{\mathrm{d}t}\bigg|_{n+1} = B\left[\frac{11\underline{u}^{n+1} - 18\underline{u}^{n} + 9\underline{u}^{n-1} - 2\underline{u}^{n-2}}{6\Delta t}\right] \tag{2.50}$$

$$C\underline{u}\big|_{n+1} = -C\left[3\underline{u}^{n} - 3\underline{u}^{n-1} + \underline{u}^{n-2}\right] \tag{2.51}$$

so that the spatially and temporally discretized model problem becomes

$$\begin{aligned}\left(\frac{11}{6}B + \nu\Delta t A\right)\underline{u}^{n+1} = B\left(3\underline{u}^{n} - \frac{3}{2}B\underline{u}^{n-1} + \frac{1}{3}\underline{u}^{n-2}\right)\\ - C\left(3\underline{u}^{n} - 3\underline{u}^{n-1} + \underline{u}^{n-2}\right)\end{aligned} \tag{2.52}$$

2.2.4 Modeling approach for low-Prandtl-number fluids

The governing partial differential equations, i.e. continuity equation, Navier–Stokes equation and an advection-diffusion equation for the temperature are numerically solved as described in the previous chapter. In order to do so, a certain degree of modeling needs to be introduced, which will be discussed in a general way in this subsection and more specific for the particular case of homogeneous thermal boundary conditions in Sec. 3.1.

Conceptually, the simplest way of solving the aforementioned set of partial differential equations is the so-called direct numerical simulation (DNS), where all the relevant scales are resolved spatially and temporally [64]. This approach yields very high accuracy as no auxiliary modeling is required. However, it comes at the cost of necessitating very powerful computational resources due to the imposed resolution requirements. Therefore, it is not applicable to high Reynolds numbers because of the existence of very small scales.

A second approach that is able to overcome this obstacle to a certain degree is the so-called large-eddy simulation (LES), where the energy containing scales are resolved and the dissipative scaled are modeled [64]. A simple,

yet effective, way of providing the missing dissipation due to the coarser resolution compared to the DNS employed in this study can be understood as a special form of an approximate deconvolution model (ADM)[68]. The relaxation term filtering (ADM-RT) works with non-deconvolved quantities in the non-linear terms but provides additional dissipative terms involving the approximate deconvolution operator [71].

The particularity of low-Prandlt-number fluids featuring larger scales in the thermal field than in the velocity field, due to the high thermal diffusivity, facilitates a so-called "hybrid LES/DNS"[49] or "thermal DNS"[27, 28]. In this approach an LES model is used for the velocity field while the thermal scales are fully resolved. Nevertheless, this approach will be denoted (well-resolved) LES in the following chapters instead of "hybrid LES/DNS" as the velocity field, and thus implicitly its resolution, directly influences the thermal field. It is noteworthy though that the thermal scales are resolved in this type of LES. Furthermore, for low Reynolds numbers a DNS is performed as a reference case as discussed in Sec. 3.2.

2.2.5 Scaling and parallelization

Good parallel scaling of Nek5000 has been shown in the literature, for instance by Offermans et al. [55] for a turbulent pipe flow. Additionally, strong scaling tests have been performed on the supercomputer CRAY XC40 (Hazel Hen) at the High-Performance Computing Center in Stuttgart (HLRS) for two DNS test cases: turbulent pipe flow at $Re_\tau = 180$ and streamwise extent of $L_z = 12.5\,D$, and at $Re_\tau = 1000$ with $L_z = 5\,D$. No advection-diffusion equations are solved for temperature fields but only the Navier–Stokes equation, Eq. (2.11), together with the continuity equation, Eq. (2.5). All 24 cores per node have been used with hyperthreading turned off. The averaged time per timestep for each test run together with the number of gridpoints per core is given in Table 2.1. Only data between steps 30 and 95 have been considered for the averaging to exclude effects of restarting and writing out files. The numerical data is visualized in two log-log plots in Figure 2.3. For the smaller test case at $Re_\tau = 180$ linear scaling is observed until 16 nodes with only a slight deviation until 128 nodes similar to what is shown by Offermans et al. [55]. The second test case at $Re_\tau = 1000$ requires a higher resolution of approximately 840×10^6 gridpoints compared to 20×10^6 for the test case at $Re_\tau = 180$. Consequently,

Table 2.1: Time per timestep in seconds and the number of gridpoints per core.

	$Re_\tau = 180$		$Re_\tau = 1000$	
# nodes	time / timestep [s]	# gridpoints / core	time / timestep [s]	gpts/core
2	3.56556	406,000	-	-
4	1.66375	203,000	-	-
8	0.74267	102,000	-	-
16	0.31611	51,000	-	-
32	0.16672	25,000	-	-
64	0.09600	13,000	5.49480	547,000
128	0.05967	6,000	2.72804	273,000
256	0.09820	3,000	1.35472	137,000
512	0.14786	1,500	0.68786	68,000
1024	-	-	0.45534	34,000

because of higher memory requirements the lowest number of nodes possible is 64. Linear scaling is observed until 256 nodes before deviation from the ideal scaling starts. Note that XXT [80] has been selected as the coarse grid solver for both test cases. Additional improvements in performance, especially for the second test case, could be observed when using an algebraic multigrid (AMG) method instead.

2.3 Proper orthogonal decomposition

The proper orthogonal decomposition (POD) is a technique of reduced-order modeling [12]. By employing the POD in analyzing numerical or experimental data, dominant features of the flow can be extracted [31]. A brief introduction, following Holmes et al. [31], is given in this section to understand the main concepts and how to interpret the obtained results.

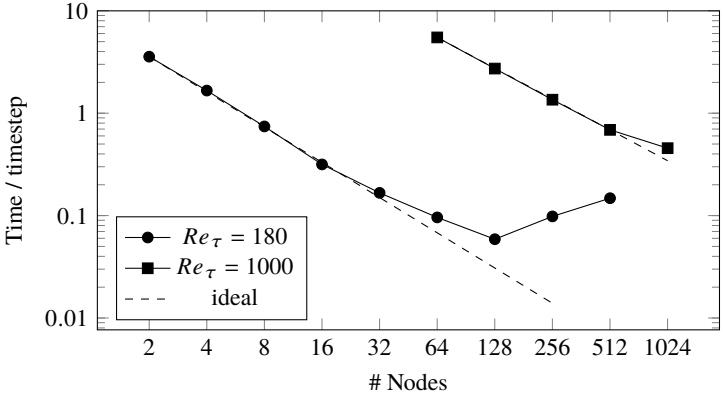

Figure 2.3: Measured time per timestep during scaling tests on Hazel Hen compared to ideal scaling for test cases at $Re_\tau = 180$ and $Re_\tau = 1000$.

Starting point is the idea to represent a dataset, in our case a finite number of instantaneous snapshots of the thermal field, by an *optimal* basis so that each individual snapshot can be reconstructed as

$$\vartheta_M(x,t) = \sum_{j=1}^{M} a_j(t)\phi_j(x) \tag{2.53}$$

Such a representation of the data by an optimal and orthonormal basis $\phi_j(x)$ is not to be confused with the definition of the trial solution in the context of the Galerkin formulation in Eq. (2.18). The task here is to find the optimal basis functions whereas they are given as Lagrange interpolation polynomials based on the GLL nodes in the derivation of the spectral element method (Sec. 2.2). One important feature of the POD is the notion of optimality, meaning that the optimal basis is the one that minimizes the (ensemble) averaged error between the dataset and its projection onto ϕ, resulting in an eigenvalue problem to solve for the basis functions ϕ_j [31]. In the finite-dimensional case with N

grid-points per snapshot and M snapshots, each snapshot is grouped into a vector

$$\boldsymbol{\vartheta}^k = \begin{bmatrix} \vartheta_1^k \\ \vartheta_2^k \\ \vdots \\ \vartheta_N^k \end{bmatrix} \quad \in \mathbb{R}^N, \qquad k = 1, ..., M \tag{2.54}$$

and all snapshots are concatenated in the data matrix X, so that

$$\boldsymbol{X} = [\boldsymbol{\vartheta}^1 \quad \boldsymbol{\vartheta}^2 \qquad \cdots \qquad \boldsymbol{\vartheta}^M] \quad \in \mathbb{R}^{N\,x M} \tag{2.55}$$

The data matrix applied on its transpose $\boldsymbol{X}\boldsymbol{X}^T$ forms the linear operator of the eigenvalue problem

$$\frac{1}{M}\boldsymbol{X}\boldsymbol{X}^T\boldsymbol{\phi} = \lambda\boldsymbol{\phi} \tag{2.56}$$

with eigenvalues λ and eigenfunctions ϕ_j, also known as empirical eigenfunctions or POD modes. This approach is also known as the direct POD.

Depending on the size of the data matrix, alternative ways of determining the POD modes might be computationally favorable. The so-called method of snapshots, introduced by Sirovich [72], solves the eigenvalue problem of the linear operator $\boldsymbol{X}^T\boldsymbol{X} \in \mathbb{R}^{M\,x M}$ instead:

$$\frac{1}{M}\boldsymbol{X}^T\boldsymbol{X}\boldsymbol{a} = \lambda\boldsymbol{a} \tag{2.57}$$

It is therefore advantageous compared to the direct method when the number of snapshots M is less than the number of grid-points N. The direct method and the method of snapshots are both related to the singular value decomposition of the data matrix

$$\boldsymbol{X} = \boldsymbol{U}\boldsymbol{\Sigma}\boldsymbol{V}^T \tag{2.58}$$

which is the discrete matrix form of Eq. (2.53). The columns of the unitary matrices $\boldsymbol{U}$ and $\boldsymbol{V}$ contain the left- singular vectors $\boldsymbol{\phi}$ and right-singular vectors $\boldsymbol{a}$, respectively, while the diagonal matrix $\boldsymbol{\Sigma}$ consists of the non-negative singular values σ_i. The left-singular vectors of $\boldsymbol{X}$ correspond to the POD modes with eigenvalues of $\lambda_i = \sigma_i^2/M$ and $\boldsymbol{\Sigma}\boldsymbol{V}^T$ contains the temporal coefficients.

Another aspect of the optimality of the POD reveals itself in terms of energy contained in the individual modes. When applying the POD on a velocity field, the average kinetic energy (per unit mass) is half of the inner product of the velocity, i.e.

$$\frac{1}{2}\left\langle \int_\Omega uu^* \mathrm{d}x \right\rangle = \frac{1}{2}\left\langle \sum_{ij} a_i a_j^* \int_\Omega \phi_i \phi_j \mathrm{d}x \right\rangle = \frac{1}{2}\sum_i \langle a_i a_i^* \rangle = \frac{1}{2}\sum_i \lambda_i \quad (2.59)$$

where the orthonormality of the basis functions is used and the fact that the temporal coefficients are uncorrelated $\langle a_i a_j^* \rangle = \delta_{ij}\lambda_i$. It can be shown that the average kinetic energy contained within any number of modes M is larger or equal to the average kinetic energy contained within the same number of modes of another representation of the velocity in any other orthonormal basis [31].

Note that the coherent structures identified by the POD and presented in Section 4.2.5 originate from the temperature fluctuations, i.e the mean temperature (average over all snapshots) is subtracted from the thermal field, so that only the temperature fluctuations are decomposed according to Eq. (2.53).

3 The effect of thermal boundary condition types

The first objective, as given in Section 1.3, is to find the appropriate type of thermal boundary condition for a central receiver system operating with liquid metals as a heat transfer fluid. For that reason, three different types of thermal boundary conditions are compared and assessed in detail regarding their influence on the heat transfer in the receiver. The results of this comparison are published by the present author and colleagues in Straub et al. [SSA2] and restated in this chapter. Note that all conclusions drawn from the results in this chapter are merged with the results in the next chapters and collectively given in Chapter 6.

The three types of TBC are the isothermal boundary condition, the mixed-type boundary condition and the isoflux boundary condition. The first to propose and study the mixed-type boundary condition were Kasagi, Tomita, and Kuroda [36], who "performed simulations with a prescribed time-averaged wall heat flux boundary condition in order to mimic the realistic thermal boundary condition (TBC) governed by a conjugate heat transfer problem. This type of boundary condition is sometimes referred to as mixed or mixed-type boundary condition (MBC) because the wall is assumed to be locally isothermal, i.e. temperature fluctuations vanish at the wall, whereas the averaged temperature increases linearly in the streamwise direction similar to isoflux boundary conditions. [...]

The first study comparing the three types of TBCs in a pipe geometry discussed in the following sections, namely MBC, isoflux (IF, where the wall heat flux is constant in time and space) and isothermal (IT, where the wall temperature is constant in time and space) was carried out by Piller [62]. He considered a turbulent pipe flow at a friction Reynolds number of $Re_\tau = u_\tau R/\nu = 180$ and a Prandtl number of $Pr = \nu/\alpha = 0.71$ and concluded that MBC differs from IF

only within the conduction sublayer. It is not known whether this conclusion also holds for low-Prandtl-number fluids or higher Reynolds numbers. [...]

The purpose of the present study is to expand the findings by Piller [62] to higher Reynolds numbers and to lower Prandtl numbers. Low Prandtl numbers are characteristic for liquid metals, which have been proposed as heat transfer fluids in concentrated solar power (CSP) plants by Pacio et al. [58], where accurate predictions of the local wall temperature in the receiver are essential for an efficient design. Therefore, a profound knowledge about the influence of the type of TBC is required in order to select the most appropriate one, depending on the problem to solve. Furthermore, the present database can be useful to develop improved computational models for CSP plants, as in the work by Vinuesa et al. [82]."[SSA2]

3.1 Setup of the homogeneous thermal boundary conditions

The setup is based on the governing equations derived in Sec. 2.1 and solved by the spectral element method described in Sec. 2.2. The particularities for the comparison of different types of homogeneous thermal boundary condition types are described in the following paragraphs.

"The numerical domain is a straight pipe of length 12.5 D with periodic boundary conditions. The set of partial differential equations to be solved are the Navier–Stokes equations for an incompressible Newtonian fluid with constant thermophysical properties together with an advection-diffusion equation for temperature:

$$\frac{\mathrm{D}\tilde{\mathbf{U}}}{\mathrm{D}\tilde{t}} = -\tilde{\nabla}\tilde{p} + \frac{1}{Re_b}\tilde{\nabla}^2\tilde{\mathbf{U}} + \tilde{\mathbf{F}}, \qquad \tilde{\nabla}\cdot\tilde{\mathbf{U}} = 0 \tag{3.1}$$

$$\frac{\mathrm{D}\Theta}{\mathrm{D}\tilde{t}} = \frac{1}{Pe}\tilde{\nabla}^2\Theta + S_\Theta \tag{3.2}$$

The non-dimensional temperature Θ is treated as a passive scalar and viscous dissipation is neglected in the energy equation [44]. Instantaneous velocity $\mathbf{U}$, time t, spatial coordinates $\mathbf{x}$, pressure p and the forcing term $\mathbf{F}$, which

drives the flow at constant bulk velocity, are non-dimensionalized with the bulk velocity U_b and the pipe diameter D as follows:

$$U_b = \frac{1}{A}\int_A U_z \mathrm{dA}, \quad \tilde{\mathbf{U}} = \frac{\mathbf{U}}{U_b}, \quad \tilde{t} = \frac{tU_b}{D}, \quad \tilde{\mathbf{x}} = \frac{\mathbf{x}}{D}, \quad \tilde{p} = \frac{p}{\rho U_b^2}, \quad \tilde{\mathbf{F}} = \frac{\mathbf{F}D}{U_b^2} \tag{3.3}$$

The cross section of the pipe is given by A and U_z is the velocity component in streamwise direction. The bulk Reynolds number and the Péclet number are defined as $Re_b = U_b D/\nu$ and $Pe = U_b D/\alpha$, respectively. The non-dimensional temperature is defined as a scaled temperature difference, employing time-averaged quantities denoted by $\langle\cdot\rangle^t$,

$$\Theta = \frac{\langle T_w\rangle^t - T}{\langle q_w\rangle^t}\rho c_p U_b = \frac{\langle T_w\rangle^t - T}{\langle T_w\rangle^t - T_b}\frac{Pe}{Nu}, \qquad T_b = \frac{\int_A \langle U_z T\rangle^t \mathrm{dA}}{\int_A \langle U_z\rangle^t \mathrm{dA}} \tag{3.4}$$

because in the thermally fully developed region the condition of $\partial\langle\Theta\rangle^t/\partial z = 0$ (as well as $Nu = const.$) is satisfied [8, 62]. Therefore, periodic boundary conditions are also admissible for the thermal field. Wall temperature, wall heat flux and bulk temperature [32] are denoted by T_w, q_w and T_b, respectively. The Nusselt number is defined in the usual way as

$$Nu = \frac{q_w D}{(\langle T_w\rangle^t - T_b)\lambda} \tag{3.5}$$

The three types of thermal boundary conditions (MBC, IF, IT) differ both in the quantity being imposed at the wall

$$T_w = const. \qquad \Theta = 0 \qquad \text{MBC, IT} \tag{3.6}$$

$$q_w = \lambda\frac{\partial T}{\partial r} = const. \qquad \frac{\partial\Theta}{\partial\tilde{r}} = -Pe \qquad \text{IF} \tag{3.7}$$

as well as in the source term S_Θ

$$S_\Theta = \begin{cases} 4\tilde{U}_z & \text{MBC, IF} \\ \tilde{a}\Theta\tilde{U}_z - \frac{1}{Pe}\left(2\tilde{a}\frac{\partial\Theta}{\partial\tilde{z}} - \tilde{a}^2\Theta\right) & \text{IT} \end{cases} \tag{3.8}$$

stemming from the non-dimensionalization [62]. For MBC and IF, the temperature varies linearly in streamwise direction [32]. The implementation of the IT boundary condition follows Piller [62]. For IT, an exponential decay in streamwise direction of the time-averaged difference between bulk and wall temperature is found for negligible net axial conduction [32, 62].

$$\frac{\langle T_w \rangle^t - T_b}{(\langle T_w \rangle^t - T_b)_{\tilde{z}=0}} = \exp(-\tilde{a}\tilde{z}) \tag{3.9}$$

According to Weigand [85], the effect of axial heat conduction can be neglected for $Pe > 100$. For the present simulation of $Pr = 0.025$ the Péclet numbers range from $Pe = 132.5$ to $Pe = 942.5$. The exponential decay rate is given by $\tilde{a}$. A priori, this term is unknown. Therefore, it is evaluated at runtime such that the integral energy balance is satisfied, as proposed by Piller [62]. For the LES of $Re_b = 5300$ the mean and standard deviation for the exponential decay rate are $(0.018732, 8.682219e-05)$ for $Pr = 0.71$ and $(0.156291, 8.103444e-04)$ for $Pr = 0.025$. For $Re_b = 37700$ the mean and standard deviation are $(0.012472, 6.440540e-05)$ for $Pr = 0.71$ and $(0.039238, 1.909494e-04)$ for $Pr = 0.025$. Therefore, due to the averaging in time, necessary anyway for converged statistics, the uncertainty in the exponential decay rate is sufficiently small.

Instantaneous values of velocity and temperature are decomposed into mean and fluctuating parts according to

$$U = \langle U \rangle + u, \qquad \Theta = \langle \Theta \rangle + \vartheta \tag{3.10}$$

If no explicit superscript is given for the averaging, it is performed in time and over the homogeneous directions z and φ. Note that the turbulence statistics in this work were computed using the Nek5000 toolbox developed by Vinuesa et al. [83]. As discussed in Ref. [83], the statistics are collected at runtime, and they are averaged over time and streamwise direction. In a postprocessing step, the averaging in azimuthal direction is performed. Turbulent velocity fields are generated based on a laminar solution with superimposed perturbations [70] using a polynomial order of $N = 5$. The generated field is fed into a simulation with $N = 7$ as initial condition. After a fully-developed state is reached, we begin collecting statistics. The required averaging periods are found in a prestudy where convergence indicators like the deviation of the total shear stress from the analytical one [84] and the residual of the total heat flux balance

[46] are evaluated together with visual inspection of the convergence of the statistics.

The bulk Reynolds number is varied within the range $Re_b = \{5300, 11700, 19000, 37700\}$, corresponding to friction Reynolds numbers of $Re_\tau \approx \{180, 360, 550, 1000\}$. Prandtl number values of $Pr = 0.71$, representing air, and $Pr = 0.025$, representing a class of liquid metals such as lead-bismuth eutectic, mercury or gallium-indium-tin [50], are selected. In case of $Re_b = 5300$, a DNS has been conducted with a resolution in streamwise, azimuthal and wall-normal direction of $\Delta z^+ < 9.4$, $\Delta(R\varphi)^+ < 4.9$ and $\Delta y^+ < 4.5$, respectively, similar to the one employed by El Khoury et al. [17] to setup a reference case. The superscript $^+$ denotes scaling in viscous units, i.e. with the friction velocity u_τ and kinematic viscosity ν. The first point away from the wall is at $\Delta y_1^+ < 0.37$. Well-resolved large-eddy simulations (LESs) are performed for the bulk Reynolds numbers of $Re_b = \{5300, 11700, 19000, 37700\}$. Due to the larger thermal scales for $Pr = 0.025$, the thermal field is still properly resolved for such low Prandtl numbers [28, 49]. The additional dissipation, which needs to be added to the governing equations, is based on a variant of the approximate deconvolution model presented by Schlatter, Stolz, and Kleiser [71] and recently tested and applied in an LES of an airfoil by Negi et al. [53]. An additional relaxation term, responsible for the required dissipation, given by $-\chi\mathcal{H}(u)$ and $-\chi\mathcal{H}(\Theta)$ is added to the right hand side of the momentum and temperature Eqs. (3.1) and (3.2), respectively. Here, $\mathcal{H}$ denotes a high-pass spectral filter (applied to the respective field) and χ is a model parameter, adjusted for each Reynolds number according to previous studies [53]. The resolution criteria proposed by Negi et al. [53] are adopted (with a slightly coarser resolution in azimuthal direction) so that $\Delta z^+ < 18$, $\Delta(R\varphi)^+ < 10$, $\Delta y^+ < 11$, and $\Delta y_1^+ < 0.64$ and validated by comparing velocity and thermal statistics at $Re_b = 5300$ with the results of the present DNS as well as a comparison with literature data at $Re_b = 5300$ and $Re_b = 37700$ presented in the following subsection.

Fig. 3.1 shows the distribution of the elements within a quarter of the cross section for the LES at $Re_b = 37700$. Note that the full cross section is used for the simulations. The total number of elements and grid-points for each simulation is summarized in Table 3.1 together with the time-step size Δt. The time-step is kept constant in each simulation at a value so that $CFL \lesssim 0.5$."[SSA2]

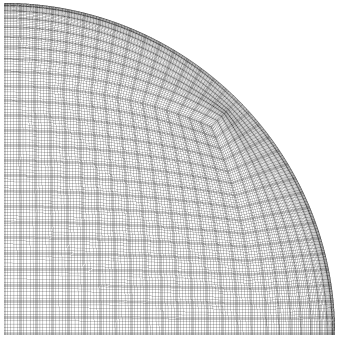

Figure 3.1: Quarter of the cross section of the employed spectral element mesh for the LES at $Re_b = 37700$. Figure taken from Ref. [SSA2].

Table 3.1: Number of elements per cross section nel_{CS}, streamwise direction nel_z and total number of grid points together with the time-step size Δt and the averaging time t_a (taken from Ref. [SSA2]).

Re_b	nel_{CS}	nel_z	grid-points	$\Delta t\, U_b/D$	$t_a\, U_b/D$
5300 (LES)	132	54	3 649 536	2×10^{-3}	8000
5300 (DNS)	384	100	19 660 800	1×10^{-3}	3600
11 700 (LES)	432	105	23 224 320	1×10^{-3}	1600
19 000 (LES)	828	160	67 829 760	5×10^{-4}	1675
37 700 (LES)	2176	290	323 092 480	4×10^{-4}	212

3.2 Validation & Domain Size

"The agreement between statistics of the reference DNS and the well-resolved LES at $Re_b = 5300$ is exemplified in Fig. 3.2. The individual contributions to the budget of the streamwise turbulent heat flux between reference DNS and LES are indistinguishable. Similarly good agreement is found for other statistics (not shown). Therefore, for $Re_b > 5300$ only LESs are performed. It is interesting to note the different behavior of dissipation ϵ and molecular

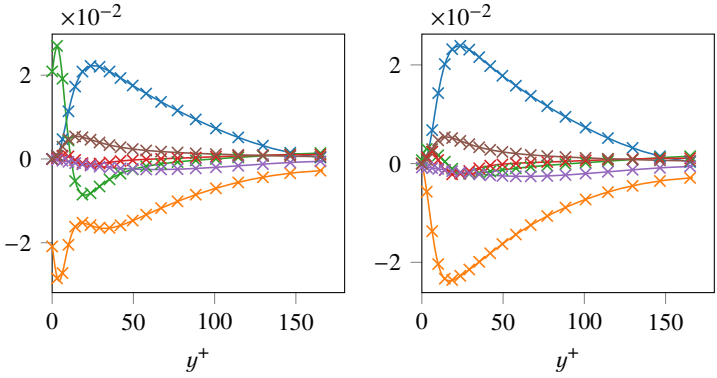

Figure 3.2: Budget of the turbulent heat flux $\langle u_z \vartheta \rangle$ at $Re_b = 5300$ for reference DNS: —— and LES: × at $Pr = 0.025$ of (left) MBC and (right) IF. Individual contributions are P^+: ——, ϵ^+: ——, MD^+: ——, TD^+: ——, TPG^+: ——, S^+: —— as defined in Appendix A.2 Figures taken from Ref. [SSA2]..

diffusion MD contributions close to the wall due to the imposition of a non-fluctuating temperature boundary condition in MBC, as is found by Flageul et al. [19] in channel flow.

For higher Reynolds numbers, velocity statistics of the present LES are compared to literature data from El Khoury et al. [17]. The friction Reynolds number of the present LES, i.e. $Re_\tau = 998.9$, agrees well with that of the DNS [17], which is $Re_\tau = 999.0$. The budget of the turbulent kinetic energy for the case at the highest considered Reynolds number of $Re_b = 37700$ is shown in Fig. 3.3. The individual contributions are defined as in El Khoury et al. [17] and restated for completeness in Appendix A.2. Note that the wall-normal location is limited to $0 < y^+ < 180$, since for $y^+ > 180$ mainly production and dissipation balance [17]. Except for a slightly too low dissipation of the present LES (maximum 7% lower in magnitude), the agreement is excellent. Based on this agreement we term the present LES well-resolved.

In order to validate the implementation of the thermal boundary conditions, the present results are compared to literature data. Fig. 3.4 shows the mean temperature $\langle \Theta \rangle^+$, the temperature variance $\langle \vartheta\vartheta \rangle^+$ and the turbulent heat fluxes in radial and streamwise direction $\langle u_r \vartheta \rangle^+$, $\langle u_z \vartheta \rangle^+$, respectively. The mean temperature and radial turbulent heat flux show good agreement with data

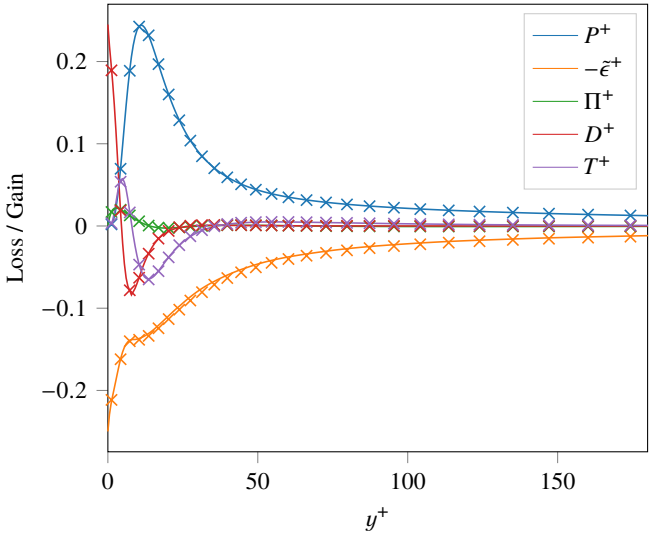

Figure 3.3: Budget of turbulent kinetic energy at $Re_b = 37700$ compared to reference DNS data by El Khoury et al. [17]: × scaled in viscous units. Individual contributions are defined in Appendix A.2. Figure taken from Ref. [SSA2].

from Piller [62] for all TBCs considered. Peak values of temperature variance and streamwise turbulent heat flux appear to be underpredicted by Piller [62] who applied a second order finite volume method in a rather short pipe of $6.328\,D$. A more recent simulation for IF by Antoranz et al. [4], who applied the same high-order method as the one considered in this work for the same domain size, shows good agreement with the present results also for the peak values of temperature variance and streamwise turbulent heat flux.

Another issue is to select the domain size appropriately such that the periodic boundary conditions do not affect the thermal and velocity statistics artificially. In general, the domain size should be large enough to accommodate the largest thermal and flow structures. Two studies dedicated to pipe length requirements are by Chin et al. [13] and Saha et al. [69]. The second study concluded that for thermal statistics, using MBC at a friction Reynolds number of $Re_\tau \approx 170$ and Prandtl numbers of $Pr = 0.025, 0.71, 2.0$, a pipe length of $L_z = 8\pi R \approx 12.5D$ is sufficient to accurately capture up to fourth-order statistics as well as two-

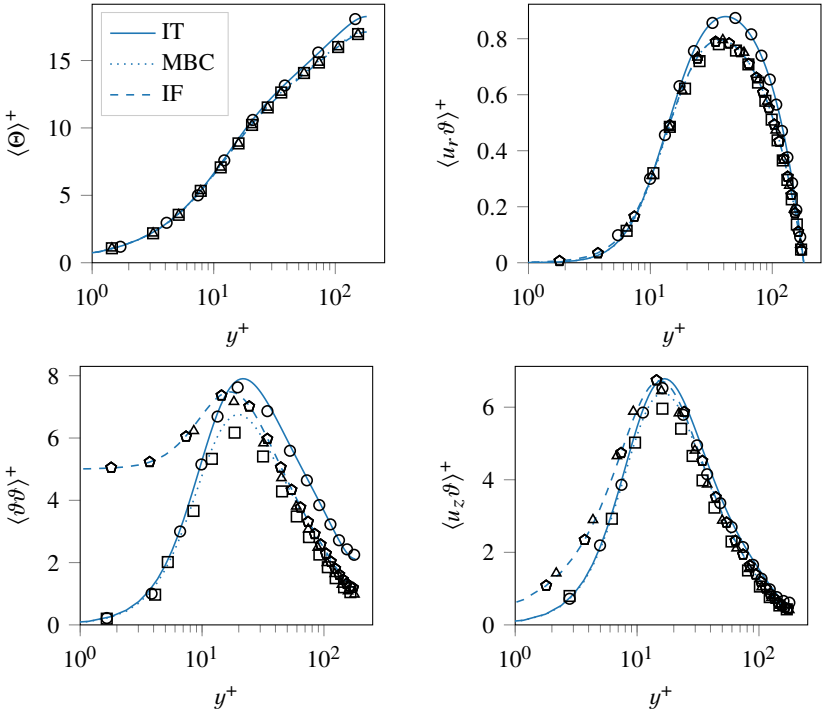

Figure 3.4: Mean temperature, radial turbulent heat flux, temperature variance and streamwise turbulent heat flux scaled in viscous units at $Re_b = 5300$ and $Pr = 0.71$ compared to Piller [62] (IT: ○, MBC: □, IF: △) and Antoranz et al. [4] (IF: ⬠) . Figures taken from Ref. [SSA2].

point correlations. In a recent study considering the computational domain for MBC in a channel flow for $Re_\tau = 500, 1000$ and $Pr = 0.71$, Lluesma-Rodríguez, Hoyas, and Perez-Quiles [46] concluded that even a smaller domain of $2\pi h$, $2h$, $2\pi h$ in streamwise, wall-normal and spanwise direction may be enough to obtain accurate one-point statistics and turbulent budgets, even though the domain is too small for the largest thermal structures. As the previously mentioned studies do not consider IT and IF types of TBC, the streamwise two-point correlations for the thermal fields are assessed in the present work to check for an appropriate domain length. They are shown

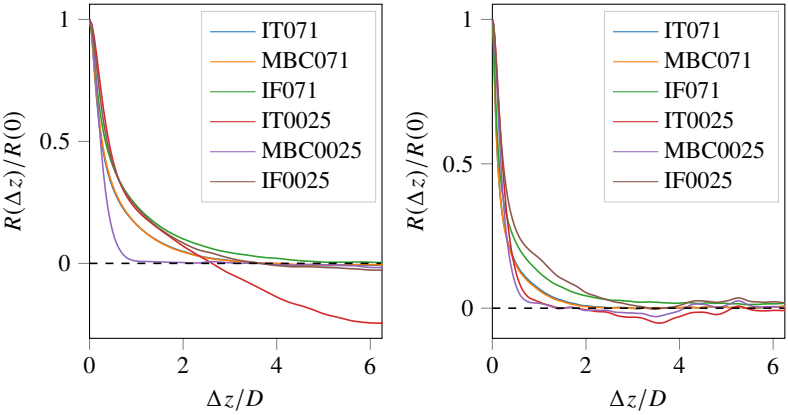

Figure 3.5: Streamwise two-point correlations of thermal fields at wall-normal location of maximum temperature variance for (left) $Re_b = 5300$ and (right) $Re_b = 11700$. Figures taken from Ref. [SSA2].

for $Re_b = 5300$ and $Re_b = 11700$ in Fig. 3.5. Evidently, the two-point correlations for all cases, except for the case of IT at $Re_b = 5300$ and $Pr = 0.025$, vanish at a separation of half the pipe length $\Delta z = 6.25D$, indicating a sufficiently long domain length of $L_z = 12.5D$. Additionally, an LES of a four times longer domain of $L_z = 50D$ shows that even though the streamwise two-point correlations for IT at $Pr = 0.025$ do not vanish, the Nusselt number, mean temperature and turbulent heat fluxes are unaffected. Only the temperature variance at the lower Prandtl number is altered by the longer domain, resulting in a 5% increase of the fluctuations occurring at the wall for IF, as found by Tiselj [75]. For the IT boundary condition at $Pr = 0.025$ the two-point correlations of the temperature fluctuations do not vanish in the longer domain either and the temperature variance in the center of the pipe is about twice as large as in the domain length of $L_z = 12.5D$. Thus, the temperature variance and power spectral density of the isothermal case at $Re_b = 5300$ and $Pr = 0.025$ are excluded from the evaluation in the following section.

An explanation for the non-vanishing two-point correlations of IT, occurring only at the lowest considered Reynolds and Prandtl numbers, most probably is that the assumption of negligible net axial heat conduction, yielding the

exponential decay of the temperature difference in IT, Eq. (3.9), is not valid for such low Péclet numbers and hence the derived source term in Eq. (3.8) is not correct for this particular case. For higher Reynolds numbers, as exemplified on the right diagram for $Re_b = 11700$, all correlations drop to zero within half of the domain length."[SSA2]

3.3 Derivation of the Nusselt number decomposition

As a tool to study the dependency of the Nusselt number on the type of thermal boundary condition, it is decomposed into laminar and turbulent contributions. The derivation given in this section is taken from the appendix of [SSA2].

"The herein presented Nusselt number decomposition closely follows the derivation given by Fukagata, Iwamoto, and Kasagi [24] for MBC in the channel flow. Note that when defining the bulk temperature as in Eq. (3.4), an additional contribution (not present in Ref. [24] but in Ref. [37]) due to the streamwise turbulent heat flux emerges. In order to comply with the nomenclature of Ref. [24], the non-dimensionalization and how to denote (non)-dimensional variables is adopted from Ref. [24] and thus different from the remaining part of this"[SSA2] thesis. "The final form of the derived decomposition is transformed into Eq. (3.39) using the non-dimensionalization as given in Section 3.1.

The following derivation is for MBC and IF. Unfortunately, for the IT boundary condition, such a decomposition into laminar and turbulent contributions was not found due to the more complex source term in the temperature equation, which directly depends on the temperature.

We start our derivation with the transport equation of the temperature T^* in dimensional form

$$\frac{\partial T^*}{\partial t^*} + \nabla^* \cdot (\mathbf{U}^* T^*) = \alpha^* \nabla^{*2} T^* \tag{3.11}$$

Introducing the Reynolds decomposition for temperature and velocity as $T^* = \bar{T}^* + T^{*'}$ and $\mathbf{U}^* = \bar{\mathbf{U}}^* + \mathbf{u}^{*'}$ and applying the averaging operator on Eq. (3.11) yields the RANS equation for temperature in a pipe flow.

$$\frac{\partial \bar{T}^*}{\partial t^*} + \nabla^* \cdot (\bar{\mathbf{U}}\bar{T}^*) = \alpha^* \nabla^{*2} \bar{T}^* - \nabla^* \cdot (\overline{\mathbf{u}^{*'} T^{*'}}) \tag{3.12}$$

In a steady-state, fully-developed pipe flow with homogeneous thermal boundary conditions $\partial(\cdot)/\partial t^* = 0$, $\partial(\cdot)/\partial\varphi = 0$, $\bar{U}_r^* = \bar{U}_\varphi^* = 0$ and all derivatives in streamwise direction vanish except for $\partial\bar{T}^*/\partial z^*$ as the temperature varies (linearly [32]) in the streamwise direction. The remaining terms (now written in index notation for a cylindrical coordinate system) are

$$0 = -\frac{1}{r^*}\frac{\partial}{\partial r^*}\left(r^* \overline{u_r^{*'} T^{*'}}\right) + \alpha^* \left[\frac{1}{r^*}\frac{\partial}{\partial r^*}\left(r^* \frac{\partial \bar{T}^*}{\partial r^*}\right) + \frac{\partial^2 \bar{T}^*}{\partial z^{*2}}\right] - \frac{\partial \bar{U}_z^* \bar{T}^*}{\partial z^*} \tag{3.13}$$

r^*, φ and z^* denote the radial, azimuthal and streamwise direction respectively. Following the non-dimensionalization of Fukagata, Iwamoto, and Kasagi [24], we scale space by the radius of the pipe δ^*, velocity by twice the bulk velocity $2U_b^*$ and the time by $2U_b^*/\delta^*$. Note that this non-dimensionalization is different from the one given in Section 3.1 and is only employed for the Nusselt number decomposition to comply with Ref. [24]. The temperature is expressed as

$$\Theta = \frac{\bar{T}_w^* - T^*}{\Delta T_z^*} \tag{3.14}$$

$$\Delta T_z^* = \frac{q_w^*}{\rho^* c_p^* (2U_b^*)} = \frac{\delta^*}{4}\frac{\mathrm{d}\bar{T}_w^*}{\mathrm{d}z^*} = \frac{\delta^*}{4}\frac{\mathrm{d}\bar{T}_b^*}{\mathrm{d}z^*} \tag{3.15}$$

where the wall heat flux is q_w^* and the relation between the reference temperature ΔT_z^* and the gradient of bulk (or wall) temperature can be found by an integral energy balance of a heated section of length $\mathrm{d}z$. The temperature equation in non-dimensional form, omitting the superscript $(\cdot)^*$, thus becomes

$$0 = -\frac{1}{r}\frac{\partial}{\partial r}\left(r\overline{u_r'\Theta'}\right) + \frac{1}{Re_b Pr}\left[\frac{1}{r}\frac{\partial}{\partial r}\left(r\frac{\partial\bar{\Theta}}{\partial r}\right)\right] + 4\bar{U}_z \tag{3.16}$$

The last term is a result of the (linear) variation of the temperature and acts as a source term such that $\partial\bar{\Theta}/\partial z = 0$. The product of bulk Reynolds number

$Re_b = 2U_b^*\delta^*/\nu^*$, with the kinematic viscosity ν^*, and the Prandtl number $Pr = \nu^*/\alpha^*$ is the Péclet number $Pe = 2U_b^*\delta^*/\alpha^*$. The thermal boundary conditions for the mixed type boundary condition (MBC) and ideal isoflux (IF) are respectively

$$\Theta|_w = \Theta(r = 1) = 0 \tag{3.17}$$

$$\frac{\partial\Theta}{\partial r} = -\frac{\partial\Theta}{\partial y} = -Pe \tag{3.18}$$

In order to relate the Nusselt number and the bulk temperature, first we integrate $\int_0^1$ (3.16) $r\mathrm{d}r$ to find

$$\left.\frac{\mathrm{d}\bar{\Theta}}{\mathrm{dr}}\right|_w = -\left.\frac{\mathrm{d}\bar{\Theta}}{\mathrm{dy}}\right|_w = -Pe \tag{3.19}$$

such that the Nusselt number can be expressed as

$$Nu = \frac{q_w^* D^*}{(\bar{T}_w^* - \bar{T}_b^*)\lambda^*} = \frac{-\lambda^* \left.\frac{\partial\bar{T}^*}{\partial y^*}\right|_w D^*}{(\bar{T}_w^* - \bar{T}_b^*)\lambda^*} \tag{3.20}$$

$$= \frac{\Delta T_z^*}{(\bar{T}_w^* - \bar{T}_b^*)} \left.\frac{\mathrm{d}\bar{\Theta}}{\mathrm{dy}}\right|_w \frac{D^*}{\delta^*} = \frac{2Pe}{\Theta_b} \tag{3.21}$$

The dimensionless bulk temperature is

$$\bar{\Theta}_b = \frac{\int_{A^*} \overline{U_z^*\Theta}\mathrm{d}A^*}{\int_{A^*} \bar{U}_z^*\mathrm{d}A^*} = \frac{\bar{T}_w^* - \bar{T}_b^*}{\Delta T_z^*} \tag{3.22}$$

Next, we apply a triple integral on Eq. (3.16): $\int_1^0(\int_1^r(\int_1^r \eta\mathrm{d}\eta)1/\eta^2\eta\mathrm{d}\eta)\bar{U}_z r dr$, reported here step by step. The first integral is $\int_1^r$ (3.16)$\eta\mathrm{d}\eta$. Note that we integrate from the wall $r = 1$ to the radial location r and that we change the variable in the integrand from r to η because the upper limit of the integral is already given by r.

$$0 = \int_1^r \left[-\frac{\partial}{\partial\eta}\left(\eta\overline{u_r'\Theta'}\right) + \frac{1}{Pe}\left(\frac{\partial}{\partial\eta}\left(\eta\frac{\partial\bar{\Theta}}{\partial\eta}\right)\right) + 4\bar{U}_z\right]\eta\mathrm{d}\eta \tag{3.23}$$

$$= -r\overline{u_r'\Theta'} + \frac{1}{Pe}r\frac{\mathrm{d}\bar{\Theta}}{\mathrm{dr}} + 1 + \Phi \tag{3.24}$$

where we have used the fact that the turbulent heat flux vanishes at the wall, substituted the gradient of Θ at the wall by Eq. (3.19) and introduced the fractional flow rate analogously to Fukagata, Iwamoto, and Kasagi [24]

$$\Phi = 4 \int_1^r \bar{U}_z \eta \mathrm{d}\eta \tag{3.25}$$

The lower and upper limits have been chosen such that we can apply known relations (or facts) at the wall. Switching upper and lower limits is obviously the same but with changed signs. Eq. (3.24) gives us a balance of the radial turbulent heat flux. The second integral should give us a balance of the mean non-dimensional temperature by integrating $\int_1^r$ (3.24) $1/\eta^2 \eta \mathrm{d}\eta$.

$$0 = \int_1^r \left[-\overline{u_r' \Theta'} + \frac{1}{Pe} \frac{\mathrm{d}\bar{\Theta}}{\mathrm{d}\eta} + \frac{1}{\eta}(1+\Phi) \right] \mathrm{d}\eta \tag{3.26}$$

$$= -\int_1^r \overline{u_r' \Theta'} \mathrm{d}\eta + \frac{1}{Pe}\bar{\Theta} + \int_1^r \frac{1}{\eta}(1+\Phi)\mathrm{d}\eta \tag{3.27}$$

where we have used the boundary condition, Eq. (3.17). Note that the mean non-dimensional temperature, evaluated at the wall, has to vanish for MBC due to the boundary condition, Eq. (3.17), but also for IF due to the definition of Θ. The third integral should give us a balance of the Nusselt number. Therefore, we have to construct it such that we find the non-dimensional bulk temperature, which is related to the Nusselt number by Eq. (3.21), by integrating $\int_1^0$ (3.27) $\bar{U}_z r \mathrm{d}r$

$$0 = -\int_1^0 \int_1^r \overline{u_r' \Theta'} \mathrm{d}\eta \bar{U}_z r \mathrm{d}r + \frac{1}{Pe} \int_1^0 \bar{\Theta} \bar{U}_z r \mathrm{d}r + \int_1^0 \int_1^r \frac{1}{\eta}(1+\Phi)\mathrm{d}\eta \bar{U}_z r \mathrm{d}r \tag{3.28}$$

$$\frac{1}{Nu} = \frac{1}{2} \int_1^0 (1+\Phi)\overline{u_r' \Theta'} \mathrm{d}r - \frac{1}{2} \int_1^0 \frac{1}{r}(1+\Phi)^2 \mathrm{d}r + \frac{2}{Pe} \int_0^1 \overline{u_z' \Theta'} r \mathrm{d}r \tag{3.29}$$

where we have used partial integration to reformulate the double integrals to a single integral and used that $\Phi(0) = -1$. The second term in Eq. (3.28) gives rise to the bulk temperature, and thus the Nusselt number, as well as a contribution due to the turbulent heat flux because $\bar{\Theta}\bar{U}_z = \overline{\Theta U_z} - \overline{\Theta' u_z'}$.

The laminar contribution is inside the second integral of Eq. (3.29) and in order to decompose it from the turbulent contribution, the streamwise velocity and the fractional flow rate need to be decomposed into a laminar and turbulent contribution

$$\bar{U}_z = \bar{U}_L + \bar{U}_t \tag{3.30}$$

$$\Phi(r) = \Phi_L + \Phi_T = 4\int_1^r \bar{U}_L \eta \mathrm{d}\eta + 4\int_1^r \bar{U}_T \eta \mathrm{d}\eta \tag{3.31}$$

Although the approach of decomposing the mean velocity profile into a corresponding laminar one and the deviation between these two profiles is not widely used in literature, it was also successfully applied for data analysis in other studies [16, 25]. The laminar velocity profile is

$$\bar{U}_L = 1 - r^2 \tag{3.32}$$

such that the laminar fractional flow rate can be evaluated to

$$\Phi_L = 2\left(r^2 - \frac{r^4}{2} - \frac{1}{2}\right) \tag{3.33}$$

To find an expression for the turbulent velocity profile, the complete velocity profile, taken from the derivation of the friction coefficient C_f for a fully-developed pipe flow [23] by taking the balance equation for the mean velocity profile (after the second of the three integrals) and replacing C_f, has to be known

$$C_f = \frac{16}{Re_b} + 16\int_0^1 2r\overline{u_r' u_z'} r \mathrm{dr} \tag{3.34}$$

$$\bar{U}_z = Re_b\left[\int_1^r \overline{u_r' u_z'} \mathrm{d}\eta - \frac{C_f}{16}(r^2 - 1)\right] \tag{3.35}$$

$$\bar{U}_z = Re_b \int_1^r \overline{u_r' u_z'} \mathrm{d}\eta - (r^2 - 1)\left[1 + Re_b \int_0^1 2r\overline{u_r' u_z'} r \mathrm{dr}\right] \tag{3.36}$$

such that the turbulent velocity profile is

$$\bar{U}_T = \bar{U}_z - \bar{U}_L = Re_b\left[(1 - r^2)\int_0^1 2r\overline{u_r' u_z'} r \mathrm{dr} + \int_1^r \overline{u_r' u_z'} \mathrm{d}\eta\right] \tag{3.37}$$

Finally, laminar and turbulent fractional flow rate are introduced into Eq. (3.29) where the contributions containing Φ_L can be evaluated analytically.

$$\begin{aligned}\frac{1}{Nu} = \frac{11}{48} - \frac{1}{2}\int_0^1 (1+\Phi)\overline{u_r'\Theta'}\mathrm{dr} \\ - \frac{1}{2}\int_0^1 \frac{1}{r}\left[(2r^4 - 4r^2)\Phi_T - \Phi_T^2\right]\mathrm{dr} + \frac{2}{Pe}\int_0^1 \overline{u_z'\Theta'}r\mathrm{dr}\end{aligned} \tag{3.38}$$

Hence, the Nusselt number is composed of four contributions: the laminar part $48/11$, the contribution due to the radial turbulent heat flux, a contribution solely due to the turbulent velocity field and a contribution due to the streamwise turbulent heat flux. The third term can be interpreted as a modification of the bulk temperature due to a different mean velocity profile as compared to the laminar one [37]. It arises from the streamwise variation of the mean axial advective heat flux $\partial \bar{U}_z^* \bar{T}^* / \partial z^*$ (c.f. eq. 3.13) which is also the source of the laminar contribution."[SSA2]

3.4 Results and Discussion

The results are taken from the publication by Straub et al. [SSA2] and are repeated in the following subsections, presenting the "(decomposed) Nusselt number, first- and second-order statistics and spectral analysis."[SSA2]

3.4.1 Nusselt Number

"Depending on the flow and the fluid (i.e. Re and Pr), correlations exist to predict the Nusselt number such as the Gnielinski correlation for fully-developed turbulent flow valid in the range of $10^4 < Re_b < 10^6$ and $0.1 < Pr < 1000$ [81]. The range of validity can be extended up to lower Reynolds numbers ($Re_b = 2300$) by interpolation of laminar and turbulent Nusselt numbers as described in [81]. Note that such an interpolation is not performed when comparing the correlation with the present results even though the lowest Reynolds number is $Re_b = 5300 < 10^4$ since the agreement is very good with the non-interpolated correlation.

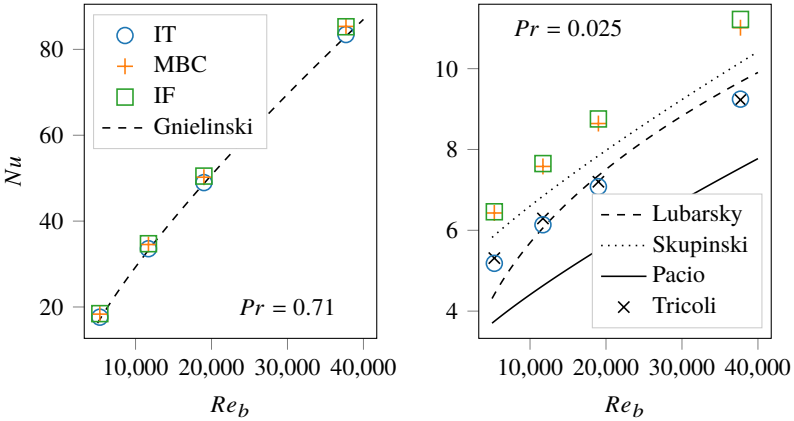

Figure 3.6: Nusselt number variation with Re_b. Figures taken from Ref. [SSA2].

For low-Prandtl-number fluids existing correlations have been assessed by Pacio, Marocco, and Wetzel [57]. As pointed out in their study, there are few reliable experimental data for the fully-developed thermal field of the IT boundary condition using liquid metals. They propose their own correlation as a best-fit of the collected experimental data in the range of $Pe = 450 - 8000$. Alternatively, Tricoli [79] proposed a theoretical relationship between the Nusselt number for IF and IT: $Nu_{IT} = \pi^2/12\, Nu_{IF}$, valid for low Prandtl numbers and high Péclet numbers. Two recommended correlations [57] for IF are the ones by Skupinski, Tortel, and Vautrey [73] (measured range of $Pe = 58 - 13100$ for NaK in hydrodynamically and thermally fully-developed horizontal pipe flow) and Lubarsky and Kaufman [48] (best fit of experimental data).

Fig. 3.6 shows a comparison of the present results to these selected correlations. The left figure shows the Nusselt number for $Pr = 0.71$. For this Prandtl number, the different types of TBCs do not influence the Nusselt number and they are accurately predicted by the Gnielinski correlation. This can be explained by the dominance of turbulent mixing over conduction for medium and high Prandtl numbers (as is discussed in the following section for MBC and IF). The right figure shows the Nusselt number for $Pr = 0.025$. For this Prandtl number, the present results show a significant effect of the TBC even

on a global quantity as the Nusselt number. The Nusselt numbers of MBC agree well with IF, but the Nusselt number of IT is significantly lower. For such low Prandtl numbers and moderately high Reynolds numbers, typical of engineering applications, the contribution of conduction to the heat transfer is comparable to that of turbulent mixing, resulting in different Nusselt numbers depending on the applied boundary condition at the wall. This is analogous to the laminar convective case, where for fully-developed laminar pipe flow $Nu = 3.66$ for IT and $Nu = 4.36$ for IF [32]. For the bulk Reynolds numbers of $Re_b = \{5300, 11700, 19000, 37700\}$ the Nusselt number of IT is $\{19.8\%, 19.7\%, 19.2\%, 17.5\%\}$ lower than that for IF and MBC, respectively, indicating a converging trend for higher Reynolds numbers. A possible explanation for this trend is the dominance of turbulent mixing over molecular conduction for increasing Reynolds numbers, as observed for $Pr = 0.71$. For a conclusive statement however, even higher Reynolds numbers should be investigated for low-Prandtl-number fluids.

Besides, the correlations by Lubarsky and Kaufman [48] and Skupinski, Tortel, and Vautrey [73] for IF underpredict the Nusselt numbers as well as the one for IT from Pacio, Marocco, and Wetzel [57]. The theoretical relationship between the Nusselt numbers of IF and IT from Tricoli [79] however, predicts the Nusselt numbers of IT well (based on the present values of IF). According to the present Nusselt number results, more accurate correlations for liquid metals, eventually based on reliable experimental or numerical data, are necessary. Although the numerical results in this study may not be sufficient to propose a new correlation, they serve as a reference to test state-of-the-art correlations and extend the openly available data for liquid metals."[SSA2]

3.4.2 Decomposition of the Nusselt Number

"Similarly to the Fukagata–Iwamoto–Kasagi (FIK) identity for the skin-friction coefficient [23], also the Nusselt number can be decomposed into laminar and turbulent contributions [24, 37]."[SSA2]

The derivation given in Section 3.3 is used to analyze in detail the individual contributions and how they are affected by the type of thermal boundary condition. When rewriting the decomposed formulation by "using the non-

dimensionalization listed in Section 3.1, the Nusselt number is decomposed into

$$\begin{aligned}\frac{1}{Nu} = &\underbrace{\frac{11}{48}}_{1/Nu_L} - \underbrace{\int_0^{0.5} (1+\tilde{\Phi})\langle \tilde{u}_r \vartheta \rangle \mathrm{d}\tilde{\mathrm{r}}}_{1/Nu_{HF,r}} \\ &\underbrace{- \frac{1}{2}\int_0^{0.5} \frac{1}{\tilde{r}} \left[(2\tilde{r}^4 - \tilde{r}^2) 16 \tilde{\Phi}_T - \tilde{\Phi}_T^2 \right] \mathrm{d}\tilde{\mathrm{r}}}_{1/Nu_{RSS}} + \underbrace{\frac{8}{Pe}\int_0^{0.5} \langle \tilde{u}_z \vartheta \rangle \tilde{r} \mathrm{d}\tilde{\mathrm{r}}}_{1/Nu_{HF,z}}\end{aligned} \tag{3.39}$$

The four contributions to the inverse Nusselt number in eq. (3.39) are the laminar term Nu_L, the contribution due to the radial turbulent heat flux $Nu_{HF,r}$, the contribution due to the turbulent velocity field Nu_{RSS} (where $\tilde{\Phi}$ is the fractional flow rate of the velocity field and $\tilde{\Phi}_T$ the fractional flow rate of the turbulent velocity field, as described in [Section 3.3] and the contribution due to the streamwise turbulent heat flux $Nu_{HF,z}$, respectively. Since the turbulent velocity field can be expressed by the Reynolds shear stress (RSS) [see Section 3.3], the fractional flow rate Φ_T and consequently Nu_{RSS} are only affected by the RSS and no thermal statistics. Note that due to the inverse relationship, the individual contributions cannot be summed together to determine the Nusselt number in contrast to the contributions of the decomposed skin friction coefficient [23]. For instance, a higher radial turbulent heat flux increases the second term on the right hand side of eq. (3.39), so that a higher value is subtracted from 11/48, thereby reducing the right hand side of eq. (3.39). This results in an increase of the Nusselt number because of the inverse relationship. In order to visualize and compare the individual contributions and to highlight the different heat transfer mechanism of low-Prandtl-number fluids, Eq. (3.39) is reformulated as

$$1 = \frac{Nu_L}{Nu} + \frac{Nu_L}{Nu_{HF,r}} + \frac{Nu_L}{Nu_{RSS}} - \frac{Nu_L}{Nu_{HF,z}} \tag{3.40}$$

with the individual ratios shown in Fig. 3.7. Note that a higher Nusselt number (i.e. lower Nu_L/Nu) is achieved by larger ratios $Nu_L/Nu_{HF,r}$ and Nu_L/Nu_{RSS}. The separate analysis of each of the three turbulent contributions highlights the different heat transfer mechanism of the two investigated Prandtl number fluids. Note that the contribution due to the streamwise turbulent heat

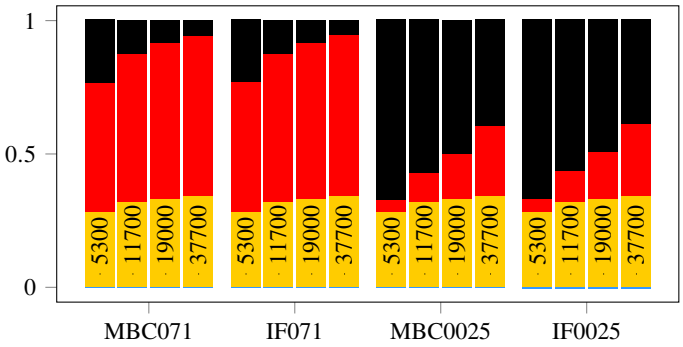

Figure 3.7: Individual contributions to the Nusselt number: Nu_L/Nu: ■, $Nu_L/Nu_{HF,r}$: ■, Nu_L/Nu_{RSS}: ■, $Nu_L/Nu_{HF,z}$: ■ Figure taken from Ref. [SSA2].

flux is one to two orders of magnitude smaller than the other contributions and its effect on the Nusselt number is negligible for the present simulations. The third term in eq. (3.40) only depends on the velocity field through the Reynolds shear stresses and is thus independent of the Prandtl number for forced convection. For the Reynolds numbers considered in the present study, it ranges from 28% to 34%. The ratio determining the contribution due to the radial turbulent heat flux $Nu_L/Nu_{HF,r}$ is the dominant contribution to the Nusselt number for $Pr = 0.71$ with values ranging from 48% to 60%. For $Pr = 0.025$, the contribution due to the radial turbulent heat flux only becomes relevant for higher Reynolds numbers with values of $Nu_L/Nu_{HF,r}$ ranging from 4% to 27%. Therefore, for the Reynolds numbers considered in the present study, the increase in Nusselt number for $Pr = 0.025$ with respect to the laminar Nusselt number is mainly caused by the contribution due to the turbulent velocity field and not the contribution due to the radial turbulent heat flux.

The individual contributions, the Nusselt number defined in eq. (3.39) and the Nusselt number evaluated directly by the bulk temperature as shown in [Section 3.3] are given in Table 3.2. The agreement between the directly evaluated Nusselt number and the one from eq. (3.39) is good in all cases except for $Pr = 0.71$ at $Re_b = 37700$ where the Nusselt number is underestimated. This

Table 3.2: Individual contributions, Nusselt number defined in eq. (3.39) and Nusselt number evaluated directly in parentheses. The bulk Reynolds number increases from top to bottom (Re_b = 5300, 11700, 19000, 37700) (taken from Ref. [SSA2]).

	$1/Nu_{HF,r}$	$1/Nu_{RSS}$	$1/Nu_{HF,z}$	Nu
MBC071	1.11×10^{-1}	6.45×10^{-2}	7.68×10^{-4}	18.3 (18.3)
IF071	1.11×10^{-1}	6.45×10^{-2}	8.13×10^{-4}	18.4 (18.5)
MBC0025	9.86×10^{-3}	6.45×10^{-2}	8.04×10^{-4}	6.43 (6.43)
IF0025	1.09×10^{-2}	6.45×10^{-2}	1.16×10^{-3}	6.46 (6.46)
MBC071	1.27×10^{-1}	7.31×10^{-2}	2.67×10^{-4}	34.5 (34.5)
IF071	1.28×10^{-1}	7.31×10^{-2}	2.78×10^{-4}	34.7 (34.7)
MBC0025	2.49×10^{-2}	7.31×10^{-2}	8.05×10^{-4}	7.58 (7.58)
IF0025	2.64×10^{-2}	7.31×10^{-2}	1.04×10^{-3}	7.65 (7.65)
MBC071	1.33×10^{-1}	7.59×10^{-2}	1.50×10^{-4}	50.2 (50.2)
IF071	1.34×10^{-1}	7.59×10^{-2}	1.56×10^{-4}	50.4 (50.5)
MBC0025	3.83×10^{-2}	7.59×10^{-2}	7.91×10^{-4}	8.64 (8.64)
IF0025	4.00×10^{-2}	7.59×10^{-2}	1.00×10^{-3}	8.75 (8.75)
MBC071	1.37×10^{-1}	7.85×10^{-2}	7.15×10^{-5}	74.5 (85.3)
IF071	1.38×10^{-1}	7.85×10^{-2}	7.47×10^{-5}	79.0 (85.3)
MBC0025	6.00×10^{-2}	7.85×10^{-2}	7.12×10^{-4}	11.0 (11.0)
IF0025	6.12×10^{-2}	7.85×10^{-2}	8.72×10^{-4}	11.1 (11.2)

discrepancy could be caused by the high sensitivity of the Nusselt number evaluated using Eq. (3.39) on the radial turbulent heat flux distribution for high Reynolds numbers. Due to the inverse relation given by Eq. (3.39), the determined Nusselt number becomes more sensitive to deviations in $1/Nu_{HF,r}$ as the sum of the three turbulent contributions approaches its upper bound 11/48. For the cases of $Re_b = 37700$ and $Pr = 0.71$ an amplified $\langle \tilde{u}_r \vartheta \rangle$ of $\approx 1\%$ yields the correct Nusselt number illustrating its high sensitivity. Additionally, the influence of the contribution due to the turbulent velocity field is tested. When using the DNS data of El Khoury et al. [17] for these two cases to determine $1/Nu_{RSS}$ and the fractional flow rate $\tilde{\Phi}$, the Nusselt

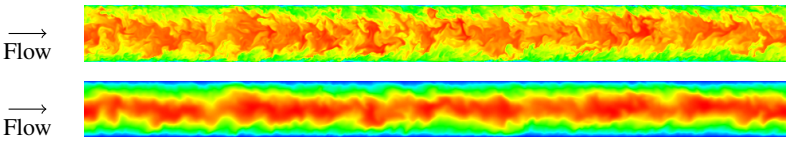

Figure 3.8: Instantaneous visualisations of the temperature Θ at $Re_b = 19000$ of MBC at (top) $Pr = 0.71$ and at (bottom) $Pr = 0.025$, scaled with individual maximum. Red (blue) regions indicate high (low) values. Figures taken from Ref. [SSA2].

number is still underestimated, so that indeed a slightly too low radial turbulent heat flux could be responsible for the observed discrepancy.

A decomposition for IT was not found due to the complex source term in Eq. (3.8), but the mean temperature budget, discussed in the following subsection, includes IT. Nevertheless, an explanation for the significant differences between the Nusselt numbers of IT and MBC/IF can be inferred because also for IT, it can be assumed that the Nusselt number consists of a laminar and a turbulent contribution. The laminar contribution, which prevails in determining the Nusselt number for low Prandtl numbers at the Reynolds numbers considered here, is lower for IT than for MBC/IF, such that also the Nusselt number is lower.

Even though the Nusselt numbers for $Pr = 0.025$ are larger than analytically found for the laminar case, the thermal field is still in a laminar-like state. Such a laminar-like thermal field can be observed in the instantaneous snapshots in Fig. 3.8 which correspond to the MBC at $Pr = 0.71$ and at $Pr = 0.025$ at $Re_b = 19000$. Indeed, while for $Pr = 0.71$ large and small scales with sharp gradients are recognizable, for $Pr = 0.025$ the small scales are smeared out by the high thermal diffusivity [75], resulting in a much smoother temperature field, resembling a laminar one."[SSA2]

3.4.3 Turbulence Statistics

"In addition to the effect of the TBCs on the Nusselt number as a global parameter, first- and second-order one-point statistics are compared in the following paragraphs. To distinguish the TBCs in the following diagrams, different line styles are used while the Reynolds number is distinguished by the

Table 3.3: Line styles and colors of Reynolds numbers and thermal boundary conditions (taken from Ref. [SSA2]).

	$Re_b = 5300$	$Re_b = 37700$
IT	———	———
MBC	·····	·····
IF	- - -	- - -

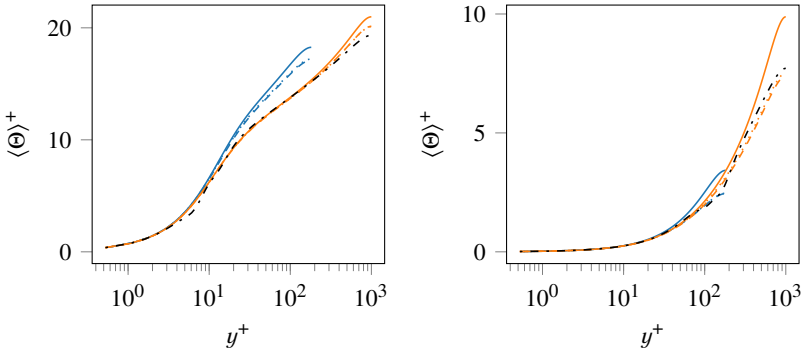

Figure 3.9: Mean temperature variation with TBC and Re_b for (left) $Pr = 0.71$ and (right) $Pr = 0.025$. Line styles and colors as in Table 3.3. Empirical correlation by Kader [34]: - · - · - . Figures taken from Ref. [SSA2].

line color, as summarized in Table 3.3. In order to keep the different profiles for each TBC and Reynolds number clearly distinguishable, the following diagrams only show results for lowest and highest Reynolds number. Results of the intermediate Reynolds numbers are provided in the database [SSD1].

The temperature distribution is presented in Fig. 3.9. Scaling in viscous units is done by substituting the bulk velocity U_b by the friction velocity u_τ in the definition of the non-dimensionalized temperature in Eq. (3.4), i.e. $\Theta^+ = \Theta u_\tau / U_b$. For both Prandtl numbers, MBC and IF yield very similar temperature profiles irrespective of the Reynolds number. However, the temperature profile of IT deviates from the other two by higher values in the core

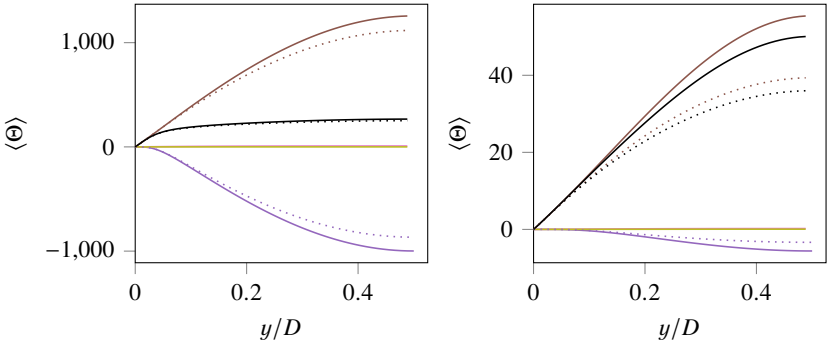

Figure 3.10: Mean temperature budget of IT and MBC at $Re_b = 11700$ (left) $Pr = 0.71$ and (right) $Pr = 0.025$. Contributions are due to radial turbulent heat flux: ——, mean advective heat flux: ——, turbulent axial advective heat flux: —— and mean streamwise thermal diffusion: ——. Their sum is equal to $\langle\Theta\rangle$: ——. Line styles as in Table 3.3. Figures taken from Ref. [SSA2].

region (cf.[62]), an effect which is especially pronounced at $Pr = 0.025$. A higher temperature for IT compared to MBC/IF in the center of the pipe at low Prandtl numbers ($\approx 33\%$ at $Re_b = 37700$) reflects the previously discussed lower Nusselt numbers of IT. Neither buffer layer nor logarithmic layer are visible for $Pr = 0.025$ (cf. [1]). The empirical correlation by Kader [34] (only shown for $Re_b = 37700$) agrees well with the present data for IF/MBC at both Prandtl numbers (cf. [1]).

Even though a decomposition of the Nusselt number for IT was not found, the budget equation for the mean temperature given by Ref. [62] reads:

$$\langle\Theta\rangle^t(\tilde{r}) = -Pe\int_{r'=\tilde{r}}^{0.5}\langle\tilde{u}_r\vartheta\rangle \mathrm{d}r' + Pe\int_{r'=\tilde{r}}^{0.5}\frac{1}{r'}\int_{r''=0}^{r'} r''\langle S_\Theta\rangle \mathrm{d}r''\mathrm{d}r' \qquad (3.41)$$

Eq. (3.41) can be used to analyze the different contributions to the mean temperature, as illustrated in Fig. 3.10 for $Re_b = 11700$ and both IT and MBC, while IF is not shown because it practically coincides with MBC. The dominant terms are the contributions due to the radial turbulent heat flux $\langle\tilde{u}_r\vartheta\rangle$ and the mean advective heat flux stemming from the source term, $4\langle\tilde{U}_z\rangle$ for MBC and IF, and $\tilde{a}\langle\tilde{U}_z\rangle\langle\Theta\rangle$ for IT. Their difference determines the distribution

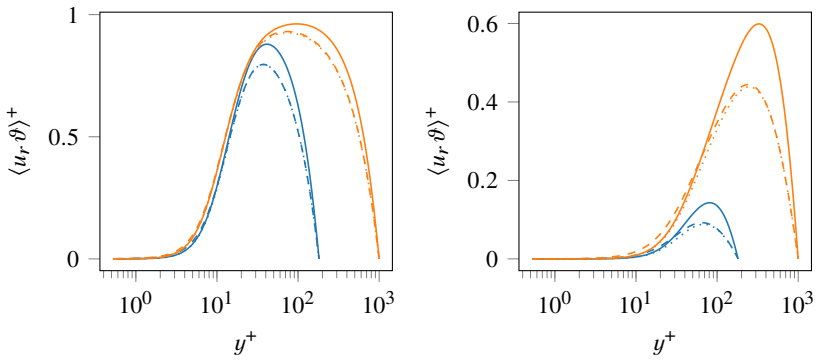

Figure 3.11: Variation of radial turbulent heat flux with TBC and Re_b for (left) $Pr = 0.71$ and (right) $Pr = 0.025$. Line styles and colors as in Table 3.3. Figures taken from Ref. [SSA2].

of $\langle\Theta\rangle$ and hence its dependency on the TBC. For both Prandtl numbers, the contributions due to turbulent axial advective heat flux $\tilde{a}\langle\tilde{u}_z\vartheta\rangle$ and mean streamwise thermal diffusion $\tilde{a}^2\langle\Theta\rangle/Pe$ are negligible, as reported by Piller [62] for $Pr = 0.71$. At $Pr = 0.71$ a slightly higher (in magnitude) contribution due to the radial turbulent heat flux for IT, compared to MBC, is compensated by the higher (in magnitude) contribution due to the mean advective heat flux such that the temperature profiles are barely distinguishable. At $Pr = 0.025$ however, the higher (in magnitude) contribution due to the radial turbulent heat flux for IT, compared to MBC, is overcompensated by the contribution due to the mean advective heat flux, yielding the observed higher temperature and consequently lower Nusselt number compared to MBC/IF. Note that since for IT the mean advective heat flux directly depends on the temperature, these two are interrelated such that a higher temperature yields a higher mean advective heat flux and vice versa. The sum of the contributions shown in Fig. 3.10 is the mean temperature $\langle\Theta\rangle$, which clearly shows the flat (turbulent) profile at $Pr = 0.71$ and the more rounded (laminar-like) profile at $Pr = 0.025$.

Fig. 3.11 shows the effect of the TBC and Reynolds number on the radial turbulent heat flux. For both Prandtl numbers, IT yields higher radial turbulent heat fluxes whereas MBC and IF nearly collapse. Therefore, the Nusselt

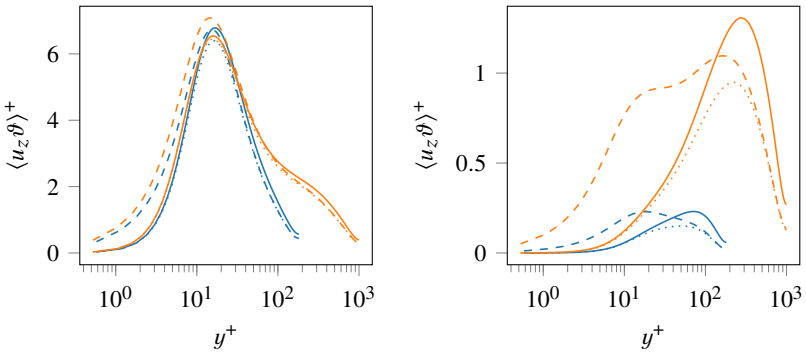

Figure 3.12: Variation of streamwise turbulent heat flux with TBC and Re_b for (left) $Pr = 0.71$ and (right) $Pr = 0.025$. Line styles and colors as in Table 3.3. Figures taken from Ref. [SSA2].

number contributions due to the radial turbulent heat flux for MBC and IF are very similar, as discussed previously.

In contrast to IF, MBC/IT suppress thermal fluctuations at the wall because of the imposed Dirichlet boundary condition. Therefore, the near-wall behavior of the turbulent heat fluxes for IF is different than for MBC/IT. As given by Kong, Choi, and Lee [42], a Taylor series expansion for the radial and streamwise turbulent heat fluxes yields

$$\langle \tilde{u}_r \vartheta \rangle = \begin{cases} c_3 \tilde{y}^3 + \ldots & \text{IT, MBC} \\ c_4 \tilde{y}^2 + \ldots & \text{IF} \end{cases} \tag{3.42}$$

$$\langle \tilde{u}_z \vartheta \rangle = \begin{cases} c_1 \tilde{y}^2 + \ldots & \text{IT, MBC} \\ c_2 \tilde{y} + \ldots & \text{IF} \end{cases} \tag{3.43}$$

The near-wall asymptotic behavior is hardly distinguishable for the radial turbulent heat flux (quadratic vs. cubic, Eq. (3.42)), while for the streamwise turbulent heat flux the differences are more pronounced (linear vs. quadratic, Eq. (3.43)).

The streamwise turbulent heat flux is shown in Fig. 3.12. and different behaviors in the near-wall region are observed according to Eq. (3.43) and

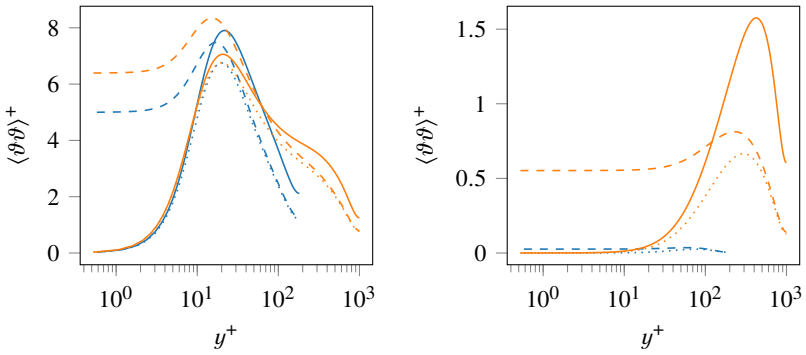

Figure 3.13: Variation of temperature variance with TBC and Re_b for (left) $Pr = 0.71$ and (right) $Pr = 0.025$. Line styles and colors as in Table 3.3. Figures taken from Ref. [SSA2].

as previously discussed for the radial counterpart. The maximum streamwise turbulent heat flux for $Pr = 0.71$ remains at $y^+ \approx 20$, independently of the Reynolds number, whereas for $Pr = 0.025$, the streamwise turbulent heat flux increases with Reynolds number and the (outer) maximum shifts towards the pipe center.

All previously presented thermal statistics are similar for MBC and IF, except for the streamwise turbulent heat fluxes for $Pr = 0.025$. While agreeing with MBC close to the pipe center, IF shows a local maximum at approximately $y^+ = 20$, corresponding to the location of maximum streamwise velocity fluctuations. For MBC and IT this maximum, most likely caused by the fluctuations of the streamwise velocity, is suppressed because of the imposed Dirichlet boundary condition for Θ and thus the temperature fluctuations at $y^+ = 20$ are much lower, as discussed in the next paragraph.

Differences in the near-wall behavior, arising from the TBC, will be further discussed for the temperature variance shown in Fig. 3.13. The temperature variance of MBC collapses with IT close to the wall and with IF in the center of the pipe, portraying precisely the mixed behavior of MBC. The temperature variation for IF at the wall is non-negligible and exhibits a constant region approximately up to $y^+ = 2$ for $Pr = 0.71$ and $y^+ = 30$ for $Pr = 0.025$. As for the turbulent heat fluxes, the inner-scaled temperature variance increases monotonically with increasing Reynolds number for $Pr = 0.025$. For $Pr =$

0.71, the temperature variance at the wall increases only slightly for IF with increasing Reynolds number. For MBC, the near wall behavior including the peak at $y^+ \approx 20$ appears to be independent of the Reynolds number. The same holds for IT when $Re_b \geq 11700$."[SSA2]

3.4.4 Spectral Analysis

"Streamwise power spectral densities (PSDs) of the thermal fluctuations, computed as the product of the Fourier coefficients of temperature fluctuation with their complex conjugate (i.e. $E = \hat{\vartheta}\hat{\vartheta}^*$) are evaluated for the different TBCs and Reynolds numbers. Contour lines of the premultiplied PSDs, i.e. $k_z \cdot E$, as a function of the wall-normal location and the streamwise wavelength $\lambda_z = 2\pi/k_z$, scaled with their respective maximum value, are shown in Fig. 3.14. For $Pr = 0.71$ the contour lines at 50% of the maximum include much smaller structures than for $Pr = 0.025$ because of the high thermal diffusivity at low Prandtl numbers. For $Pr = 0.025$ the inner-scaled streamwise wavelength of thermal structures increases at higher Reynolds numbers as observed by a shift of the contour lines and maximum values towards larger wavelengths. For instance, the maximum values for MBC reside at $(\lambda_z^+, y^+) = (560, 80)$, $(640, 140)$, $(1060, 220)$, $(1790, 420)$ for increasing Reynolds numbers. Note that as discussed previously in Section 3.2, the low Prandtl number case of IT at $Re_b = 5300$ is excluded. For $Pr = 0.71$ the effect of the Reynolds number on the location of the maximum and on the contour lines is less pronounced so that the maximum values for MBC reside at $(\lambda_z^+, y^+) = (640, 19)$, $(560, 19)$, $(490, 19)$, $(730, 17)$. One exception is the maximum value of IF at $Re_b = 5300$ that is found at a larger wavelength and closer to the wall.

While IT and MBC show very similar PSDs at their respective Reynolds numbers, IF is characterized by temperature fluctuations occurring at the wall. Hence, thermal scales of considerable streamwise wavelength are observed in the spectrum down to the wall, highlighting the difference between IF and the other two TBCs."[SSA2]

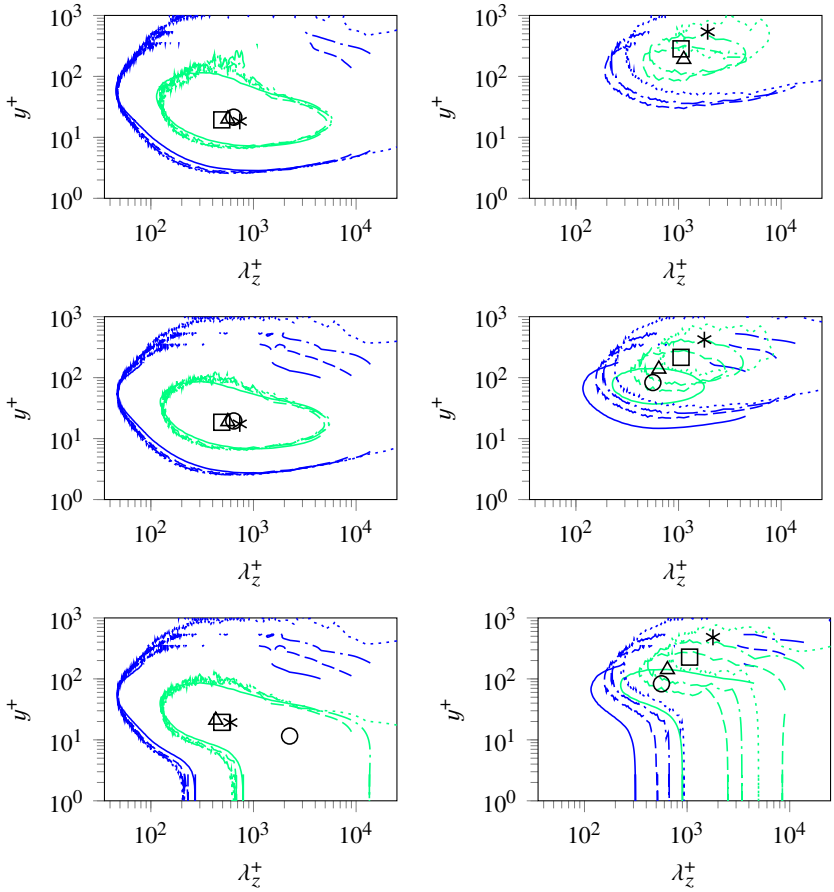

Figure 3.14: Streamwise premultiplied power spectral densities of thermal fluctuations at Re_b = 5300: ——, Re_b = 11700: - - -, Re_b = 19000: -·-·-, Re_b = 37700: ····· for (left panels) Pr = 0.71 and (right panels) Pr = 0.025. From top to bottom rows: IT, MBC, IF. Contour lines represent 50%: —— and 10%: —— of the maximum value, which is located at the markers Re_b = 5300: ○, Re_b = 11700: △, Re_b = 19000: □, Re_b = 37700: ∗. Line styles as in Table 3.3. Figures taken from Ref. [SSA2].

4 The effect of azimuthally inhomogeneous thermal boundary conditions

The second objective, as stated in Sec. 1.3, is to learn more about how the non-homogeneity of the thermal boundary condition affects the heat transfer within the receiver. To that end, azimuthally inhomogeneous thermal boundary conditions are set up and their thermal statistics are studied and compared to the homogeneous reference cases of the previous section. The results of this comparison are published by the present author and colleagues in Straub et al. [SSA1] and restated in this chapter. Note that all conclusions drawn from the results in this chapter are merged with the conclusions from the previous and next chapter and collectively given in Chapter 6.

"The influence of azimuthally inhomogeneous thermal boundary conditions on fluids with Prandtl numbers of $Pr = \nu/\alpha = 0.7, 4$ is shown by Antoranz et al. [4] for friction Reynols numbers of $Re_\tau = u_\tau R/\nu = 180, 360$. [...] The pipe radius is R and the friction velocity is $u_\tau = \sqrt{\tau_w/\rho}$ with τ_w being the wall-shear stress. Liquid metals are characterized by their large thermal conductivity, resulting in low molecular Prandtl numbers. Thus, conduction plays a more dominant role for liquid metals than for fluids of $Pr \approx 1$. How heat transfer in liquid metals is affected by inhomogeneous thermal boundary conditions and how it is different from fluids of $Pr \approx 1$ at moderately high Reynolds numbers has not yet been investigated.

Therefore, one objective of the present study is to fill this gap for azimuthally inhomogeneous applied heat flux by providing high fidelity datasets of low Prandtl number fluids at moderately high Reynolds numbers. Such a dataset is valuable for improving Reynolds–Averaged–Navier–Stokes (RANS) models to properly capture the behavior of low Prandtl number fluids subject to inhomogeneous thermal boundary conditions. Second objective, more directly related to the engineering problems in central receiver systems, is to pro-

vide information about the temperature statistics at the fluid – solid interface. Due to the inhomogeneous distribution of the temperature around the receiver tube, thermal stresses need to be considered during the design of the receiver [21, 22, 47, 52]. Hence, accurate results of the temperature distribution are necessary."[SSA1]

4.1 Setup of the azimuthally inhomogeneous thermal boundary conditions

The setup for studying the azimuthally inhomogeneous thermal boundary conditions is very similar to the one for homogeneous thermal boundary conditions described in Sec. 3.1. As a result of the assessment of different types of thermal boundary conditions in the previous chapter, the isoflux-type thermal boundary condition is selected in order to prescribe a constant (in time) wall heat flux, that is distributed non-homogeneously in azimuthal direction. Due to the inhomogeneity in azimuthal direction, statistical averaging, denoted by $\langle\cdot\rangle$, can only be performed temporally or spatially, in streamwise direction, which is indicated by a corresponding superscript. Note that "for brevity, when no superscript is given, averaging over time and streamwise direction is applied."[SSA1] When redefining the non-dimensional temperature to be

$$\Theta = \frac{T_b - T}{\langle q_w \rangle^{\varphi}} \rho c_p U_b \tag{4.1}$$

the advection-diffusion equation for temperature remains the same as in Eq. (3.2) with a source term of $S_\Theta = 4\tilde{U}_z$.

The assumptions made for the comparison of homogeneous thermal boundary conditions in the previous chapter are also made for investigating the azimuthally inhomogeneous thermal boundary conditions, i.e. incompressible flow, constant material properties, negligible effects due to viscous heating, temperature being treated as a passive scalar, so that buoyancy effects are not considered. Under the assumption of fully developed velocity and thermal fields, and due to the non-dimensionalization of the temperature as given in Eq. (4.1), periodic boundary conditions are admissible since the statistics of velocity and non-dimensionalized temperature are independent of the streamwise location. The linear increase of the physical temperature in streamwise

direction [8, 60] is "taken into account in the source term $4\tilde{U}_z$ [...] (cf. [62]). In other words, this source term compensates for the prescribed wall heat flux."[SSA1].

The thermal boundary condition is prescribed as an "azimuthally dependent wall heat flux of [4]

$$\tilde{q}_w(\varphi) = \begin{cases} 2, & 0 < \varphi < 180° \\ 0, & \text{else} \end{cases} \tag{4.2}$$

$$\tilde{q}_w(\varphi) = \begin{cases} \pi \sin(\varphi), & 0 < \varphi < 180° \\ 0, & \text{else} \end{cases} \tag{4.3}$$

Eq. (4.2) represents a constant wall heat flux on the upper part of the pipe and adiabatic on the lower part, subsequently referred to as "halfconst" and eq. (4.3) represents a sinusoidal wall heat flux on the upper part and adiabatic on the lower part and referred to as "halfsin". Factors 2 and π stem from considering the same heat rate as in the homogeneous case. Note that wall heat flux is non-dimensionalized as $\tilde{q}_w = q_w / \langle q_w \rangle^{\varphi}$. The boundary conditions together with the coordinate system are illustrated schematically in Fig. 4.1"[SSA1]

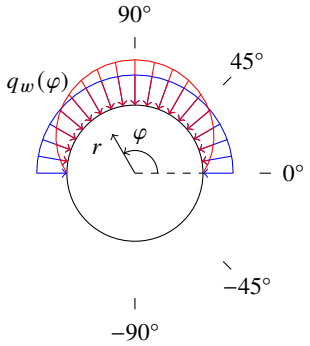

Figure 4.1: Schematic of the prescribed wall heat flux distribution. Figure taken from Ref. [SSA1].

The parameter space of Reynolds numbers and Prandtl numbers as well as the mesh is the same as in the comparison of different thermal boundary condition types, discussed in Sec. 3.1.

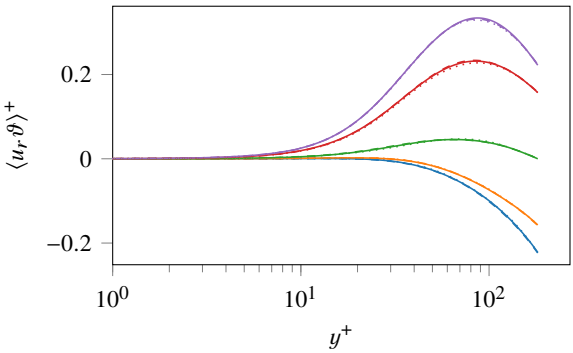

Figure 4.2: Radial turbulent heat flux in viscous units of "halfsin" for $Re_b = 5300$ and $Pr = 0.025$ evaluated at $\varphi = -90°$ ( ), $\varphi = -45°$ ( ), $\varphi = 0°$ ( ), $\varphi = 45°$ ( ), $\varphi = 90°$ ( ) with LES12.5 ( ), LES50 ( ) and DNS ( ). Figure taken from Ref. [SSA1].

The selected domain size and the mesh resolution for the LES "is validated by comparing the reference DNS results with $L_z = 12.5\,D$ to the slightly coarser resolved LESs with $L_z = 12.5\,D$ (LES12.5) and $L_z = 50\,D$ (LES50). Good agreement is found for the turbulent heat fluxes in radial and streamwise direction and the mean temperature. This is exemplified in Fig. 4.2, showing for the "halfsin" setup at $Re_b = 5300$ and $Pr = 0.025$ the radial turbulent heat flux $\langle u_r\vartheta\rangle^+$ evaluated at five azimuthal locations. The temperature variance $\langle\vartheta\vartheta\rangle^+$ for $Pr = 0.025$ is found to be more sensitive to the domain size, as also reported by Tiselj [75] for channel flows at low Prandtl numbers. At the location of maximum wall heat flux ($\varphi = 90°$) the temperature variance evaluated at the wall for $L_z = 12.5\,D$ is 7 % lower than for $L_z = 50\,D$. However, other statistics, like the mean temperature and the turbulent heat fluxes agree well for $L_z = 12.5\,D$ and $L_z = 50\,D$, so that"[SSA1] the following results refer to $L_z = 12.5\,D$.

4.2 Results and Discussion

The results are taken from the publication by Straub et al. [SSA1] and are repeated in the following subsections, presenting the local and global Nusselt

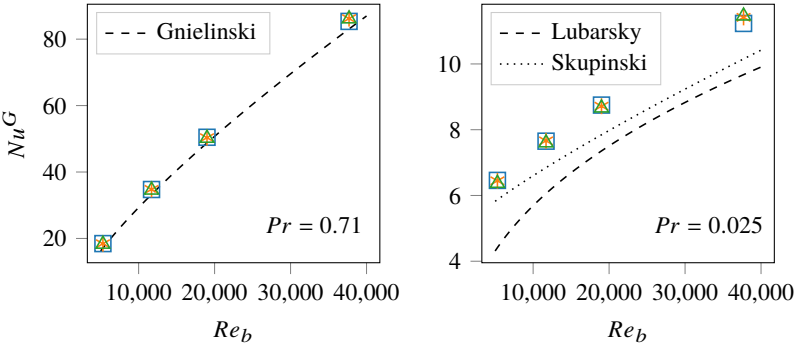

Figure 4.3: Global Nusselt number of homogeneous (□), "halfconst" (∗) and "halfsin" (△) compared with correlations[26, 48, 73]. Figures taken from Ref. [SSA1].

numbers, temperature and temperature variance as well as the turbulent Prandtl number.

4.2.1 Nusselt Number

"The heat transfer coefficient h, being non-dimensionalized in form of the Nusselt number [$Nu = hD/\lambda$], characterizes the convective heat transfer and is typically required for design of a heat exchanger device. For azimuthally inhomogeneous thermal boundary conditions a global and local Nusselt number are defined as

$$Nu^G = \frac{D}{\lambda}\frac{\langle q_w\rangle^\varphi}{\langle T_w - T_b\rangle^{\varphi,z,t}} = -\frac{Pe}{\langle\Theta_w\rangle^{\varphi,z,t}} \tag{4.4}$$

$$Nu(\varphi) = \frac{D}{\lambda}\frac{q_w(\varphi)}{\langle T_w - T_b\rangle^{z,t}} = -\frac{Pe}{\langle\Theta_w\rangle^{z,t}}\tilde{q}_w \tag{4.5}$$

with the Péclet number [$Pe = DU_b\rho c_p/\lambda$]. Note that the global Nusselt number $Nu^G \neq \langle Nu(\varphi)\rangle^\varphi$ since the wall heat flux in the numerator and the difference between wall temperature and bulk temperature in the denominator are averaged separately for Nu^G.

The global Nusselt number is shown in Fig. 4.3. For both Prandlt numbers, the

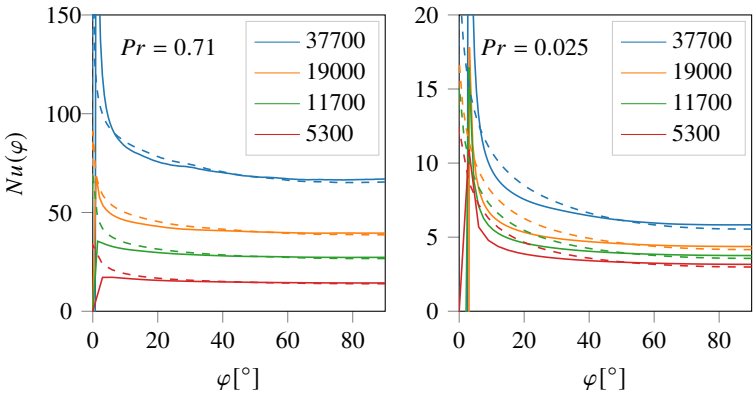

Figure 4.4: Local Nusselt number of "halfsin" (——) and "halfconst" (- - -) for various Re_b. Figures taken from Ref. [SSA1].

azimuthally inhomogeneous wall heat flux distributions yield the same global Nusselt number as in the homogeneous setup. Thus, the global Nusselt number appears to be independent of the distribution of the wall heat flux [50]. For $Pr = 0.71$, the global Nusselt numbers are well predicted by the Gnielinski correlation [26]. In the case of low Prandtl number fluids with $Pr = 0.025$, two correlations which perform best, based on the comparison by Pacio, Marocco, and Wetzel [57], are from Lubarsky and Kaufman [48] and Skupinski, Tortel, and Vautrey [73]. They both underestimate the global Nusselt number for the present range of Reynolds numbers.

As the global Nusselt number does not give any local information, the local Nusselt number, shown in Fig. 4.4, is more relevant for the azimuthally inhomogeneous setup. Note that due to symmetry only half of the heated section in the range $0 < \varphi < 90°$ is shown. The local Nusselt number peaks at $\varphi \approx 0$, i.e. at the boundary between adiabatic and heated wall. At the location, where the difference between bulk and wall temperature vanishes, i.e. the denominator in (4.5), a singularity in the local Nusselt number occurs. This happens for "halfsin" of $Pr = 0.025$ in the heated part of the wall, as recognizable from the zero crossing Fig. 4.7 and from the corresponding peak in the local Nusselt number in Fig. 4.4.

Table 4.1: Global Nusselt number and local Nusselt number for "halfsin" at the location of highest wall heat flux for $Pr = 0.71$ ($Pr = 0.025$) (taken from Ref. [SSA1]).

Re_b	Nu^G	$Nu(\varphi = 90°)$
5300	18 (6.4)	14 (3.2)
11700	35 (7.6)	27 (3.8)
19000	50 (8.7)	40 (4.4)
37700	86 (11)	67 (5.8)

Over a wide part of the heated section spanned symmetrically around $\varphi = 90°$, both distributions, "halfconst" and "halfsin", collapse and remain independent of φ. This plateau is observed in the range starting from $\varphi \approx 30°$ and $\varphi \approx 50°$ for $Pr = 0.71$ and $Pr = 0.025$, respectively. The local Nusselt numbers at the location of maximum wall heat flux $\varphi = 90°$ for "halfsin" together with the global Nusselt numbers are given in Table 4.1. The local Nusselt numbers at the highest wall heat flux are $\approx 20\,\%$ and $\approx 50\,\%$ lower than their respective global Nusselt numbers for $Pr = 0.71$ and $Pr = 0.025$."[SSA1]

4.2.2 Temperature

"Snapshots of the instantaneous temperature distribution for "halfsin" at both Prandtl numbers, $Pr = 0.71$ and $Pr = 0.025$, and the lowest and highest simulated Reynolds numbers, $Re_b = 5300$ and $Re_b = 37700$, are displayed in Fig. 4.5. Note that due to the definition of Θ in Eq. (4.1), low values of Θ correspond to high values of T. Evidently, the temperature field is smoother in the low Prandtl number fluid of $Pr = 0.025$, with the small scales being blurred and only the larger scales remaining. The increase in Reynolds number by a factor of ≈ 7 results in smaller scales and a thinner conductive sublayer for both Prandtl numbers, even if this is less pronounced for $Pr = 0.025$.

Averaging in time and streamwise direction yields the mean non-dimensional temperature distribution, presented in viscous units $\Theta^+ = \Theta u_\tau / U_b$ in Fig. 4.6. The conductive sublayer becomes thinner with increasing Reynolds number

resulting in higher radial temperature gradients inside of it. Differences between "halfconst" and "halfsin" are largest close to the heated wall, where for "halfsin" $\langle\Theta_w\rangle^+$ decreases monotonically from $\varphi = 0°$ to $\varphi = 90°$, shown by the darkest region in Fig. 4.6 , while for "halfconst", $\langle\Theta_w\rangle^+$ is almost constant over the heated section. These differences between "halfconst" and "halfsin" are more evident for $Pr = 0.71$ than for $Pr = 0.025$ because of the higher conductive heat transfer in the latter.

The non-dimensional wall temperature is shown in Fig. 4.7. For $Pr = 0.025$, $\langle\Theta_w\rangle^+$ vanishes for "halfsin" at $\varphi > 0°$ and for "halfconst" at $\varphi < 0°$ explaining the sharp peaks observed in the local Nusselt number in Fig. 4.4. Within the heated region of "halfsin" $\langle\Theta_w\rangle^+$ varies sinusoidally as the wall heat flux resulting thus in a region of constant $Nu(\varphi)$ (eq. (4.5)), as shown in Fig. 4.4.

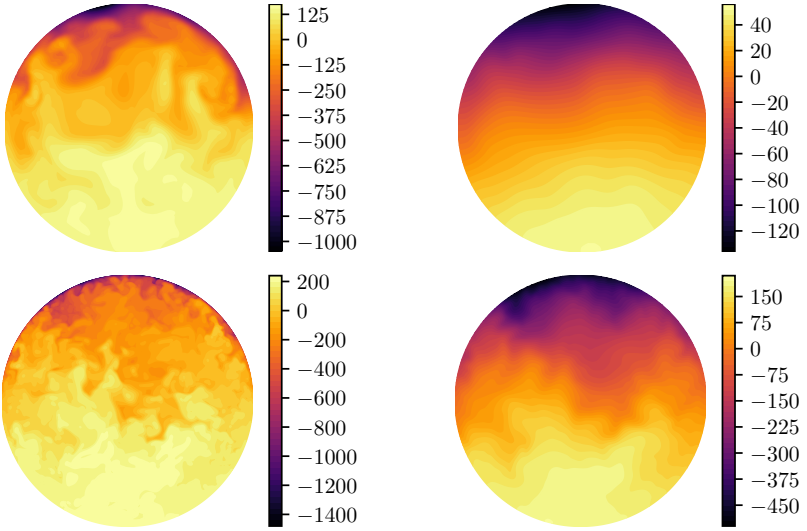

Figure 4.5: Snapshots of the non-dimensionalized temperature field Θ of "halfsin" at $Re_b = 5300$ (top row) and at $Re_b = 37700$ (bottom row) with $Pr = 0.71$ (left) and $Pr = 0.025$ (right). Values range from low (dark region) in the upper, heated part of the pipe ($\varphi = 90°$) to high (bright region) in the lower, adiabatic part $\varphi = -90°$. Figures taken from Ref. [SSA1].

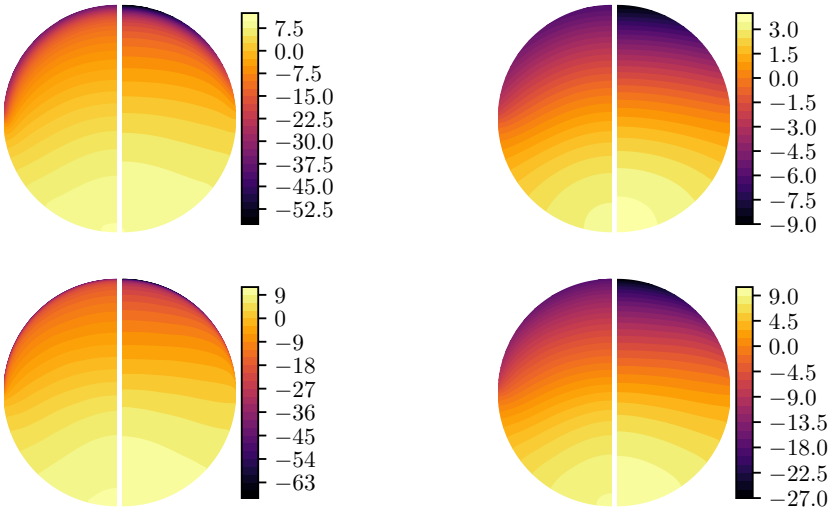

Figure 4.6: Non-dimensionalized temperature in viscous units at $Re_b = 5300$ (top row) and $Re_b = 37700$ (bottom row) with $Pr = 0.71$ (left) and $Pr = 0.025$ (right). The left semicircles show "halfconst" and the right semicircles show "halfsin". Figures taken from Ref. [SSA1].

A quantitative comparison of the temperature profiles for the "halfsin" thermal boundary condition is shown in Fig. 4.8. The various lines show radial profiles of $\langle\Theta\rangle^+$ evaluated at five azimuthal locations $\varphi = -90°, -45°, 0°, 45°, 90°$. For $Pr = 0.71$ the change in Reynolds number from $Re_b = 5300$ ($Re_\tau = u_\tau R/\nu \approx 180$) to $Re_b = 37700$ ($Re_\tau \approx 1000$) has a moderate impact only, whereas for $Pr = 0.025$ the temperature values approximately triple. For instance, $\langle\Theta_w\rangle^+(\varphi = 90°) = -9$ for $Re_b = 5300$ and $\langle\Theta_w\rangle^+(\varphi = 90°) = -27$ for $Re_b = 37700$. A logarithmic region for the temperature profiles is only observed for $\varphi > 0$ at $Pr = 0.71$. Indeed, for $Pr = 0.025$ convection increases over conduction with increasing Reynolds number, while for $Pr = 0.71$ convection is already predominant at $Re_b = 5300$. In the adiabatic region and at $Pr = 0.025$, the thermal field is dominated by conduction."[SSA1]

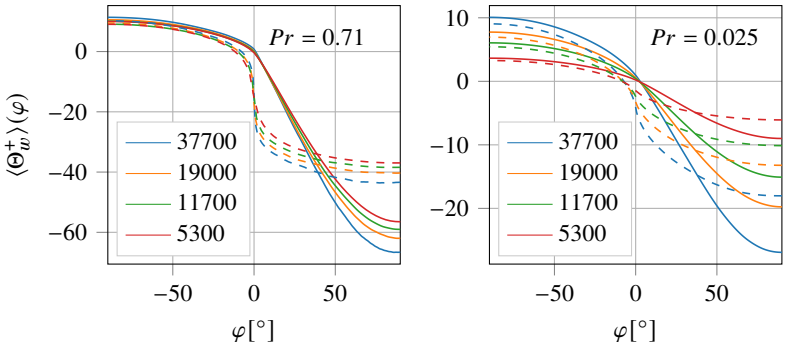

Figure 4.7: Non-dimensional wall temperature in viscous units of "halfsin" (——) and "halfconst" (- - -) for various Re_b. Figures taken from Ref. [SSA1].

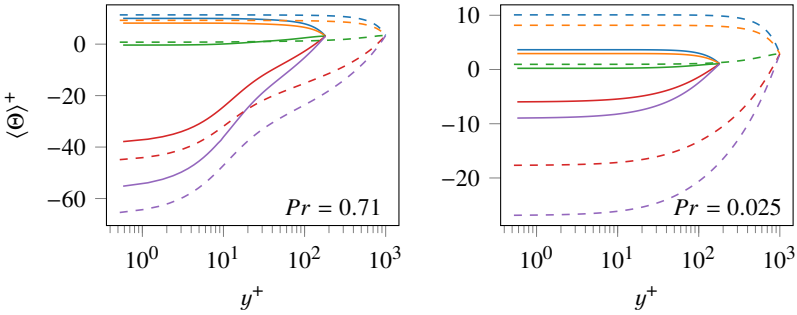

Figure 4.8: Non-dimensional temperature profiles of "halfsin" in viscous units evaluated at φ = −90° (——), φ = −45° (——), φ = 0° (——), φ = 45° (——), φ = 90° (——) for Re_b = 5300 (——) and Re_b = 37700 (- - -). Figures taken from Ref. [SSA1].

4.2.3 Temperature Variance

"The general distribution as well as the influence of the Prandtl and the Reynolds number on the temperature variance is shown for the "halfsin" setup in Fig. 4.9. On the adiabatic (lower) part of the pipe the temperature variance is very small. For Pr = 0.71 the highest temperature variance occurs at the azimuthal location of maximum wall heat flux (φ = 90°) with a peak at the wall normal location of $y^+ \approx 20$. A higher Reynolds number gives a slightly

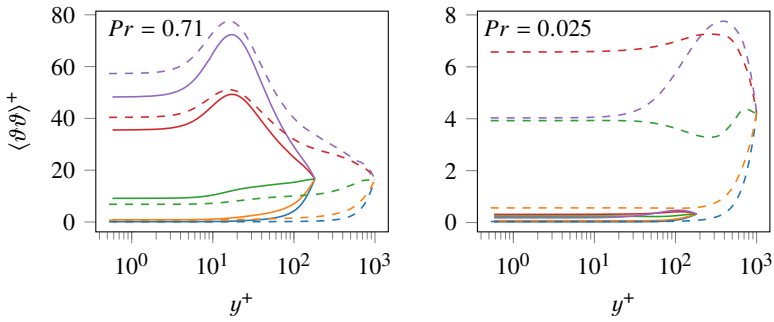

Figure 4.9: Non-dimensional temperature variance profiles of "halfsin" in viscous units evaluated at $\varphi = -90°$ (———), $\varphi = -45°$ (———), $\varphi = 0°$ (———), $\varphi = 45°$ (———), $\varphi = 90°$ (———) for $Re_b = 5300$ (———) and $Re_b = 37700$ (- - -). Figures taken from Ref. [SSA1].

increased temperature variance in the heated (upper) part of the pipe. For $Pr = 0.025$ on the other hand, the Reynolds number has a strong effect on the magnitude of the temperature variance. The highest temperature variance at the wall occurs at $\varphi = 45°$, instead of $\varphi = 90°$, with a peak at the wall normal location of $y^+ \approx 100$ and $y^+ \approx 400$ for $Re_b = 5300$ and $Re_b = 37700$, respectively. The wall normal temperature variance at $\varphi = 45°$ increases by a factor of 18 from $Re_b = 5300$ to $Re_b = 37700$. This is caused by the very high contribution of conduction to the heat transfer at $Re_b = 5300$ for $Pr = 0.025$ and consequently almost no turbulent mixing. The turbulent mixing increases significantly at $Re_b = 37700$. For $Pr = 0.71$ however, convection already prevails over conduction at $Re_b = 5300$ and thus the increase of temperature variance with Reynolds number is less than compared to the case of $Pr = 0.025$. The peculiarity of the temperature variance in the near-wall region being higher at $\varphi = 45°$ than at $\varphi = 90°$ for $Pr = 0.025$ is also observed for "halfconst" and results from the higher production of temperature variance at the former azimuthal location. Due to the high thermal diffusivity, the radial gradients of the averaged temperature are small in the near-wall region at $\varphi = 90°$, as observed in Fig. 4.6 and discussed previously. Due to symmetry the azimuthal gradients vanish at $\varphi = 90°$. Therefore, the production of the temperature variance, i.e. the product of turbulent heat flux and averaged temperature gradient, is relatively small. However, strong gradients in azimuthal direction of the averaged temperature occur at $\varphi = 45°$ for $Pr = 0.025$, as observed in Fig. 4.6,

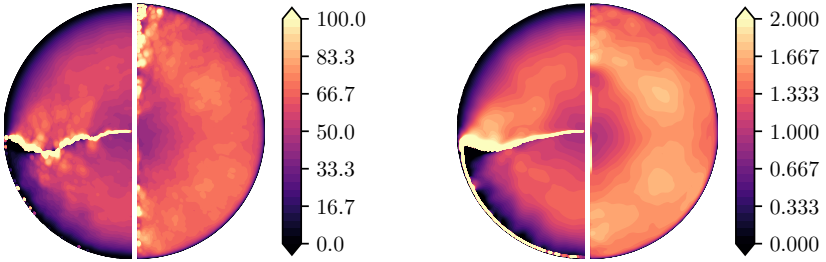

Figure 4.10: Ratio of turbulent thermal diffusivities to molecular thermal diffusivity α_t/α of "halfsin" at $Re_b = 37700$ for $Pr = 0.71$ (left) and $Pr = 0.025$ (right). The left side of each plot shows $\alpha_{t,r}$ and the right side $\alpha_{t,\varphi}$. Figures taken from Ref. [SSA1].

and coincide with the maximum of the azimuthal turbulent heat flux, resulting in a higher production of the temperature variance than at $\varphi = 90°$."[SSA1]

4.2.4 Turbulent Prandtl Number

"RANS models relying on the Reynolds analogy, i.e. assuming that turbulent kinematic viscosity is approximately equal to turbulent thermal diffusivity $\nu_t/\alpha_t = Pr_t \approx 1$ are not suited for liquid metals due to their different heat transfer mechanism compared to fluids with $Pr \approx 1$ (e.g. Refs. [27, 38, 77]). The turbulent viscosity for the fully developed pipe flow is

$$\nu_t(r) = -\frac{\langle u_r u_z \rangle^{\varphi,z,t}}{\frac{\partial \langle U_z \rangle^{\varphi,z,t}}{\partial r}} \tag{4.6}$$

and the turbulent diffusivities, being different in radial and azimuthal direction, are

$$\alpha_{t,r}(r,\varphi) = -\frac{\langle u_r \vartheta \rangle}{\frac{\partial \langle \Theta \rangle}{\partial r}}, \quad \alpha_{t,\varphi}(r,\varphi) = -\frac{\langle u_\varphi \vartheta \rangle}{\frac{1}{r}\frac{\partial \langle \Theta \rangle}{\partial \varphi}} \tag{4.7}$$

The ratio of turbulent to molecular thermal diffusivity α_t/α for "halfsin" at $Re_b = 37700$ is shown in Fig. 4.10. The results for "halfconst" are similar and therefore omitted. As already found by Antoranz et al. [4] for $Re_b = 5300$

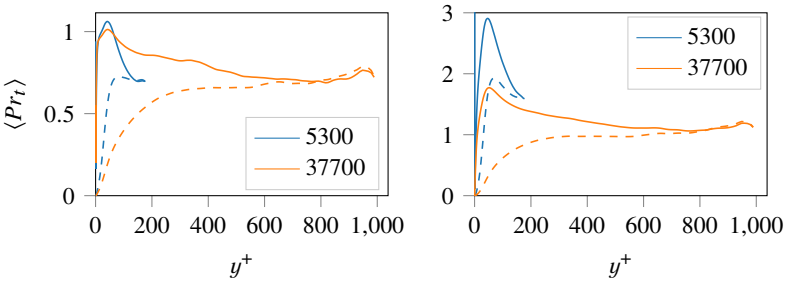

Figure 4.11: Turbulent Prandtl number for "halfsin" in radial (——) and azimuthal (- - -) direction for $Pr = 0.71$ (top) and $Pr = 0.025$ (bottom). Figures taken from Ref. [SSA1].

and $Pr = 0.71$, the thermal diffusivites of eqn. (4.7) are indeed different and clearly exhibit a dependency on the radial location but depend only weakly on the azimuthal location. The same is true for higher Reynolds numbers and also for the lower Prandtl number $Pr = 0.025$. A singularity appears where the temperature gradient in the denominator of eqs. (4.7) vanishes. Even though the general pattern for $Pr = 0.025$ is very similar to $Pr = 0.71$, the values are two orders of magnitude apart. For $Pr = 0.025$ the turbulent thermal diffusivities are comparable with the values of the molecular diffusivities and thus non-negligible, while for $Pr = 0.71$ the turbulent thermal diffusivities are dominant.

The radial and circumferential turbulent Prandtl numbers, shown in Fig. 4.11 for "halfsin", are obtained by dividing the turbulent viscosity, evaluated by eq. (4.6), with the values of $\alpha_{t,r}$ and $\alpha_{t,\varphi}$ averaged over a range without singularity and with a weak dependency on φ, i.e. $45° < \varphi < 90°$ and $0 < \varphi < 45°$, respectively. The results for "halfconst" are similar again and therefore omitted. For $Pr = 0.71$ and at $Re_b = 5300$, the turbulent Prandtl number attains a maximum value of $Pr_{t,r} \approx 1$ and $Pr_{t,\varphi} \approx 0.7$ in radial and azimuthal direction, respectively, and only in the center of the pipe it shows an isotropic behavior, i.e. $Pr_{t,r} = Pr_{t,\varphi} = 0.7$. At $Re_b = 37700$, the radial turbulent Prandtl number still has a peak close to the wall at $y^+ \approx 50$ but converges to the azimuthal turbulent Prandtl number further away from the wall. An isotropic state is observed from $y^+ \approx 500$ up to the center of the pipe where $Pr_{t,r} \approx Pr_{t,\varphi} \approx 0.7$. For the low molecular Prandtl number of $Pr = 0.025$

the turbulent Prandtl numbers exhibit similar wall-normal dependencies with maxima of $Pr_{t,r} \approx 3$ and $Pr_{t,\varphi} \approx 2$ at $Re_b = 5300$ and an isotropic state of $Pr_{t,r} \approx Pr_{t,\varphi} \approx 1$.

Therefore, if the Reynolds number is high enough, the assumption of a constant turbulent Prandtl number close to 1 appears to be adequate within the core region of the flow even for fluids of low molecular Prandtl number and non-homogeneous thermal boundary conditions. Close to the wall however such an assumption underestimates the turbulent Prandtl number of $Pr = 0.025$ in radial direction up to 75 %. Overall, the present results indicate that errors introduced by the assumption of the Reynolds analogy are becoming less severe for higher Reynolds numbers."[SSA1]

4.2.5 Proper orthogonal decomposition

The application and evaluation of the POD is carried out analogous to Antoranz et al. [5] for the "halfsin" setup. The present results at $Re_b = 5300$ and $Pr = 0.71$ agree with their data. Low-Prandtl-number fluids and the moderately high Reynolds numbers of the present database extend their observations and are reported in the following paragraphs.

By decomposing the thermal field into POD modes, a large amount of the energy can be represented by a small number of modes thereby reducing the order of the model. Summing all the eigenvalues together yields the energy, in case of thermal fields that is half the temperature variance, contained in the domain according to Eq. (2.59).

The energy captured by a single mode is given by its eigenvalue $\lambda_i = \sigma_i^2/M$ (where the factor $1/M$ is dropped in Figure 4.12 due to the normalization by the energy contained within all modes). This energy per POD mode is visualized together with the cumulative sum in Fig. 4.12. For $Pr = 0.71$, the modal contribution of the first modes to the energy is relatively low with values of $\sigma_i^2 \approx 6\%-7\%$. In order to represent 90% of the energy a large number of modes is required, i.e $105, 239, 370, 374$ for $Reb = 5300, 11700, 19000, 37700$, respectively. As smaller structures of non-negligible energy are present at higher Reynolds numbers, more modes are required for $Re_b = 37700$ compared to $Re_b = 5300$ to represent a certain amount of energy.

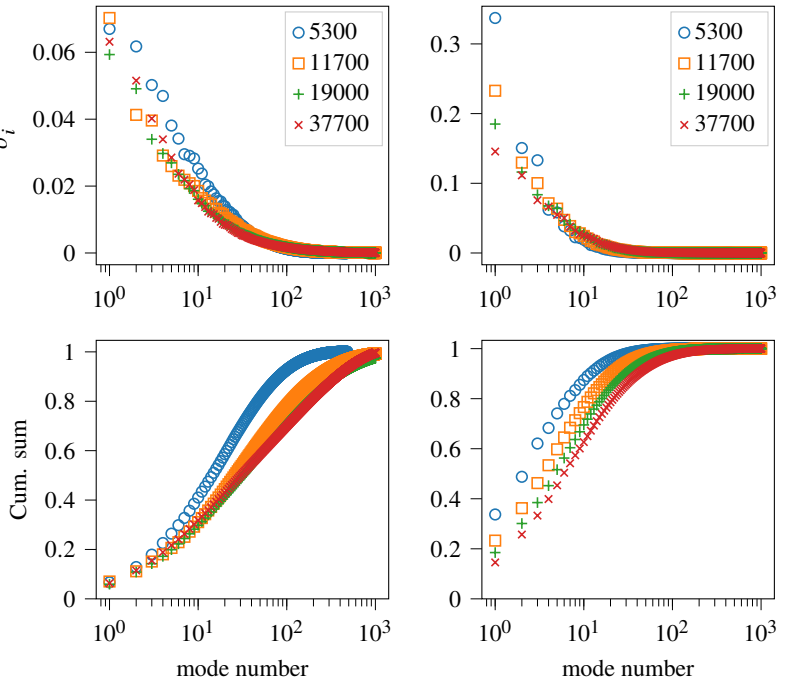

Figure 4.12: Singular values σ_i^2, normalized by their sum, for each mode (top row) and cumulative sum (bottom row) for $Pr = 0.71$ (left column) and $Pr = 0.025$ (right column)

A reduced order model of low-Prandtl-number fluids is more likely conceivable since a larger fraction of the energy is contained within the first modes. In fact, the first mode for $Pr = 0.025$ at $Re_b = 5300, 11700, 19000, 37700$ is responsible for 34%, 23%, 18% and 15%, respectively and 90% of the energy are contained within the first $12, 21, 28, 40$ modes. Due to the high thermal diffusivity of low-Prandtl-number fluids, the thermal structures, particularly the energy-containing ones, are larger than compared to $Pr = 0.71$ so that the relative importance of the first modes increases.

The dominant coherent structure, identified by the first POD mode, is presented in Fig. 4.13 in a cross-sectional view of the heated pipe. Note that the POD modes, identified as eigenvectors in the discrete case as explained in Section

2.3, are normalized to be of unit length. Additionally, symmetry is exploited to improve the quality of the first POD mode. In the case of $Pr = 0.71$ a large scale structure is located at the symmetry plane of $\varphi = 90°$. The zero contour line separates this central structure from two flanking structures on each side. Even though, the central and flanking structures extend from the heated, upper part of the pipe to the lower part, high magnitudes are only observed in the upper part. The Reynolds number only has a small influence on the shape of the structures. For $Re_b = 5300, 11700$ and $Pr = 0.71$ the first modes agree well with the data by Antoranz et al. [5]. The low-Prandt-number fluid of $Pr = 0.025$ exhibits a similar pattern of structures with a central one on the symmetry plane and two flanking structures. Particularly, for the moderately high Reynolds number of $Re_b = 37700$, the location of the structures and their magnitude agree very well between $Pr = 0.71$ and $Pr = 0.025$. At the lower end of the investigated Reynolds numbers, $Re_b = 5300$, only the central structure remains and extends over the whole cross section. Especially for this combination of $Re_b = 5300$ and $Pr = 0.025$, where the thermal field is still in a laminar-like state, the turbulent contribution to the heat transfer from the heated, upper part of the pipe to the lower part is largely represented by this first mode.

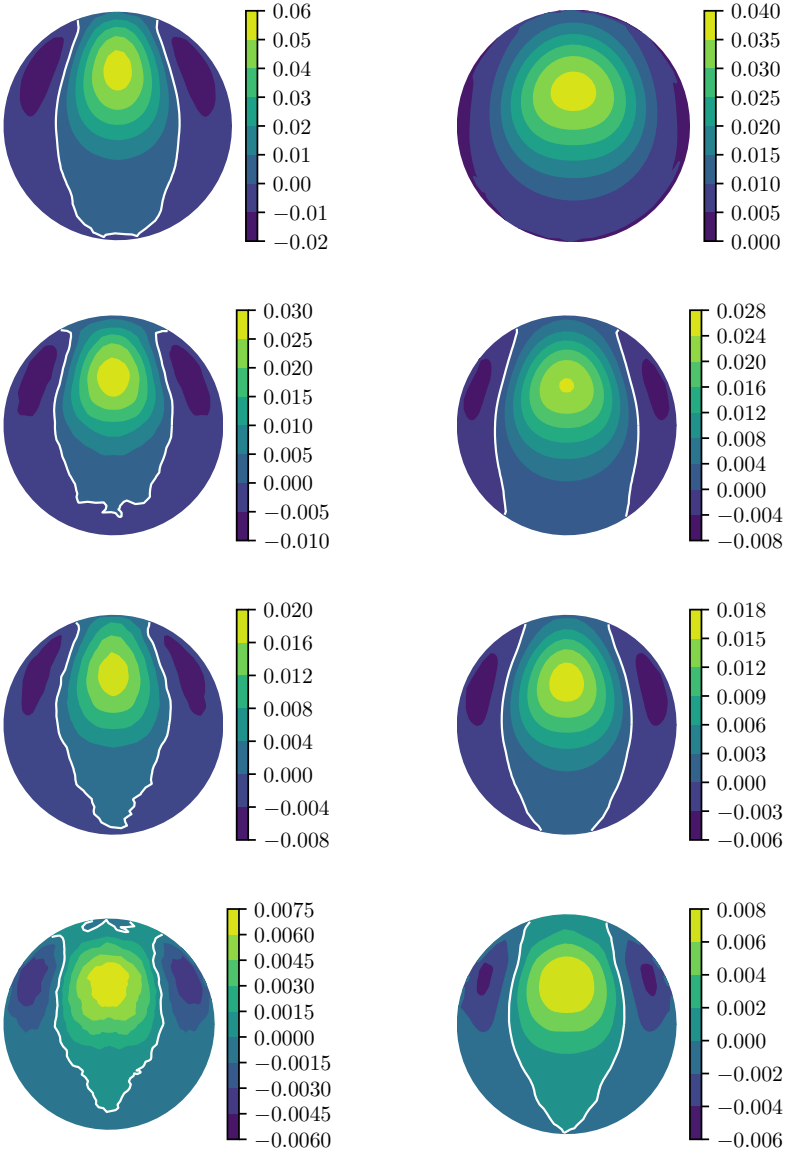

Figure 4.13: First POD modes of $Pr = 0.71$ (left column) and $Pr = 0.025$ (right column) at $Re_b = 5300, 11700, 19000, 37700$ (from top to bottom).

5 The effect of axially and azimuthally inhomogeneous thermal boundary conditions

The wall heat flux distribution on a receiver of a central receiver system is inhomogeneous both in azimuthal and in axial direction. Therefore, thermal statistics are strongly dependent on the location in respect to the wall heat flux distribution and need to be evaluated locally.

The numerical setup of this complex distribution of wall heat flux applied on the receiver is described in the next section followed by the results in terms of first- and second-order thermal statistics. The conclusions are drawn in the final chapter.

5.1 Setup of the axially and azimuthally inhomogeneous thermal boundary conditions

The assumptions made in the previous chapters, i.e. incompressible flow, Newtonian fluid, constant thermophysical properties, negligible heating due to viscous dissipation and negligible buoyancy forces, are adopted. The velocity field is considered to be fully developed. However, the thermal field is developing due to the axial inhomogeneity in contrast to the previous chapters. Therefore, the governing equations, Eq. (3.1) and Eq. (3.2), are slightly modified by dropping the source term S_Θ in the temperature equation. This source term compensates for the increase in temperature along the axial direction and allows for treating the fully developed temperature field with periodic boundary conditions. For a developing temperature field such a source term is not required as Dirichlet and Neumann boundary conditions are prescribed

at the inlet and outlet, respectively, for the temperature field. Note that periodic boundary conditions are prescribed for the fully developed velocity field nonetheless because of the treatment of the temperature as a passive scalar.

Different from the previous chapters, temperature is non-dimensionalized as a scaled difference between the local temperature T and, as reference, the inlet temperature T_0

$$\Theta = \frac{T - T_0}{q_{w,ref}} \rho c_p U_b \tag{5.1}$$

with a reference wall heat flux $q_{w,ref} = \pi q_{w,max}$. The Dirichlet boundary condition at the inlet and zero-gradient at the outlet are then given as

$$\Theta(z = 0) = 0 \tag{5.2}$$

$$\left.\frac{\partial \Theta}{\partial z}\right|_{L_z} = 0 \tag{5.3}$$

The prescribed wall heat flux at the outlet is non-zero and hence the temperature is increasing in axial direction so that the zero-gradient boundary condition is enforced artificially. However, the prescribed wall heat flux at the outlet is small, i.e. less than 5% of its maximum, so that the axial temperature gradient at the outlet is small, too, and the zero-gradient boundary condition is a reasonable approximation.

At the wall, the no-slip boundary condition for the velocity field is set and a wall heat flux distribution, similar to the one employed by Marocco et al. [50], of

$$\tilde{q}_w = \frac{q_w}{q_{w,ref}} = \begin{cases} \pi \sin(\varphi) \exp\left(-\frac{1}{2}\left(\frac{z - L_z/2}{L_z/5}\right)^2\right), & 0 < \varphi < 180° \\ 0, & \text{else} \end{cases} \tag{5.4}$$

is prescribed. It is adiabatic on one side of the pipe and varies sinusoidally over the circumferential direction and as a Gaussian function in axial direction, being centered symmetrically over the domain of length L_z. The azimuthal variation and the factor π is the same as in the previous chapter, cf. Eq. (4.3), so that the heat rate at $z = L_z/2$ is the same as in the homogeneous setup.

Table 5.1: Domain length L_z, number of elements nel and averging time t_A.

Re_b	L_z/D	nel	$t_A U_b/D$
5300 (DNS)	12.5	36 480	11 900
5300 (DNS)	25.0	72 960	17 600
5300 (LES)	12.5	7128	48 000
11 700 (LES)	12.5	45 360	9000
19 000 (LES)	12.5	132 480	5000
37 700 (LES)	12.5	631 040	660

Using the definition of the non-dimensional temperature Θ, the local Nusselt number is given as

$$Nu(\varphi, z) = \frac{Pe}{\langle \Theta_w(\varphi, z) \rangle^t - \langle \Theta_b(z) \rangle^t} \tilde{q}_w(\varphi, z) \tag{5.5}$$

The circumferentially averaged Nusselt number and the Nusselt number at the circumferential location of maximum wall heat flux $\varphi = 90°$ are respectively

$$\langle Nu \rangle^\varphi = \frac{Pe}{\langle \Theta_w \rangle^{\varphi,t} - \langle \Theta_b \rangle^t} \langle \tilde{q}_w \rangle^\varphi \tag{5.6}$$

$$Nu(\varphi = 90°) = \frac{Pe}{\langle \Theta_w(\varphi = 90°) \rangle^t - \langle \Theta_b \rangle^t} \tilde{q}_w(\varphi = 90°) \tag{5.7}$$

Two direct numerical simulations at $Re_b = 5300$ follow the resolution requirements given in Sec. 3.1 and differ in domain length, i.e. $L_z = 12.5\,D$ and $L_z = 25\,D$. Large-eddy simulations are performed for $Re_b = 5300, 11700, 19000, 37700$ with the same resolution requirements as given for the LES in Sec. 3.1 and a domain length of $L_z = 12.5\,D$. All simulations feature two Prandtl numbers of $Pr = 0.025, 0.71$. Their respective number of elements and averaging times are given in Table 5.1.

Due to the inhomogeneity of the thermal boundary conditions and consequently the lack of homogeneous directions, averaging is performed only in time except

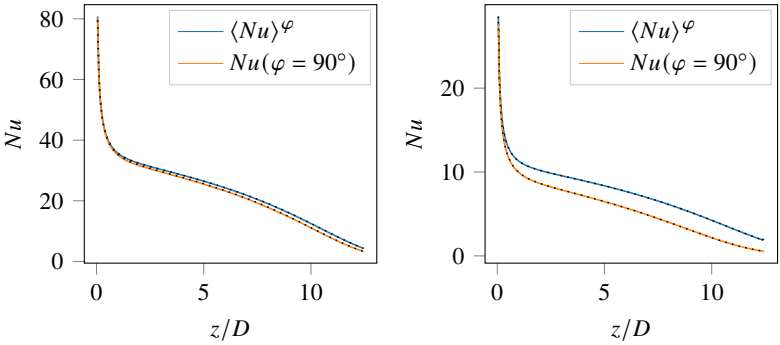

Figure 5.1: Circumferentially averaged Nusselt number and Nusselt number at $\varphi = 90°$ for $Re_b = 5300$ at $Pr = 0.71$ (left) and $Pr = 0.025$ (right). Continuous lines are DNS and dotted lines are LES results.

for the circumferentially averaged Nusselt number where both spatial and temporal averaging is performed. Thus, first- and second-order statistics, presented in the next section, are dependent on radial r, azimuthal φ and streamwise z location. The statistics are improved by exploiting the left-right-symmetry along the axis at $\varphi = 90°$.

5.1.1 Validation

For validation purposes, the results of the LES at $Re_b = 5300$ and $L_z = 12.5$ are compared to the DNS in this subsection focusing on the agreement between DNS and LES results with a more detailed discussion of the results in the next section. The circumferentially averaged Nusselt number and the Nusselt number at the circumferential location of maximum wall heat flux are shown in Fig. 5.1. The Nusselt numbers from the LES are indistinguishable from the DNS results for both Prandtl numbers.

Second-order thermal statistics are more challenging in terms of required resolution and averaging time. Nevertheless, good agreement is found also for first- and second-order thermal statistics as exemplified by the radial turbulent heat flux presented in Fig. 5.2. The turbulent heat flux in radial direction is evaluated at different axial locations z/D and at the circumferential location

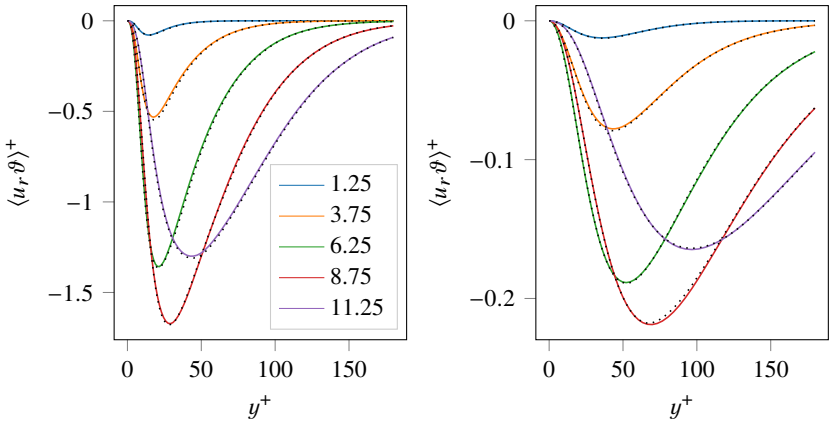

Figure 5.2: Radial turbulent heat flux at $\varphi = 90°$ for $Re_b = 5300$ at $Pr = 0.71$ (left) and $Pr = 0.025$ (right). The axial location is given in z/D. Continuous lines are DNS and dotted lines are LES results.

of maximum wall heat flux $\varphi = 90°$. The agreement between DNS and LES results for the radial turbulent heat flux is very good for both Prandtl numbers. Furthermore, temperature, temperature variance and turbulent heat fluxes in azimuthal and streamwise direction also agree well between DNS and LES results (not shown).

5.2 Results and Discussion

First- and second-order thermal statistics are evaluated in this section including temperature, temperature variance and turbulent heat fluxes in radial, azimuthal and streamwise direction together with the Nusselt number and instantaneous snapshots.

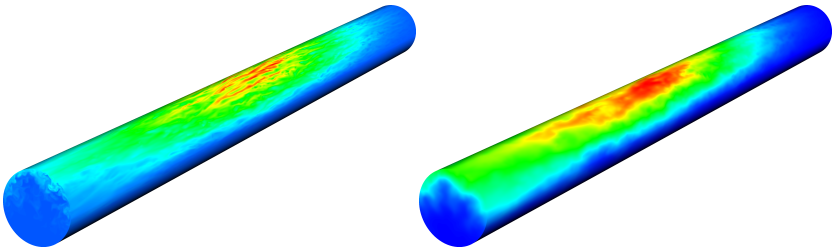

Figure 5.3: Instantaneous snapshots of the thermal field for $Re_b = 19000$ and $Pr = 0.71$ (left) and $Pr = 0.025$ (right), scaled by their individual minimum and maximum temperature. The flow direction is from the upper right to the lower left corner.

5.2.1 Instantaneous snapshots

The instantaneous temperature field for the axially and azimuthally inhomogeneous thermal boundary condition qualitatively shows the difference in the thermal field between the two investigated Prandtl numbers in Fig. 5.3 for $Re_b = 19000$. At the same instance in time the thermal field of a fluid with $Pr = 0.71$ and a low-Prandtl-number fluid of $Pr = 0.025$ are captured. The footprint of the prescribed wall heat flux boundary condition with the maximum temperature at $\varphi = 90°$ and at $z \approx L_z/2$ is clearly visible in both cases. A streaky pattern of the wall temperature at its maximum is visible only for $Pr = 0.71$ as well as comparably small structures at the cross section of the outlet. On the other hand, the low-Prandtl-number fluid is characterized by a high thermal diffusivity, which effectively smears out the smaller structures so that only the larger structures remain (c.f. Figs. 3.8 and 4.5 for the homogeneous and azimuthally inhomogeneous setups, respectively).

5.2.2 Nusselt number

More quantitative information can be gathered from the thermal statistics. The Nusselt number, which characterizes the heat transfer in forced convection, is presented in Fig. 5.4. The circumferentially averaged Nusselt number $\langle Nu \rangle^{\varphi}$ as well as the local Nusselt number evaluated at the location of maximum wall heat flux $\varphi = 90°$ are plotted. Their distribution is remarkably similar for $Pr = 0.71$. Due to the vanishing denominator, the Nusselt number becomes

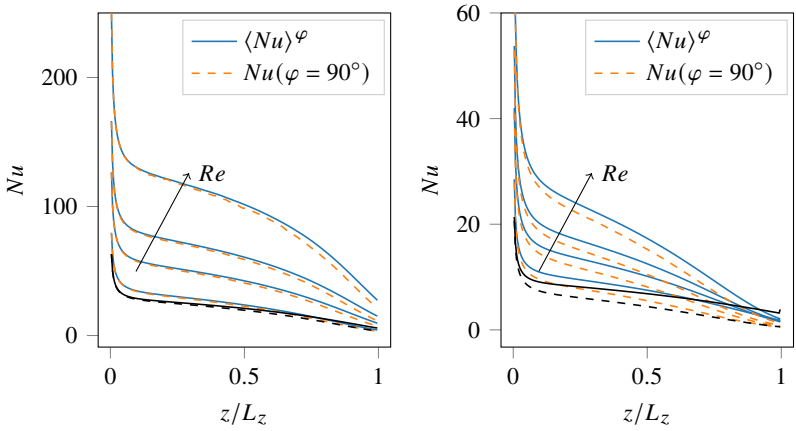

Figure 5.4: Nusselt number distribution for varying Reynolds numbers Re_b = 5300, 11700, 19000, 37700 at Pr = 0.71 (left) and Pr = 0.025 (right). The longer domain length of $L_z = 25\,D$ is given in black.

singular at the inlet and it decreases monotonically in axial direction. In the first half of the domain, wall temperature, bulk temperature and wall heat flux all increase in axial direction, with the difference between wall and bulk temperature (denominator of the Nusselt number) increasing stronger than the wall heat flux (numerator of the Nusselt number). In the second half of the domain, downstream of the maximum wall temperature, the difference between wall and bulk temperature decreases slower in axial direction than the wall heat flux decreases, resulting still in a decrease of the Nusselt number in axial direction. The same shape for the development of the Nusselt number has been reported by Marocco et al. [50] using a four-equation turbulence model. For low-Prandtl-number fluids the Nusselt number evaluated at the location of maximum heat flux $Nu(\varphi = 90°)$ is lower than the circumferentially averaged Nusselt number, a result of the less intense peak of the wall temperature due to the high thermal diffusivity, as shown and discussed in the next paragraphs. Higher Reynolds numbers lead to higher Nusselt numbers as expected since convection becomes more dominant.

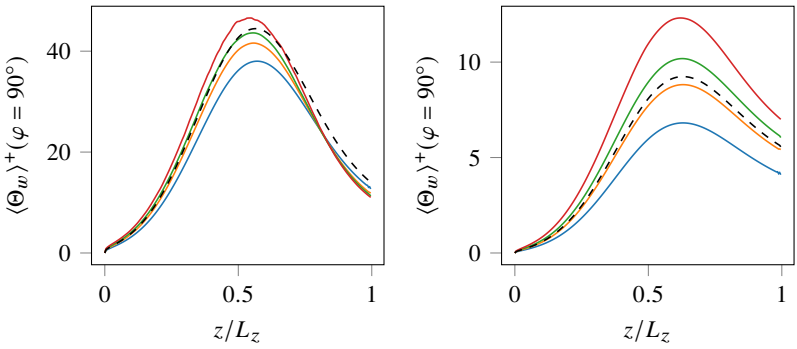

Figure 5.5: Wall temperature in viscous units at $\varphi = 90°$ for $Pr = 0.71$ (left) and $Pr = 0.025$ (right). Line-styles and -colors refer to $Re_b = 5300$, $L_z = 25$: (- - -), $Re_b = 5300$, $L_z = 12.5$: (———), $Re_b = 11700$: (———), $Re_b = 19000$: (———), $Re_b = 37700$: (———)

5.2.3 Wall temperature

The wall temperature evaluated at the circumferential location of maximum wall heat flux $\varphi = 90°$ is shown in Fig. 5.5. The maximum of the wall temperature resides at $z/L_z \approx 0.6$, shifted slightly downstream in respect to the maximum of the wall heat flux at $z/L_z = 0.5$, and its location is insensitive to the Reynolds number. The effect of the Reynolds number is more pronounced for low Prandtl numbers, causing higher maximum temperatures for higher Reynolds numbers. Lower Nusselt numbers for the longer domain length of $L_z = 25\,D$, as shown in Fig. 5.4, are associated with a higher wall temperature for both Prandtl numbers than the corresponding case at the same Reynolds number and the shorter domain. As the thermal field is developing, the domain length has an effect on the thermal statistics. For instance the temperature field at the axial center of the domain, $z/L_z = 0.5$, develops from the inlet for $z/D = 12.5$ in the longer domain compared to $z/D = 6.25$ in the shorter domain. Besides, the overall heat input, as a result of the prescribed wall heat flux according to Eq. 5.2, is larger for the longer domain.

Fig. 5.6 shows the wall temperature distribution in circumferential direction evaluated at $z = L_z/2$. Due to the left-right symmetry of the problem only one half of the pipe $-90° < \varphi < 90°$ is presented. Angles are depicted

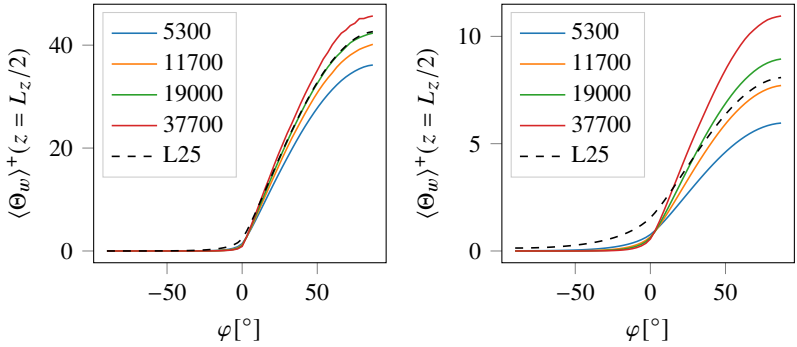

Figure 5.6: Wall temperature in viscous units at $z = L_z/2$ for $Pr = 0.71$ (left) and $Pr = 0.025$ (right).

schematically in Fig. 4.1. Effects of the Reynolds number and of the domain length are present as discussed in the previous paragraph with an increase of wall temperature with Reynolds number and an increased temperature for the longer domain length due to the longer spatial development of the thermal field. Noteworthy in this plot is the less intense peak of the wall temperature for $Pr = 0.025$, i.e. the ratio of $\langle\Theta_w\rangle^t(\varphi = 90°)/\langle\Theta_w\rangle^{\varphi,t}$ is lower than for $Pr = 0.71$ due to the high thermal diffusivity of low-Prandtl-number fluids. This is responsible for the lower Nusselt numbers evaluated at $\varphi = 90°$, shown in Fig. 5.4, and particularly pronounced in the case of $L_z = 25\,D$.

5.2.4 Radial profiles

This subsection presents radial profiles of first- and second-order statistics. On account of the short averaging period for the case at $Re_b = 37700$, second-order statistics are only presented for $Re_b = 5300$ and $Re_b = 19000$. The database of this chapter includes additionally the results of the two DNSs at $Re_b = 5300$ of domain size $L_z = 12.5\,D$ and $25\,D$ and the intermediate Reynolds number case at $Re_b = 11700$ as well as profiles evaluated at the angles of $\varphi = \pm 90°, \pm 45°, 0°$.

To distinguish the selected axial locations, the line-styles and -colors as given in Table 5.2 are used for the following profiles in Figs. 5.7 - 5.11.

Table 5.2: Line-styles and line-colors for axial location of radial profiles.

z/D	1.25	3.75	6.25	8.75	11.25
Line-style	—	—	- - -	- - -	- - -

The temperature, evaluated at the circumferential location of maximum wall heat flux $\varphi = 90°$ is presented in Fig. 5.7. This figure shows the results for the fluid with $Pr = 0.71$ in the left column and for the low-Prandtl-number fluid with $Pr = 0.025$ in the right column. The top row represents the results obtained at $Re_b = 5300$ and the bottom row the results at $Re_b = 37700$. Five axial locations, consisting of the central location at $z/D = 6.25 = L_z/2$ and two locations upstream and downstream thereof, are selected to indicate also the axial development of the thermal statistics. Note the different abscissas at different Reynolds numbers. Close to the inlet, the temperature is non-zero only in the near-wall region. This region of non-zero temperature is increasing towards the core of the flow with increasing axial development of the thermal field. Due to the high thermal diffusivity at $Pr = 0.025$, this thermal boundary layer extends further towards the core of the flow, so that at $Re_b = 5300$ already at half of the domain length $z/D = 6.25$ the temperature in the core is non-zero. A higher Reynolds number reduces the radial extension of the thermal boundary layer due to the relatively increasing effect of convection over diffusion. As pointed out in Fig. 5.5, the maximum wall temperature resides downstream of the maximum wall heat flux at $z/L_z \approx 0.6$.

The temperature variance, being important for the design of the receiver due to thermal fatigue, is shown in Fig. 5.8 for the circumferential location of maximum wall heat flux $\varphi = 90°$. Instead of the results at $Re_b = 37700$, the bottom row shows the results obtained at $Re_b = 19000$ because of the relatively short averaging period for $Re_b = 37700$. The temperature variance is non-vanishing at the wall because of the Neumann-type boundary condition, which permits fluctuations of the wall temperature. A near-wall peak is developing, moving away from the wall and closer to the core region with increasing axial location, clearly visible for $Pr = 0.025$. It gains in magnitude up to $z/L_z \approx 0.6$ and declines further downstream, similar to the axial wall temperature

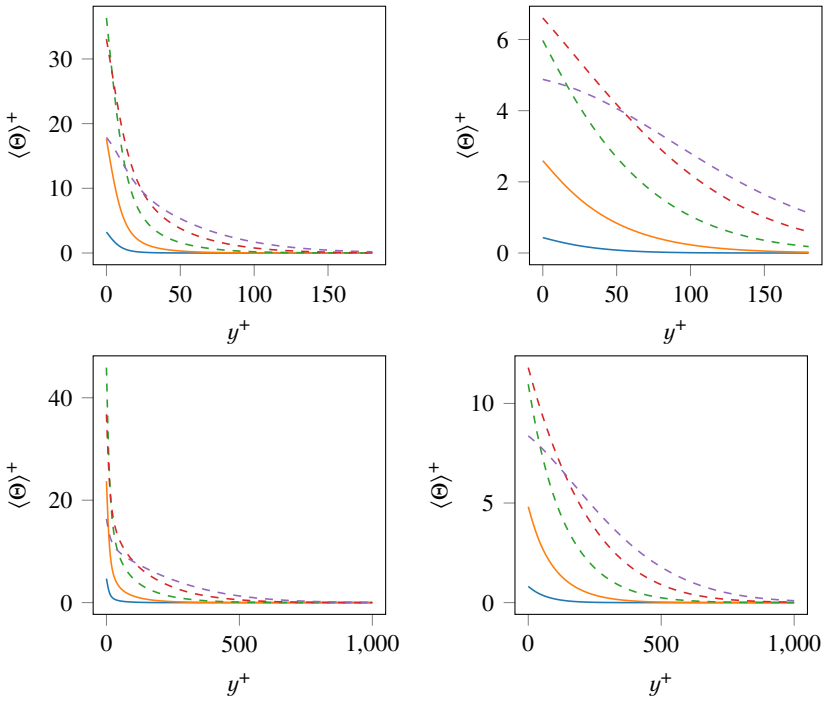

Figure 5.7: Temperature in viscous units at $\varphi = 90°$ for $Pr = 0.71$ (left) and $Pr = 0.025$ (right) and the LESs at $Re_b = 5300$ (top) and $Re_b = 37700$ (bottom).

distribution. For the lower Prandtl number $Pr = 0.025$ the peak is located further away from the all, due to the high thermal diffusivity and the larger thermal boundary layer. As the thermal field at $Re_b = 5300$ and $Pr = 0.025$ is still in a laminar-like state the thermal fluctuations are very small and they increase by approximately one order of magnitude at $Re_b = 19000$, when scaled in viscous units.

The radial distribution of the radial turbulent heat flux is directly related to the temperature distribution, as shown by Eq. (3.41). It is presented in Fig. 5.9 for the circumferential location of maximum wall heat flux $\varphi = 90°$. Similar features as for the temperature variance can be observed. The peak gains in

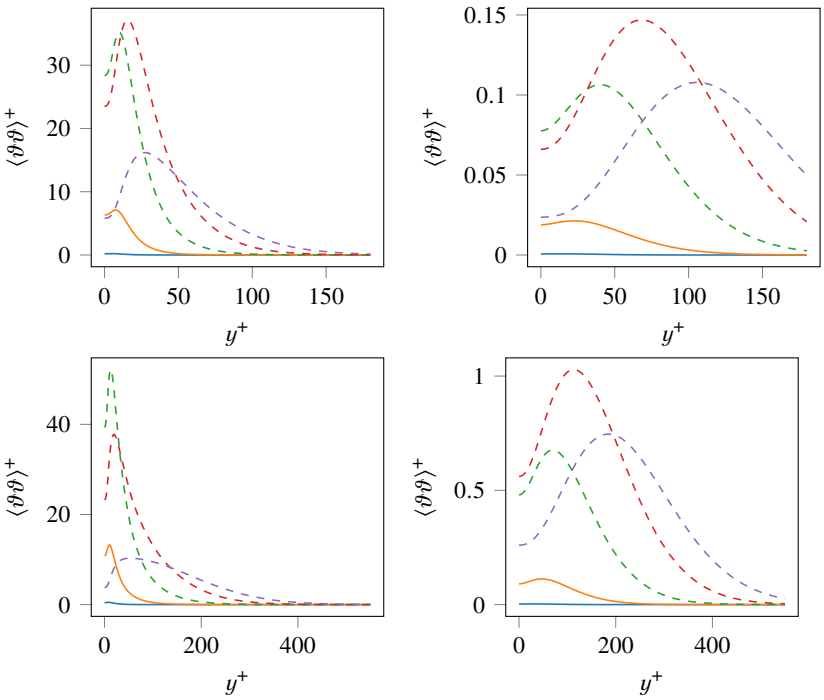

Figure 5.8: Temperature variance in viscous units at $\varphi = 90°$ for $Pr = 0.71$ (left) and $Pr = 0.025$ (right) and the LESs at $Re_b = 5300$ (top) and $Re_b = 19000$ (bottom).

magnitude and declines towards the outlet. The core of the flow exhibits non-vanishing radial turbulent heat flux for the low-Prandtl-number fluid further upstream than for $Pr = 0.71$ due to the larger thermal boundary layer. The increase in Reynolds number from $Re_b = 5300$ to $Re_b = 19000$ increases the radial turbulent heat flux of $Pr = 0.025$ approximately threefold, when scaled in viscous units. The gain is smaller than that of the temperature variance because the fluctuations of the velocity field do not increase as much as the thermal fluctuations.

Due to the symmetry of the wall heat flux boundary condition, the azimuthal turbulent heat flux vanishes at $\varphi = \pm 90°$. Therefore, it is presented at the circumferential location of $\varphi = 45°$ in Fig. 5.10. A near-wall peak is observed,

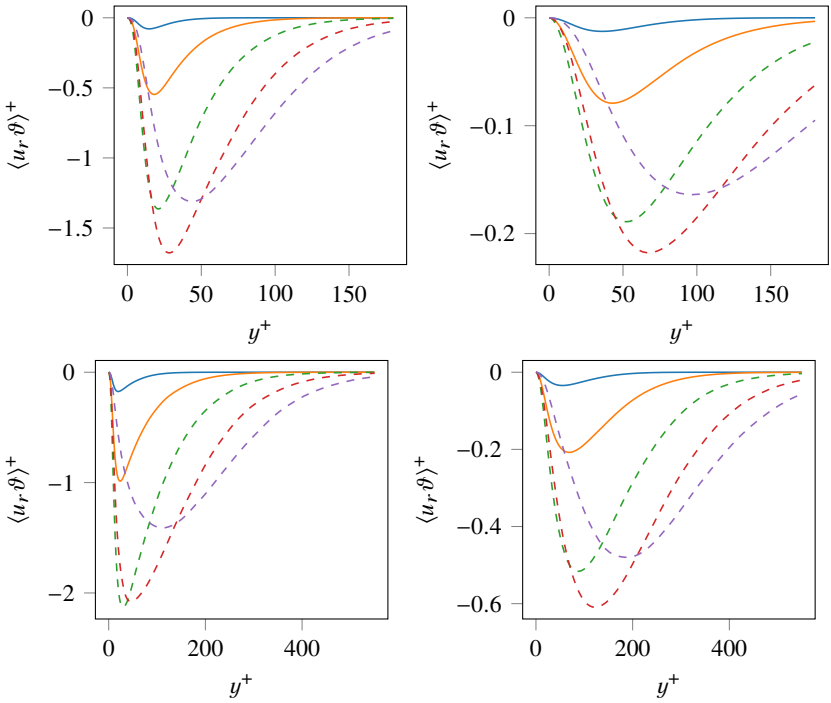

Figure 5.9: Radial turbulent heat flux at $\varphi = 90°$ for $Pr = 0.71$ (left) and $Pr = 0.025$ (right) and the LESs at $Re_b = 5300$ (top) and $Re_b = 19000$ (bottom).

gaining in magnitude and only reducing slightly close to the outlet at $z/D = 11.25$, while shifting closer to the core region when the streamwise location increases. Particularly for the case at $Re_b = 5300$ and $Pr = 0.025$, a bump is visible at $y^+ \approx 75$, which is likely caused by the high temperature variance at this location. This bump is less pronounced at the higher Reynolds number of $Re_b = 19000$ with the peak being flatter.

The streamwise turbulent heat flux evaluated at the circumferential location of maximum wall heat flux $\varphi = 90°$ is given in Fig. 5.11. For the cases of $Pr = 0.71$, the dependency on the axial location with a gain and decline is similar to what is observed for the previously presented second-order thermal statistics. The low-Prandtl-number fluid exhibits a remarkably different development.

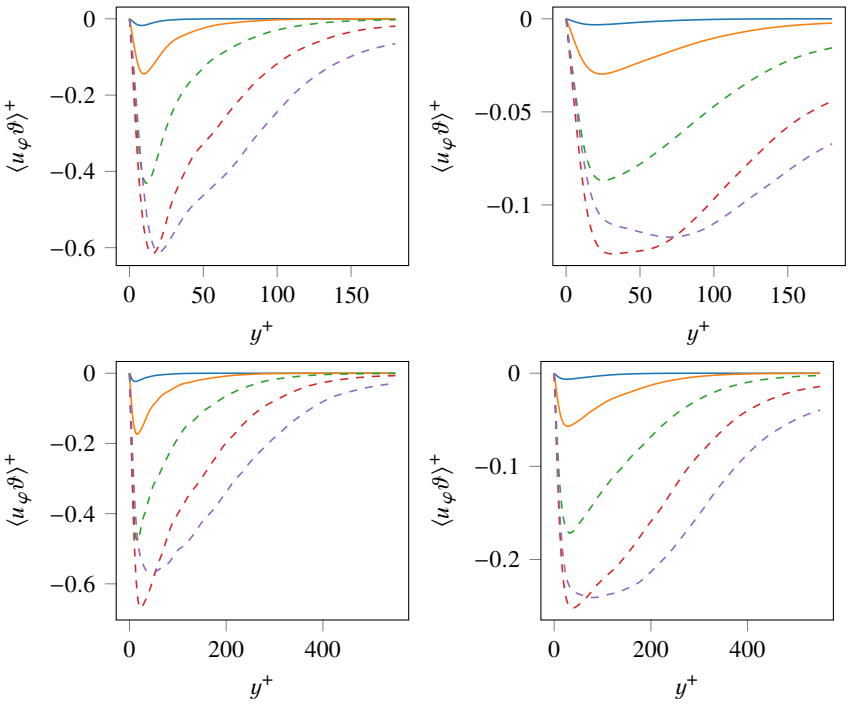

Figure 5.10: Azimuthal turbulent heat flux at $\varphi = 45°$ for $Pr = 0.71$ (left) and $Pr = 0.025$ (right) and the LESs at $Re_b = 5300$ (top) and $Re_b = 19000$ (bottom).

Close to the inlet, where the thermal fluctuations are still small and limited to the region right next to the wall, the correlation between streamwise velocity and thermal fluctuations is dominated by the fluctuations of the velocity field, building up a near wall peak at $y^+ \approx 20$. Downstream of the axial location of maximum wall heat flux , i.e. at $z/L_z > 0.5$, a second peak emerges, which is declining in magnitude due to the declining wall heat flux and shifts closer to the core region. Such a distribution, consisting of a near wall peak and an outer peak closer towards the pipe center, is also observed for the fully developed thermal field under homogeneous isoflux boundary conditions, as shown in Fig. 3.12 and discussed in the corresponding paragraph.

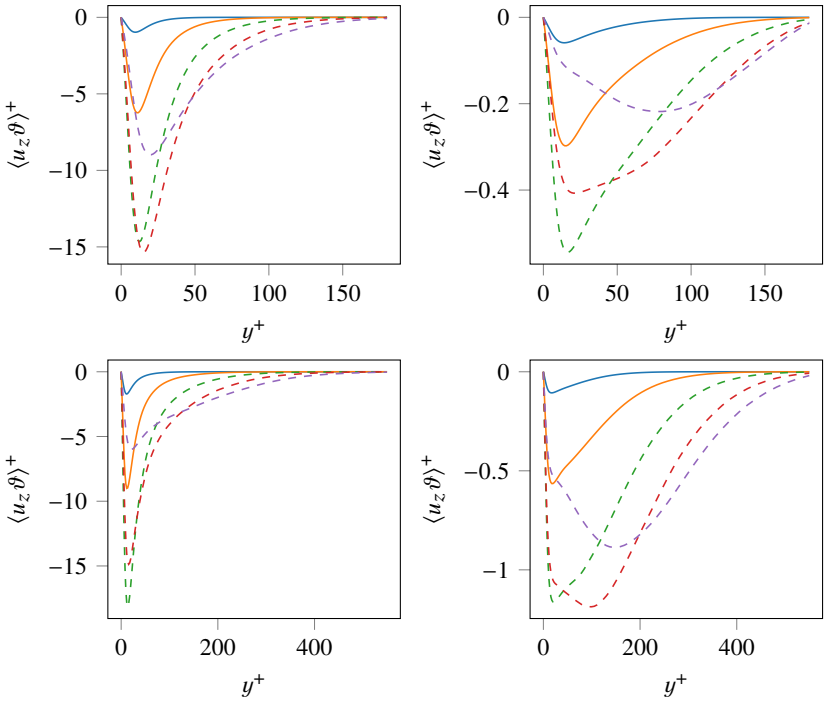

Figure 5.11: Streamwise turbulent heat flux at $\varphi = 90°$ for $Pr = 0.71$ (left) and $Pr = 0.025$ (right) and the LESs at $Re_b = 5300$ (top) and $Re_b = 19000$ (bottom).

6 Conclusions and outlook

For the efficient application of liquid metals as heat transfer fluids an improved understanding of their distinct heat transfer mechanism is essential. This study focuses on the application of liquid metals in central receiver systems. Particular in central receiver systems is the non-homogeneous thermal boundary condition applied on the receiver. Such complex thermal boundary conditions are studied numerically by direct numerical simulations and large-eddy simulations in order to generate a high-fidelity database crucial for the improvement of less computationally expensive Reynolds-averaged Navier–Stokes simulations. In a first step, "three types of thermal boundary conditions, i.e. isothermal, mixed-type and isoflux, are analyzed in a fully-developed turbulent forced convection pipe flow. The influence of the TBC on thermal statistics is assessed for bulk Reynolds numbers up to $Re_b = 37700$ and Prandtl numbers of $Pr = 0.71$, $Pr = 0.025$ by means of DNS (for $Re_b = 5300$) and well-resolved LES. For $Pr = 0.71$ the TBC barely affects the Nusselt number while for $Pr = 0.025$, the Nusselt number for IT is $\approx 20\%$ lower than for IF/MBC analogous to laminar fully-developed forced convection. This highlights the different heat transfer mechanism for low Prandtl number fluids, where the molecular conduction plays an important role even for turbulent convection at moderately high Reynolds numbers. Thermal one-point statistics are dependent on the TBC, especially for low Prandtl numbers. Due to the Dirichlet boundary condition of IT and MBC, temperature fluctuations at the wall are suppressed, leading to different near-wall behaviors of the turbulent heat fluxes compared to IF. For the same reason the premultiplied power spectral densities of IF exhibit thermal structures at the wall, which are absent for IT and MBC.

Depending on the Prandtl number and on which statistics are to be evaluated, the appropriate TBC is to be chosen. For $Pr \approx 1$ all three types give similar results except for the temperature variance at the wall. Therefore, MBC is recommended due to its simplicity in implementation. On the other hand, for $Pr \ll 1$, differences between the TBCs are more pronounced. If true isother-

mal boundary conditions are to be simulated for a low-Prandtl-number fluid, even though difficult to realize in practice, IT should be used since MBC gives significantly different results. For a constant wall heat flux condition, first-order statistics between MBC and IF agree such that MBC is recommended. Previous literature studies on conjugate heat transfer show maximum values of temperature fluctuations occuring for IF [77], representing thus the most conservative boundary condition for their estimation. The recommended TBC for low-Prandtl-number heat transfer fluids in CSP plants is IF for two reasons: First, the focused solar radiation imposes a wall heat flux boundary condition on the receiver; second, the thermal fluctuations of the wall temperature, which are only reproduced by IF, should be taken into account when designing the receiver.

The presented results of first- and second-order statistics together with the Nusselt number and its contributions are hosted in the open access repository KITopen [SSD1]. Due to the limited numerical (and experimental) data available of heat transfer in liquid metals, this database can serve as reference data for testing and improving Reynolds-averaged Navier–Stokes (RANS) models. Individual contributions to the budget of the temperature variance and budgets of the turbulent heat fluxes in radial and streamwise direction [...] are also available in the database."[SSA2]

Using the findings of the study on the influence of the type of thermal boundary conditions in a homogeneous setup, the isoflux boundary condition is selected and prescribed for the simulations of non-homogeneous thermal boundary conditions. The complexity of the thermal boundary condition is increased gradually, by first studying azimuthally non-homogeneous thermal boundary conditions. The same parameter space of Reynolds numbers from $Re_b = 5300$ to $Re_b = 37700$ and two Prandtl numbers of $Pr = 0.71$ and $Pr = 0.025$ is studied for fully developed turbulent forced convection pipe flow where the surface heat flux is applied non-homogeneously in azimuthal direction. The thermal boundary condition is derived from the application in central receiver systems and features one adiabatic half and one heated half of the pipe wall. On the heated part either a constant wall heat flux or a sinusoidal distribution of the wall heat flux is imposed. For this setup "the azimuthally averaged global Nusselt number Nu^G practically coincides with that for a uniform applied surface heat flux. The locally defined Nusselt number exhibits a plateau over a wide range of the heated section, where the results for the sinusoidal and

constant wall heat flux collapse. Within this region, the locally defined Nusselt number is approximately 20 % and 50 % lower than its respective global value for $Pr = 0.71$ and $Pr = 0.025$. Large values for the local Nusselt number occur close to the edge of the heated section, where the wall temperature is close to the bulk temperature. The temperature profiles only present logarithmic regions within the heated part of the pipe at $Pr = 0.71$, while it is absent for $Pr = 0.025$ even at $Re_b = 37700$. The radial and azimuthal thermal diffusivities show only a weak dependency on the circumferential location, therefore being practically only a function of the radial location. For $Re_b = 37700$, the turbulent Prandtl numbers of $Pr = 0.71$ and $Pr = 0.025$ attain an approximately constant value for $y^+ > 500$, where it is isotropic and approximately unity."[SSA1]

A proper orthogonal decomposition of the thermal fields reveals a higher concentration of energy in the first modes for low-Prandtl-number fluids compared to $Pr \approx 1$. This is due to the comparatively larger thermal structures present at low Prandtl numbers. Therefore, fewer modes are required to capture 90% of the energy for a fluid of a low Prandtl number of $Pr = 0.025$, i.e. $12 - 40$ modes in the range of $Re_b = 5300$ to $Re_b = 37700$, compared to $105 - 374$ modes for $Pr = 0.71$. Even though the relative energy of the modes is different between the two considered Prandtl numbers, the spatial distribution of the first mode is very similar, especially for high enough Reynolds numbers like $Re_b = 37700$.

A second database including the presented results of first- and second-order thermal statistics of the azimuthally non-homogeneous thermal boundary conditions is hosted also in the open access repository KITopen [SSD3].

Increasing the complexity of the thermal boundary conditions one step further, an axially and azimuthally inhomogeneously distributed wall heat flux is studied. The distribution of the wall heat flux in azimuthal direction is considered adiabatic on one half of the pipe and a sinusoidal wall heat flux distribution is imposed on the other half. In axial direction a Gaussian function for the wall heat flux is selected to represent the locality of the wall heat flux imposed on the receiver of an actual central receiver system. The same parameter space of Reynolds and Prandtl numbers as before is explored. Locally evaluated Nusselt numbers at the azimuthal location of maximum heat flux and the azimuthally averaged Nusselt number are compared and yield very similar distributions for $Pr \approx 1$, with increased Nusselt numbers at high Reynolds numbers. For lower Prandtl numbers however, the local Nusselt numbers are lower than the cir-

cumferentially averaged ones due to the high thermal diffusivity causing a less intense peak of the wall temperature at the location of maximum wall heat flux. The wall temperature, normalized in viscous units, exhibits an increasing trend with increasing Reynolds number, more pronounced for low Prandtl numbers. It reaches its maximum downstream of the axial location of maximum wall heat flux at $z/L_z \approx 0.6$ compared to $z/L_z = 0.5$, respectively, irrespective of the Reynolds and Prandtl numbers. In azimuthal direction, the wall temperatures spread more evenly for low-Prandtl-number fluids causing the temperature to increase stronger in the adiabatic part of the pipe than for fluids of $Pr \approx 1$. Radial profiles of first- and second-order thermal statistics evaluated at the azimuthal location of maximum wall heat flux and at selected axial locations display differences in the axial development of the thermal field. The thermal boundary layer extends further towards the core of the flow for low-Prandtl-number fluids moving also the peak of the thermal fluctuations further away from the wall. A peculiarity in the turbulent heat flux in streamwise direction for the low-Prandtl-number fluid is the appearance of a near-wall peak and an outer peak closer towards the center of the pipe caused by the radial separation of the maxima of thermal fluctuations and fluctuations of streamwise velocity as observed also in the fully developed homogeneous setup.

The presented results of the axially and azimuthally inhomogeneous thermal boundary conditions are included in a third database and hosted in the open access repository KITopen [SSD2].

A natural extension for future projects is to lift some of the underlying assumptions of the present simulations. First, the assumption of constant thermophysical properties could be lifted. This assumption simplifies the numerical simulations and is therefore often applied in the literature. However, when the difference in physical temperatures is not small enough, temperature dependent thermophysical properties should be considered in order to model the turbulent heat transfer appropriately, as done recently by Antoranz [3] for $Re_\tau = 180$ and $Pr = 0.7$. Among other things, they encounter secondary motions induced by the non-isotropic fluid properties.

Second, the influence of buoyancy forces could be taken into account. Depending on the operating conditions of the central receiver facility, the effects of

buoyancy forces on velocity and thermal statistics could become non-negligible in a mixed convection regime. For two Reynolds numbers of $Re_b = 5300$ and $Re_b = 11690$, aided mixed convection is studied for homogeneous thermal boundary conditions by means of LES by Centurelli [T2] additionally extending the decomposition of the Nusselt number to mixed convection. To explore the parameter space for mixed convection in liquid metals, higher Reynolds numbers should be considered in the future together with a selection of Richardson numbers to accommodate for different flow regimes.

Third, conduction within the solid wall could be taken into account by including an additional partial differential equation for the temperature in the solid body coupled with the system of partial differential equations for the heat transfer in the fluid (conjugate heat transfer). Since material parameters for the fluid and the solid under consideration need to be prescribed, the results will be specific for this combination of fluid/solid and less general.

Fourth, different types of inlet conditions and their effect on the heat transfer could be examined. The inflow conditions for velocity and temperature might be strongly affected by the pipe routing. For instance a bend in proximity, upstream, of the region of heat input could introduce another inhomogeneity of the mean velocity field (in streamwise and azimuthal direction) on top of the non-homogeneous thermal boundary conditions.

A Appendix

A.1 Estimations to support assumptions

Some of the assumptions discussed in Section 2.1 rely on order of magnitude estimates which are given in the following paragraphs.

Maximum temperature difference In the setup of homogeneous TBCs, the maximum non-dimensionalized temperature for $Pr = 0.025$ is $\langle \Theta_h \rangle^+ = 10$. In order to convert the non-dimensionalized temperature differences to physical temperature differences, the definition of

$$\Theta_h^+ = \frac{\langle T_w \rangle^t - T}{\langle q_w \rangle^t} \rho c_p u_\tau \tag{A.1}$$

needs to be recalled and physical parameters of the experiment need to be taken into account. The wall heat flux density on the receiver is in the order of $q_w \approx 1\,\mathrm{MW\,m^{-2}}$ [20, 58, 59]. The working temperature of the liquid metal is estimated to be at $T = 600\,\mathrm{K}$, so that the molecular Prandtl number is close to the prescribed value of $Pr = 0.025$, according the temperature dependent thermophysical properties given by Fazio et al. [18]. At this temperature, density, specific heat capacity at constant pressure, dynamic and kinematic viscosity as well as thermal conductivity for LBE are [18]

$$\rho = 1.0 \times 10^4\,\mathrm{kg\,m^{-3}} \tag{A.2}$$

$$c_p = 144\,\mathrm{J\,kg^{-1}\,K^{-1}} \tag{A.3}$$

$$\mu = 1.8 \times 10^{-3}\,\mathrm{Pa\,s} \tag{A.4}$$

$$\nu = 1.7 \times 10^{-7}\,\mathrm{m^2\,s^{-1}} \tag{A.5}$$

$$\lambda = 12\,\mathrm{W\,m^{-1}\,K^{-1}} \tag{A.6}$$

The inner diameter of the receiver tube is estimated to be in the order of $D = 0.01\,\mathrm{m}$ [10].

The highest Reynolds number simulated in the present thesis is $Re_b = 37700$, $Re_\tau = 1000$, which gives a friction velocity of $u_\tau = 0.034\,\mathrm{m\,s^{-1}}$. The maximum physical temperature difference is therefore

$$\langle\langle T_w\rangle^t - T\rangle = \frac{\langle\Theta_h\rangle^+\langle q_w\rangle}{\rho c_p u_\tau} = 200\,\mathrm{K}. \tag{A.7}$$

In the setup of azimuthally non-homogeneous TBCs, the non-dimensionalized temperature for $Pr = 0.025$ ranges from $\langle\Theta_{az}\rangle^+ = -27$ to $\langle\Theta_{az}\rangle^+ = 9$ and the non-dimensionalized temperature is given by

$$\Theta^+_{az} = \frac{T_b - T}{\langle q_w\rangle^\varphi}\rho c_p u_\tau \tag{A.8}$$

Due to the half sinusoidal distribution of the wall heat flux density, the azimuthal average is $\langle q_w\rangle^\varphi = 32 \times 10^5\,\mathrm{MW\,m^{-2}}$ for a maximum $q_w(\varphi = \pi/2) = 1\,\mathrm{MW\,m^{-2}}$.

The maximum physical temperature differences are therefore

$$\langle T_b - T_w\rangle|_{\varphi=\pi/2} = \frac{\langle\Theta_{az}\rangle^+\langle q_w\rangle^\varphi}{\rho c_p u_\tau} = -171\,\mathrm{K} \tag{A.9}$$

$$\langle T_b - T_w\rangle|_{\varphi=-\pi/2} = 57\,\mathrm{K} \tag{A.10}$$

so that the maximum temperature difference between heated and adiabatic wall is $\langle T_w|_{\varphi=\pi/2} - T_w|_{\varphi=-\pi/2}\rangle = 229\,\mathrm{K}$.

Heating due to viscous dissipation The pseudo-dissipation as a result from the numerical simulation is $\tilde{\epsilon}^+ < 0.027$ for the case of $Re_b = 37700$. Converted into dimensional units, using $U_b = Re_b D/\nu = 0.64\,\mathrm{m\,s^{-1}}$, this is

$$\tilde{\epsilon} = \frac{U_b^3}{D}\frac{Re_\tau^4}{Re_b^3}\tilde{\epsilon}^+ < 7.7\,\mathrm{m^2\,s^{-3}} \tag{A.11}$$

The source term in the non-dimensional temperature equation, which accounts for the mean axial advective heat flux, is $S_\Theta = 4U_z/U_b \approx 5$ and the heating due to viscous dissipation (in the same non-dimensionalization) is

$$\tilde{\epsilon}\frac{D\rho}{q_w} = 8 \times 10^{-4} \tag{A.12}$$

which is orders of magnitude smaller than the source term (convective term).

Buoyancy forces The thermal expansion coefficient at $T = 600\,\mathrm{K}$ is [18]

$$\beta = -\frac{1}{\rho}\left(\frac{\partial\rho}{\partial T}\right)_p = 1.3 \times 10^{-4}\,\mathrm{K}^{-1} \tag{A.13}$$

and the gravitational acceleration is $g = 9.81\,\mathrm{m\,s}^{-2}$ Therefore, the Grashof number (based on the wall heat flux) yields

$$Gr = \frac{g\beta q_w D^4}{\lambda\nu^2} = 3.6 \times 10^7 \tag{A.14}$$

One criteria to assess the importance of buoyancy effects is to compute the ratio of

$$\frac{Gr}{Re_b^2} = 0.025 \ll 1 \tag{A.15}$$

for $Re_b = 37700$, indicating the dominance of forced over natural convection [32]. A second criteria to asses the importance of buoyancy forces goes back to Jackson, Cotton, and Axcell [33], defining a buoyancy parameter, which has recently been employed also for liquid metals [49, 51],

$$Bo = 8 \times 10^4 \cdot \frac{Gr}{Re^{3.425}Pr^{0.8}} = 8 \times 10^4 \cdot 1.7 \times 10^{-7} = 1.3 \times 10^{-2} \tag{A.16}$$

encouraging the assumption of negligible buoyancy forces.

A.2 Budget Equations

A.2.1 Turbulent Kinetic Energy

"The budget of the turbulent kinetic energy $k = 1/2\langle u_i u_i \rangle$ is given as

$$\frac{\bar{D}k}{\bar{D}t} = P^k + \Pi^k - \tilde{\epsilon}^k + D^k + T^k \tag{A.17}$$

where the individual terms are the production P^k, pressure-related diffusion Π^k, pseudo-dissipation $\tilde{\epsilon}^k$, viscous diffusion D^k and turbulent velocity related diffusion T^k, defined as (cf. [17])

$$P^k = -\langle u_i u_k \rangle \frac{\partial \langle U_i \rangle}{\partial x_k}, \qquad \Pi^k = -\frac{1}{\rho}\left\langle u_i \frac{\partial p'}{\partial x_i} \right\rangle, \qquad \tilde{\epsilon}^k = \nu \left\langle \frac{\partial u_i}{\partial x_k} \frac{\partial u_i}{\partial x_k} \right\rangle \tag{A.18}$$

$$D^k = \frac{\nu}{2} \frac{\partial^2 \langle u_i u_i \rangle}{\partial x_k \partial x_k}, \qquad T^k = -\frac{1}{2} \frac{\partial \langle u_i u_i u_k \rangle}{\partial x_k} \tag{A.19}$$

Note that the pseudo-dissipation is defined to be positive, as given in Pope [64], whereas Ref. [17] defines it to be negative, and the pressure is decomposed into mean and fluctuating part as $p = \langle p \rangle + p'$, while velocity and thermal field are decomposed as in Eq. (3.10)."[SSA2]

A.2.2 Temperature Variance and Turbulent Heat Fluxes

"Additionally, the temperature variance and turbulent heat flux budgets are presented for completeness, since the individual contributions are also contained in the database. The budgets for the temperature variance with $k^\vartheta = 1/2\langle \vartheta\vartheta \rangle$ and turbulent heat fluxes $\langle u_i \vartheta \rangle$ are given by

$$\frac{\bar{D}k^\vartheta}{\bar{D}t} = \left(\mathrm{P}^\vartheta + \epsilon^\vartheta + \mathrm{MD}^\vartheta + \mathrm{TD}^\vartheta + \mathrm{S}^\vartheta \right) \tag{A.20}$$

$$\frac{\bar{D}\langle u_i \vartheta \rangle}{\bar{D}t} = \mathrm{P}_{i\Theta} + \mathrm{TPG}_{i\Theta} + \mathrm{TD}_{i\Theta} + \epsilon_{i\Theta} + \mathrm{MD}_{i\Theta} + \mathrm{S}_{i\theta} \tag{A.21}$$

where the individual terms are the production P^{ϑ}, the dissipation ϵ^{ϑ}, the molecular diffusion MD^{ϑ} and the turbulent diffusion TD^{ϑ} of the temperature variance, defined as (cf.[35])

$$\mathrm{P}^{\vartheta} = -\langle u_i \vartheta \rangle \frac{\partial \langle \Theta \rangle}{\partial x_i}, \qquad \epsilon^{\vartheta} = -\alpha \left\langle \frac{\partial \vartheta}{\partial x_i} \frac{\partial \vartheta}{\partial x_i} \right\rangle \tag{A.22}$$

$$\mathrm{MD}^{\vartheta} = \frac{\alpha}{2} \frac{\partial^2 \langle \vartheta \vartheta \rangle}{\partial x_i \partial x_i}, \qquad \mathrm{TD}^{\vartheta} = -\frac{1}{2} \frac{\partial \langle u_i \vartheta \vartheta \rangle}{\partial x_i} \tag{A.23}$$

and the production $\mathrm{P}_{i\Theta}$, temperature-pressure gradient $\mathrm{TPG}_{i\Theta}$, turbulent diffusion $\mathrm{TD}_{i\Theta}$, dissipation $\epsilon_{i\Theta}$ and molecular diffusion $\mathrm{MD}_{i\Theta}$ of turbulent heat fluxes, defined as (cf.[35])

$$\mathrm{P}_{i\Theta} = -\langle u_i u_k \rangle \frac{\partial \langle \Theta \rangle}{\partial x_k} - \langle u_k \vartheta \rangle \frac{\partial \langle U_i \rangle}{\partial x_k}, \qquad \mathrm{TPG}_{i\Theta} = -\frac{1}{\rho} \left\langle \vartheta \frac{\partial p'}{\partial x_i} \right\rangle \tag{A.24}$$

$$\mathrm{TD}_{i\Theta} = -\frac{\partial \langle \vartheta u_i u_k \rangle}{\partial x_k}, \qquad \epsilon_{i\Theta} = -\alpha(1 + Pr) \left\langle \frac{\partial \vartheta}{\partial x_k} \frac{\partial u_i}{\partial x_k} \right\rangle \tag{A.25}$$

$$\mathrm{MD}_{i\Theta} = \frac{\partial}{\partial x_k} \left(\alpha \left\langle u_i \frac{\partial \vartheta}{\partial x_k} \right\rangle + \alpha Pr \left\langle \vartheta \frac{\partial u_i}{\partial x_k} \right\rangle \right) \tag{A.26}$$

Note that the dissipation of temperature variance and of the turbulent heat fluxes is defined with a negative sign conforming to Kasagi and Ohtsubo [35].

The source term contributions for the temperature variance and turbulent heat fluxes depend on the type of thermal boundary condition [62]

$$\mathrm{S}^{\vartheta} = \begin{cases} 4\langle u_z \vartheta \rangle / D & \text{MBC, IF} \\ a \left(\langle U_z \rangle \langle \vartheta \vartheta \rangle + \langle \Theta \rangle \langle u_z \vartheta \rangle + \langle u_z \vartheta \vartheta \rangle - \alpha \dfrac{\partial \langle \vartheta \vartheta \rangle}{\partial z} + \alpha a \langle \vartheta \vartheta \rangle \right) & \text{IT} \end{cases} \tag{A.27}$$

$$\mathrm{S}_{i\Theta} = \begin{cases} 4\langle u_z u_i \rangle / D & \text{MBC, IF} \\ a \left(\langle U_z \rangle \langle \vartheta u_i \rangle + \langle \Theta \rangle \langle u_z u_i \rangle + \langle u_z u_i \vartheta \rangle - \alpha 2 \left\langle \dfrac{\partial \vartheta}{\partial z} u_i \right\rangle + \alpha a \langle \vartheta u_i \rangle \right) & \text{IT} \end{cases} \tag{A.28}$$

Note that the budgets for temperature variance and turbulent heat fluxes are given in dimensional units whereas Kasagi and Ohtsubo [35] state them in viscous units."[SSA2]

References

[1] H. Abe, H. Kawamura, and Y. Matsuo. "Surface heat-flux fluctuations in a turbulent channel flow up to $Re_\tau = 1020$ with Pr =0.025 and 0.71". In: *Int. J. Heat Fluid Flow* 25.3 (2004), pp. 404–419. ISSN: 0142-727X. DOI: https://doi.org/10.1016/j.ijheatfluidflow.2004.02.010.

[2] F. Alcántara-Ávila, S. Hoyas, and M. Pérez-Quiles. "DNS of thermal channel flow up to Re_τ=2000 for medium to low Prandtl numbers". In: *Int. J. Heat Mass Tran.* 127 (2018), pp. 349–361. ISSN: 0017-9310. DOI: https://doi.org/10.1016/j.ijheatmasstransfer.2018.06.149.

[3] A. Antoranz. "A numerical study of turbulent heat transfer in pipes". PhD thesis. Madrid, Spain: Universidad Carlos III de Madrid. Departamento de Bioingeniería e Ingeniería Aeroespacial, 2017. URL: http://hdl.handle.net/10016/25815.

[4] A. Antoranz, A. Gonzalo, O. Flores, and M. García-Villalba. "Numerical simulation of heat transfer in a pipe with non-homogeneous thermal boundary conditions". In: *Int. J. Heat Fluid Flow* 55 (2015), pp. 45–51. ISSN: 0142-727X. DOI: https://dx.doi.org/10.1016/j.ijheatfluidflow.2015.05.007.

[5] A. Antoranz, A. Ianiro, O. Flores, and M. García-Villalba. "Extended proper orthogonal decomposition of non-homogeneous thermal fields in a turbulent pipe flow". In: *Int. J. Heat Mass Tran.* 118 (2018), pp. 1264–1275. ISSN: 0017-9310. DOI: https://doi.org/10.1016/j.ijheatmasstransfer.2017.11.076.

[6] A. Barletta and S. Lazzari. "Combined forced and free flow in a vertical circular duct subjected to non-axisymmetric wall heating conditions". In: *Int. J. Heat Mass Tran.* 50.25-26 (Dec. 2007), pp. 4927–4936. DOI: https://doi.org/10.1016/j.ijheatmasstransfer.2007.03.039.

[7] A. Barletta, S. Lazzari, and E. Zanchini. “Non-axisymmetric forced and free flow in a vertical circular duct”. In: *Int. J. Heat Mass Tran.* 46.23 (2003), pp. 4499–4512. ISSN: 0017-9310. DOI: https://doi.org/10.1016/S0017-9310(03)00284-9.

[8] A. Bejan. *Convection Heat Transfer*. 4th ed. Hoboken, New Jersey: Wiley, 2013. ISBN: 978-1-118-33448-5.

[9] A. W. Black and E. M. Sparrow. “Experiments on Turbulent Heat Transfer in a Tube With Circumferentially Varying Thermal Boundary Conditions”. In: *J. Heat Transfer* 89.3 (1967), pp. 258–268. DOI: https://doi.org/10.1115/1.3614375.

[10] R. W. Bradshaw et al. *Final Test and Evaluation Results from the Solar Two Project*. Tech. rep. SAND2002-0120. Albuquerque, NM 87185-0703: Sandia National Laboratories, Jan. 2002. DOI: https://doi.org/10.2172/793226.

[11] C. Canuto, M. Y. Hussaini, A. Quarteroni, and T. A. Zang. *Spectral Methods: evolution to complex geometries and applications to fluid dynamics*. Scientific ComputationSpringerLink. Berlin, Heidelberg: Springer Berlin Heidelberg, 2007. ISBN: 3540307273.

[12] A. Chatterjee. “An introduction to the proper orthogonal decomposition”. In: *Current Science* 78.7 (2000), pp. 808–817. ISSN: 00113891. URL: http://www.jstor.org/stable/24103957.

[13] C. Chin, A. S. H. Ooi, I. Marusic, and H. M. Blackburn. “The influence of pipe length on turbulence statistics computed from direct numerical simulation data”. In: *Phys. Fluids* 22.11 (2010), p. 115107. DOI: https://doi.org/10.1063/1.3489528.

[14] W. Couzy. “Spectral element discretization of the unsteady Navier-Stokes equations and its iterative solution on parallel computers”. PhD thesis. Lausanne, Switzerland: Lausanne, EPFL, 1995. DOI: https://doi.org/10.5075/epfl-thesis-1380.

[15] M. O. Deville, P. F. Fischer, and E. H. Mund. *High-order methods for incompressible fluid flow*. Vol. 9. Cambridge monographs on applied and computational mathematics ; 9. Cambridge, UK: Cambridge University Press, 2002.

[16] B. Eckhardt, S. Grossmann, and D. Lohse. “Torque scaling in turbulent Taylor–Couette flow between independently rotating cylinders”. In: *J. Fluid Mech.* 581 (May 2007), pp. 221–250. DOI: https://doi.org/10.1017/s0022112007005629.

[17] G. K. El Khoury, P. Schlatter, A. Noorani, P. F. Fischer, G. Brethouwer, and A. V. Johansson. “Direct numerical simulation of turbulent pipe flow at moderately high Reynolds numbers”. In: *Flow Turbul. Combust.* 91.3 (2013), pp. 475–495. ISSN: 1573-1987. DOI: https://dx.doi.org/10.1007/s10494-013-9482-8.

[18] C. Fazio et al. *Handbook on Lead-bismuth Eutectic Alloy and Lead Properties, Materials Compatibility, Thermal-hydraulics and Technologies - 2015 Edition*. Tech. rep. 32.01.13; LK 01. Issy-les-Moulineaux, France: OECD/NEA, 2015. 948 pp.

[19] C. Flageul, S. Benhamadouche, É. Lamballais, and D. Laurence. “DNS of turbulent channel flow with conjugate heat transfer: Effect of thermal boundary conditions on the second moments and budgets”. In: *Int. J. Heat Fluid Flow* 55 (2015), pp. 34–44. DOI: https://doi.org/10.1016/j.ijheatfluidflow.2015.07.009.

[20] J. Flesch, A. Fritsch, G. Cammi, L. Marocco, F. Fellmoser, J. Pacio, and T. Wetzel. “Construction of a Test Facility for Demonstration of a Liquid Lead-bismuth-cooled 10 kW Thermal Receiver in a Solar Furnace Arrangement - SOMMER”. In: *Energy Procedia* 69 (2015). International Conference on Concentrating Solar Power and Chemical Energy Systems, SolarPACES 2014, Beijing, China, pp. 1259–1268. ISSN: 1876-6102. DOI: https://dx.doi.org/10.1016/j.egypro.2015.03.157.

[21] O. Flores, C. Marugán-Cruz, D. Santana, and M. García-Villalba. “Thermal Stresses Analysis of a Circular Tube in a Central Receiver”. In: *Energy Procedia* 49 (2014), pp. 354–362. ISSN: 1876-6102. DOI: https://dx.doi.org/10.1016/j.egypro.2014.03.038.

[22] A. Fritsch, R. Uhlig, L. Marocco, C. Frantz, R. Flesch, and B. Hoffschmidt. “A comparison between transient CFD and FEM simulations of solar central receiver tubes using molten salt and liquid metals”. In: *Sol. Energy* 155 (2017), pp. 259–266. ISSN: 0038-092X. DOI: https://dx.doi.org/10.1016/j.solener.2017.06.022.

[23] K. Fukagata, K. Iwamoto, and N. Kasagi. "Contribution of Reynolds stress distribution to the skin friction in wall-bounded flows". In: *Phys. Fluids* 14.11 (Nov. 2002), pp. L73–L76. DOI: https://doi.org/10.1063/1.1516779.

[24] K. Fukagata, K. Iwamoto, and N. Kasagi. "Novel turbulence control strategy for simultaneously achieving friction drag reduction and heat transfer augmentation". In: *Proc. 4th Int. Symp. Turbulence and Shear Flow Phenomena*. Williamsburg, Virginia, June 2005, pp. 307–312.

[25] D. Gatti, A. Cimarelli, Y. Hasegawa, B. Frohnapfel, and M. Quadrio. "Global energy fluxes in turbulent channels with flow control". In: *J. Fluid Mech.* 857 (Oct. 2018), pp. 345–373. DOI: https://doi.org/10.1017/jfm.2018.749.

[26] V. Gnielinski. "Neue Gleichungen für den Wärme- und den Stoffübergang in turbulent durchströmten Rohren und Kanälen". In: *Forschung im Ingenieurwesen A* 41.1 (1975), pp. 8–16. ISSN: 1434-0860. DOI: https://doi.org/10.1007/BF02559682.

[27] G. Grötzbach. "Challenges in low-Prandtl number heat transfer simulation and modelling". In: *Nucl. Eng. Des.* 264 (2013). SI: 14th International Topical Meeting on Nuclear Reactor Thermal Hydraulics (NURETH-14), pp. 41–55. ISSN: 0029-5493. DOI: https://doi.org/10.1016/j.nucengdes.2012.09.039.

[28] G. Grötzbach. "Revisiting the resolution requirements for turbulence simulations in nuclear heat transfer". In: *Nucl. Eng. Des.* 241.11 (2011). SI: 13th International Topical Meeting on Nuclear Reactor Thermal Hydraulics (NURETH-13), Kanazawa, Japan, pp. 4379–4390. ISSN: 0029-5493. DOI: https://doi.org/10.1016/j.nucengdes.2010.12.027.

[29] G. Hagedorn et al. "The concerns of the young protesters are justified: A statement by Scientists for Future concerning the protests for more climate protection". In: *GAIA - Ecological Perspectives for Science and Society* 28.2 (Jan. 2019), pp. 79–87. ISSN: 0940-5550. DOI: https://doi.org/10.14512/gaia.28.2.3.

[30] H. Herwig. *Strömungsmechanik: Einführung in die Physik von technischen Strömungen*. 2., überarbeitete und erweiterte Auflage. Lehrbuch. Wiesbaden: Springer Vieweg, 2016. ISBN: 978-3-658-12982-8. DOI: https://doi.org/10.1007/978-3-658-12982-8.

[31] P. Holmes, J. Lumley, G. Berkooz, and C. Rowley. *Turbulence, Coherent Structures, Dynamical Systems and Symmetry*. 2. ed. Cambridge monographs on mechanics. Cambridge: Cambridge University Press, 2012. 402 pp. ISBN: 9781107008250.

[32] F. P. Incropera, D. P. DeWitt, T. L. Bergmann, and A. S. Lavine. *Fundamentals of Heat and Mass Transfer*. 6. ed. Hoboken, NJ: Wiley, 2007. ISBN: 978-0-471-45728-2.

[33] J. Jackson, M. Cotton, and B. Axcell. "Studies of mixed convection in vertical tubes". In: *Int. J. Heat Fluid Flow* 10.1 (Mar. 1989), pp. 2–15. DOI: https://doi.org/10.1016/0142-727x(89)90049-0.

[34] B. Kader. "Temperature and concentration profiles in fully turbulent boundary layers". In: *Int. J. Heat Mass Tran.* 24.9 (1981), pp. 1541–1544. ISSN: 0017-9310. DOI: https://doi.org/10.1016/0017-9310(81)90220-9.

[35] N. Kasagi and Y. Ohtsubo. "Direct Numerical Simulation of Low Prandtl Number Thermal Field in a Turbulent Channel Flow". In: *Turbulent Shear Flows 8*. Ed. by F. Durst, R. Friedrich, B. E. Launder, F. W. Schmidt, U. Schumann, and J. H. Whitelaw. Berlin, Heidelberg: Springer Berlin Heidelberg, 1993, pp. 97–119. ISBN: 978-3-642-77674-8. DOI: https://doi.org/10.1007/978-3-642-77674-8_8.

[36] N. Kasagi, Y. Tomita, and A. Kuroda. "Direct numerical simulation of passive scalar field in a turbulent channel flow". In: *J. Heat Transf.* 114.3 (Aug. 1992), pp. 598–606. ISSN: 0022-1481. DOI: https://doi.org/10.1115/1.2911323.

[37] N. Kasagi, Y. Hasegawa, K. Fukagata, and K. Iwamoto. "Control of Turbulent Transport: Less Friction and More Heat Transfer". In: *J. Heat Transfer* 134.3 (Jan. 2012), p. 031009. ISSN: 0022-1481. DOI: https://doi.org/10.1115/1.4005151.

[38] H. Kawamura, H. Abe, and Y. Matsuo. “DNS of turbulent heat transfer in channel flow with respect to Reynolds and Prandtl number effects”. In: *Int. J. Heat Fluid Flow* 20.3 (1999), pp. 196–207. ISSN: 0142-727X. DOI: http://dx.doi.org/10.1016/S0142-727X(99)00014-4.

[39] H. Kawamura, K. Ohsaka, H. Abe, and K. Yamamoto. “DNS of turbulent heat transfer in channel flow with low to medium-high Prandtl number fluid”. In: *Int. J. Heat Fluid Flow* 19.5 (1998), pp. 482–491. ISSN: 0142-727X. DOI: https://dx.doi.org/10.1016/S0142-727X(98)10026-7.

[40] J. Kim, P. Moin, and R. Moser. “Turbulence statistics in fully developed channel flow at low Reynolds number”. In: *J. Fluid Mech.* 177 (1987), pp. 133–166. DOI: https://doi.org/10.1017/S0022112087000892.

[41] J. Kim and P. Moin. *Transport of Passive Scalars in Turbulent Channel Flow*. Tech. rep. NASA Technical Memorandum 89463. NASA Ames Research Center, July 1987.

[42] H. Kong, H. Choi, and J. S. Lee. “Direct numerical simulation of turbulent thermal boundary layers”. In: *Phys. Fluids* 12.10 (2000), pp. 2555–2568. DOI: https://doi.org/10.1063/1.1287912.

[43] D. A. Kopriva. *Implementing Spectral Methods for Partial Differential Equations: Algorithms for Scientists and Engineers*. Scientific computation. Dordrecht: Springer Netherlands, 2009. 394 pp. ISBN: 978-90-481-2261-5. DOI: https://doi.org/10.1007/978-90-481-2261-5.

[44] P. K. Kundu, I. M. Cohen, and D. R. Dowling. *Fluid Mechanics*. 5. ed. Amsterdam: Elsevier Academic Press, 2012. ISBN: 978-0-12-382100-3.

[45] Q. Li, P. Schlatter, L. Brandt, and D. S. Henningson. “DNS of a spatially developing turbulent boundary layer with passive scalar transport”. In: *Int. J. Heat Fluid Flow* 30.5 (2009). The 3rd International Conference on Heat Transfer and Fluid Flow in Microscale, pp. 916–929. ISSN: 0142-727X. DOI: https://doi.org/10.1016/j.ijheatfluidflow.2009.06.007.

[46] F. Lluesma-Rodríguez, S. Hoyas, and M. Perez-Quiles. "Influence of the computational domain on DNS of turbulent heat transfer up to Re_τ=2000 for Pr=0.71". In: *Int. J. Heat Mass Tran.* 122 (2018), pp. 983–992. ISSN: 0017-9310. DOI: https://doi.org/10.1016/j.ijheatmasstransfer.2018.02.047.

[47] W. R. Logie, J. D. Pye, and J. Coventry. "Thermoelastic stress in concentrating solar receiver tubes: A retrospect on stress analysis methodology, and comparison of salt and sodium". In: *Sol. Energy* 160 (2018), pp. 368–379. ISSN: 0038-092X. DOI: https://doi.org/10.1016/j.solener.2017.12.003.

[48] B. Lubarsky and S. J. Kaufman. *Review of experimental investigations of liquid-metal heat transfer*. Technical Note 3336. Lewis Flight Propulsion Laboratory Cleveland, Ohio: National Advisory Comitee for Aeronoutics, 1955.

[49] L. Marocco. "Hybrid LES/DNS of turbulent forced and aided mixed convection to a liquid metal flowing in a vertical concentric annulus". In: *Int. J. Heat Mass Tran.* 121 (2018), pp. 488–502. ISSN: 0017-9310. DOI: https://doi.org/10.1016/j.ijheatmasstransfer.2018.01.006.

[50] L. Marocco, G. Cammi, J. Flesch, and T. Wetzel. "Numerical analysis of a solar tower receiver tube operated with liquid metals". In: *Int. J. Therm. Sci.* 105 (2016), pp. 22–35. ISSN: 1290-0729. DOI: https://dx.doi.org/10.1016/j.ijthermalsci.2016.02.002.

[51] L. Marocco, A. A. di Valmontana, and T. Wetzel. "Numerical investigation of turbulent aided mixed convection of liquid metal flow through a concentric annulus". In: *Int. J. Heat Mass Tran.* 105 (2017), pp. 479–494. ISSN: 0017-9310. DOI: https://doi.org/10.1016/j.ijheatmasstransfer.2016.09.107.

[52] C. Marugán-Cruz, O. Flores, D. Santana, and M. García-Villalba. "Heat transfer and thermal stresses in a circular tube with a non-uniform heat flux". In: *Int. J. Heat Mass Tran.* 96 (2016), pp. 256–266. ISSN: 0017-9310. DOI: https://dx.doi.org/10.1016/j.ijheatmasstransfer.2016.01.035.

[53] P. Negi, R. Vinuesa, A. Hanifi, P. Schlatter, and D. Henningson. "Unsteady aerodynamic effects in small-amplitude pitch oscillations of an airfoil". In: *Int. J. Heat Fluid Flow* 71 (2018), pp. 378–391. ISSN: 0142-727X. DOI: https://doi.org/10.1016/j.ijheatfluidflow.2018.04.009.

[54] NEK5000 v17.0. Argonne National Laboratory, Illinois. Release Date 2017/12/17. URL: https://nek5000.mcs.anl.gov.

[55] N. Offermans et al. "On the Strong Scaling of the Spectral Element Solver Nek5000 on Petascale Systems". In: *Proceedings of the Exascale Applications and Software Conference 2016*. EASC '16. Stockholm, Sweden: Association for Computing Machinery, 2016, 5:1–5:10. ISBN: 978-1-4503-4122-6. DOI: https://doi.org/10.1145/2938615.2938617.

[56] I. F. Okafor, J. Dirker, and J. P. Meyer. "Influence of circumferential solar heat flux distribution on the heat transfer coefficients of linear Fresnel collector absorber tubes". In: *Sol. Energy* 107 (2014), pp. 381–397. ISSN: 0038-092X. DOI: https://dx.doi.org/10.1016/j.solener.2014.05.011.

[57] J. Pacio, L. Marocco, and T. Wetzel. "Review of data and correlations for turbulent forced convective heat transfer of liquid metals in pipes". In: *Heat Mass Transfer* 51 (2015), pp. 153–164. ISSN: 1432-1181. DOI: https://dx.doi.org/10.1007/s00231-014-1392-3.

[58] J. Pacio, C. Singer, T. Wetzel, and R. Uhlig. "Thermodynamic evaluation of liquid metals as heat transfer fluids in concentrated solar power plants". In: *Appl. Therm. Eng.* 60 (2013), pp. 295–302. DOI: https://dx.doi.org/10.1016/j.applthermaleng.2013.07.010.

[59] J. Pacio and T. Wetzel. "Assessment of liquid metal technology status and research paths for their use as efficient heat transfer fluids in solar central receiver systems". In: *Sol. Energy* 93 (2013), pp. 11–22. ISSN: 0038-092X. DOI: https://dx.doi.org/10.1016/j.solener.2013.03.025.

[60] S. V. Patankar, C. H. Liu, and E. M. Sparrow. "Fully Developed Flow and Heat Transfer in Ducts Having Streamwise-Periodic Variations of Cross-Sectional Area". In: *J. Heat Transf.* 99.2 (1977), pp. 180–186. DOI: https://dx.doi.org/10.1115/1.3450666.

[61] A. T. Patera. “A spectral element method for fluid dynamics: Laminar flow in a channel expansion”. In: *J. Comput. Phys.* 54.3 (1984), pp. 468–488. ISSN: 0021-9991. DOI: https://dx.doi.org/10.1016/0021-9991(84)90128-1.

[62] M. Piller. “Direct numerical simulation of turbulent forced convection in a pipe”. In: *Int. J. Numer. Meth. Fl.* 49.6 (2005), pp. 583–602. ISSN: 1097-0363. DOI: https://dx.doi.org/10.1002/fld.994.

[63] S. Pirozzoli, M. Bernardini, and P. Orlandi. “Passive scalars in turbulent channel flow at high Reynolds number”. In: *J. Fluid Mech.* 788 (2016), pp. 614–639. DOI: https://doi.org/10.1017/jfm.2015.711.

[64] S. B. Pope. *Turbulent Flows*. 1. publ. Cambridge: Cambridge Univ. Press, 2000.

[65] A. Rapier. “Forced convection heat transfer in a circular tube with non-uniform heat flux around the circumference”. In: *Int. J. Heat Mass Tran.* 15.3 (1972), pp. 527–537. ISSN: 0017-9310. DOI: https://doi.org/10.1016/0017-9310(72)90215-3.

[66] L. Redjem-Saad, M. Ould-Rouiss, and G. Lauriat. “Direct numerical simulation of turbulent heat transfer in pipe flows: Effect of Prandtl number”. In: *Int. J. Heat Fluid Flow* 28.5 (2007), pp. 847–861. ISSN: 0142-727X. DOI: https://doi.org/10.1016/j.ijheatfluidflow.2007.02.003.

[67] W. Reynolds. “Turbulent heat transfer in a circular tube with variable circumferential heat flux”. In: *Int. J. Heat Mass Tran.* 6.6 (1963), pp. 445–454. ISSN: 0017-9310. DOI: https://doi.org/10.1016/0017-9310(63)90119-4.

[68] P. Sagaut. *Large eddy simulation for incompressible flows: an introduction; with 11 tables*. Scientific computationPhysics and astronomy online library. Berlin: Springer, 2001. ISBN: 3-540-67890-5.

[69] S. Saha, C. Chin, H. Blackburn, and A. Ooi. “The influence of pipe length on thermal statistics computed from DNS of turbulent heat transfer”. In: *Int. J. Heat Fluid Flow* 32.6 (2011), pp. 1083–1097. ISSN: 0142-727X. DOI: https://doi.org/10.1016/j.ijheatfluidflow.2011.09.003.

[70] P. Schlatter and R. Örlü. “Turbulent boundary layers at moderate Reynolds numbers: inflow length and tripping effects”. In: *J. Fluid Mech.* 710 (Aug. 2012), pp. 5–34. DOI: https://doi.org/10.1017/jfm.2012.324.

[71] P. Schlatter, S. Stolz, and L. Kleiser. “LES of transitional flows using the approximate deconvolution model”. In: *Int. J. Heat Fluid Flow* 25.3 (2004), pp. 549–558. ISSN: 0142-727X. DOI: https://doi.org/10.1016/j.ijheatfluidflow.2004.02.020.

[72] L. Sirovich. “Turbulence and the dynamics of coherent structures - part 1: coherent structures”. In: *Quarterly of Applied Mathematics* 45.3 (1987), pp. 561–571.

[73] E. Skupinski, J. Tortel, and L. Vautrey. “Determination des coefficients de convection d’un alliage sodium-potassium dans un tube circulaire”. In: *Int. J. Heat Mass Tran.* 8.6 (1965), pp. 937–951. ISSN: 0017-9310. DOI: https://doi.org/10.1016/0017-9310(65)90077-3.

[74] E. M. Sparrow and S. H. Lin. “Turbulent heat transfer in a tube with ctrcumferentiallyvarying temperature or heat flux”. In: *Int. J. Heat Mass Transfer* 6.9 (Sept. 1963), pp. 866–867. DOI: https://doi.org/10.1016/0017-9310(63)90070-X.

[75] I. Tiselj. “Tracking of large-scale structures in turbulent channel with direct numerical simulation of low Prandtl number passive scalar”. In: *Phys. Fluids* 26.12 (2014), p. 125111. DOI: https://doi.org/10.1063/1.4905018.

[76] I. Tiselj, R. Bergant, B. Mavko, I. Bajsic, and G. Hetsroni. “DNS of Turbulent Heat Transfer in Channel Flow With Heat Conduction in the Solid Wall”. In: *J. Heat Transf.* 123 (2001), pp. 849–857. DOI: https://dx.doi.org/10.1115/1.1389060.

[77] I. Tiselj and L. Cizelj. “DNS of turbulent channel flow with conjugate heat transfer at Prandtl number 0.01”. In: *Nucl. Eng. Des.* 253 (2012). SI : CFD4NRS-3, pp. 153–160. ISSN: 0029-5493. DOI: https://dx.doi.org/10.1016/j.nucengdes.2012.08.008.

[78] I. Tiselj, A. Horvat, B. Mavko, E. Pogrebnyak, A. Mosyak, and G. Hetsroni. “Wall properties and heat transfer in near-wall turbulent flow”. In: *Numerical Heat Transfer, Part A: Applications* 46.7 (2004), pp. 717–729. DOI: https://doi.org/10.1080/10407789050400 05.

[79] V. Tricoli. “Technical Note Heat transfer in turbulent pipe flow revisited: similarity law for heat and momentum transport in low-Prandtl-number fluids”. In: *Int. J. Heat Mass Tran.* 42.8 (Apr. 1999), pp. 1535–1540. DOI: https://doi.org/10.1016/S0017-9310(98)00258-0.

[80] H. Tufo and P. Fischer. “Fast Parallel Direct Solvers for Coarse Grid Problems”. In: *J. Parallel Distrib. Comput.* 61.2 (2001), pp. 151–177. ISSN: 0743-7315. DOI: https://doi.org/10.1006/jpdc.2000.1676.

[81] VDI e.V., ed. *VDI Heat Atlas*. 2. ed. Springer reference. Berlin: Springer, 2010. DOI: https://doi.org/10.1007/978-3-540-77877-6.

[82] R. Vinuesa, L. F. de Arévalo, M. Luna, and H. Cachafeiro. “Simulations and experiments of heat loss from a parabolic trough absorber tube over a range of pressures and gas compositions in the vacuum chamber”. In: *J. Renew. Sustain. Ener.* 8.2 (2016), p. 023701. DOI: https://doi.org/10.1063/1.4944975.

[83] R. Vinuesa, L. Fick, P. Negi, O. Marin, E. Merzari, and P. Schlatter. *Turbulence statistics in a spectral element code: a toolbox for High-Fidelity Simulations*. Tech. rep. Argonne, IL (United States): Argonne National Lab. (ANL), Feb. 2017. DOI: https://doi.org/10.2172/1349052.

[84] R. Vinuesa, C. Prus, P. Schlatter, and H. M. Nagib. “Convergence of numerical simulations of turbulent wall-bounded flows and mean cross-flow structure of rectangular ducts”. In: *Meccanica* 51.12 (Dec. 2016), pp. 3025–3042. ISSN: 1572-9648. DOI: https://doi.org/10.1007/s11012-016-0558-0.

[85] B. Weigand. *Analytical Methods for Heat Transfer and Fluid Flow Problems*. 2nd ed. Mathematical EngineeringSpringerLinkSpringer eBook Collection. Berlin, Heidelberg: Springer, 2015. DOI: https://doi.org/10.1007/978-3-662-46593-6.

(Co) supervised student theses

[T1] D. Beck. “Turbulent pipe flow with heat transfer and conducting walls”. Advisors: B. Frohnapfel, S. Straub, P. Schlatter, R. Vinuesa. Masterthesis (unpublished). Karlsruhe Institute of Technology, Institute of Fluid Mechanics, 2016.

[T2] G. Centurelli. “Large Eddy Simulations of aided mixed convection to a low Prandtl number fluid in a vertical pipe flow”. Supervisor: L. Marocco, Co-Supervisor: L. Colombo, S. Straub. Masterthesis. Politecnico di Milano, Department of Energy, 2019. URL: http://hdl.handle.net/10589/150527.

[T3] J. Eggebrecht. “LES der turbulenten Wärmeübertragung von Flüssigmetallen in einem inhomogen beheizten Rohr”. Advisors: T. Wetzel, B. Frohnapfel, L. Marocco, B. Dietrich. S. Straub. Masterthesis (unpublished). Karlsruhe Institute of Technology, Institute of Fluid Mechanics, 2018.

[T4] T. Gut. “Numerische Simulation sich entwickelnder thermischer Strömungen in Solarreceivern”. Advisors: B. Frohnapfel, S. Straub. Masterthesis (unpublished). Karlsruhe Institute of Technology, Institute of Fluid Mechanics, 2018.

[T5] L. Pröbsting. “Pipe length requirements for DNS/LES of turbulent heat transfer in liquid Metals”. Advisors: B. Frohnapfel, S. Straub. Bachelorthesis (unpublished). Karlsruhe Institute of Technology, Institute of Fluid Mechanics, 2018.

[T6] S. Schlichting. “Validierung von OpenFOAM® für Wärmeübertragungssimulationen im Kontext Reynolds gemittelter Navier–Stokes Gleichungen”. Advisors: B. Frohnapfel, S. Straub, C. Bruzzese. Masterthesis (unpublished). Karlsruhe Institute of Technology, Institute of Fluid Mechanics, 2018.

Own publications

Journal articles

[SSA1] S. Straub, P. Forooghi, L. Marocco, T. Wetzel, and B. Frohnapfel. "Azimuthally inhomogeneous thermal boundary conditions in turbulent forced convection pipe flow for low to medium Prandtl numbers". In: *Int. J. Heat Fluid Flow* 77 (June 2019), pp. 352–358. DOI: https://doi.org/10.1016/j.ijheatfluidflow.2019.05.003.

[SSA2] S. Straub, P. Forooghi, L. Marocco, T. Wetzel, R. Vinuesa, P. Schlatter, and B. Frohnapfel. "The influence of thermal boundary conditions on turbulent forced convection pipe flow at two Prandtl numbers". In: *Int. J. Heat Mass Transfer* 144 (Dec. 2019), p. 118601. DOI: https://doi.org/10.1016/j.ijheatmasstransfer.2019.118601.

[SSA3] S. Straub, R. Vinuesa, P. Schlatter, B. Frohnapfel, and D. Gatti. "Turbulent Duct Flow Controlled with Spanwise Wall Oscillations". In: *Flow Turbul. Combust.* 99.3 (Dec. 2017), pp. 787–806. ISSN: 1573-1987. DOI: https://doi.org/10.1007/s10494-017-9846-6.

Conference contributions

[SSC1] S. Straub, D. Beck, B. Frohnapfel, P. Schlatter, and R. Vinuesa. "The effect of selected thermal boundary conditions on a fully developed turbulent pipe flow". In: *16th European Turbulence Conference, Stockholm, Sweden, 21-24 August 2017*. 35.12.01; LK 01. Kungliga Tekniska Högskolan, Stockholm, 2017. DOI: https://doi.org/10.5445/IR/1000088452.

[SSC2] S. Straub, P. Forooghi, L. Marocco, R. Vinuesa, P. Schlatter, T. Wetzel, and B. Frohnapfel. “The influence of thermal boundary conditions on turbulent forced convection pipe flow”. In: *17th European Turbulence Conference, Turin, Italy, 3-6 September*. 2019.

[SSC3] S. Straub, P. Forooghi, L. Marocco, T. Wetzel, and B. Frohnapfel. “Non-homogeneous thermal boundary conditions in low Prandtl number pipe flows”. In: *Turbulence, Heat and Mass Transfer 9. Proceedings of the Ninth International Symposium on Turbulence, Heat and Mass Transfer, Rio de Janeiro, BR, July 10-13, 2018. Ed.: A.P. Silva Freire*. 35.12.01; LK 01. Begell House, New York (NY), 2018, pp. 205–208. ISBN: 978-1-56700-468-7. DOI: https://doi.org/10.5445/IR/1000088453.

[SSC4] S. Straub, R. Vinuesa, P. Schlatter, B. Frohnapfel, and D. Gatti. “Turbulent duct flow with spanwise wall oscillations”. In: *11th International ERCOFTAC Symposium on Engineering Turbulence Modelling and Measurements, September 21-23, 2016, Palermo, Italy*. 35.12.01; LK 01. 2016. DOI: https://doi.org/10.5445/IR/1000071447.

Databases

[SSD1] S. Straub. *Statistics on turbulent forced convection pipe flow with different thermal boundary conditions for two Prandtl numbers*. 2019. DOI: https://doi.org/10.5445/IR/1000096346.

[SSD2] S. Straub. *Thermal statistics of turbulent forced convection pipe flow for axially and azimuthally inhomogeneous thermal boundary conditions*. 2019. DOI: https://doi.org/10.5445/IR/1000100008.

[SSD3] S. Straub. *Thermal Statistics of Turbulent Forced Convection Pipe Flow for Azimuthally Inomogeneous Thermal Boundary Conditions*. 2019. DOI: https://doi.org/10.5445/IR/1000093905.